First-Principles Calculations on the Thermodynamic and Electronic Properties of Defective Semiconductors and Semiconductor Alloys

by

Zihao Deng

A dissertation submitted in partial fulfillment
of the requirements for the degree of
Doctor of Philosophy
(Materials Science and Engineering and Scientific Computing)
in the University of Michigan
2022

Doctoral Committee:

Associate Professor Emmanouil Kioupakis, Chair
Professor Zetian Mi
Professor Pierre F. P. Poudeu
Associate Professor Liang Qi

Zihao Deng
zhdeng@umich.edu
ORCID iD: 0000-0002-7247-4040

ACKNOWLEDGEMENTS

Personal acknowledgements

Looking back at my journey in graduate school, I have received tremendous support from my advisor, collaborators, family and friends, without whom I cannot reach this important academic milestone in my life.

First and foremost, I would like to express my deepest gratitude to Manos, a phenomenal advisor, for his continuous help and support on my research, courses, and careers. Manos is a successful researcher, a knowledgeable teacher, and a fantastic mentor, and he has always been my role model. I am so lucky to join the Kioupakis group, where I met my fellow group members who are passionate about science. Working in such a friendly and collaborative environment has been a joy for me. I am especially grateful for Dr. Logan Williams, Dr. Christina Jones, and Dr. Jihang Lee for helping me navigate my first year and learn all the essential computational tools for research.

I also want to thank my collaborators who worked on various experiments, including Prof. Ferdinand Poudeu, Prof. Zetian Mi, Prof. Becky Peterson, Prof. Neil Dasgupta, and Prof. Steve Durbin. Collaborating with these talented scientists has been enjoyable and fruitful. The impact of the computational studies in this dissertation is strengthened by their experimental verification.

Studying away from home for five years was not easy, especially with Covid-19 pandemic over the past two years. Fortunately, I received exceptional emotional support and encouragement from my warm family. I am grateful that my parents always believe in me, give me their love, and respect and support my decisions. I really appreciate that I met my beloved, Wenyi, here at U-M. We had great fun and also helped each other get through the hard time. I am very excited to celebrate this important achievement with her. Finally, I am thankful that I have made many close friends in graduate school. Hanging out with them in Ann Arbor has always been a happy memory.

Funding acknowledgements

I would like to acknowledge the various funding sources that support this dissertation research: the National Science Foundation Grant No. DMR-1561008, the Intel Corporation through an Intel Strategic Research Alliance, the computational resources provided by the DOE NERSC facility under Contract No. DE-AC02-05CH11231, the computational resources provided by XSEDE through Allocation No. TG-DMR200031, the University of Michigan's Rackham International Student Fellowship, and Rackham Conference Travel Grants.

Copyright acknowledgements

Chapter II is adapted from *Phys. Rev. Materials* **3**, 053401 (2019), Copyright (2019) American Physical Society, and *Adv. Electron. Mater.* **6**, 2000337 (2020) with the permission of John Wiley and Sons.

Chapter III is reprinted from *AIP Advances* **11**, 065312 (2021), with the permission of AIP Publishing.

Chapter V is adapted from *Appl. Phys. Lett.* **119**, 132104 (2021), with the permission of AIP Publishing, and *Phys. Rev. Lett.* **122**, 256403 (2019), Copyright (2019) American Physical Society.

Chapter VI is reprinted with permission from *Chem. Mater.* **32**, 14, 6070–6077 (2020). Copyright (2020) American Chemical Society.

TABLE OF CONTENTS

CHAPTER

LIST OF FIGURES

FIGURE

LIST OF TABLES

TABLE

LIST OF APPENDICES

APPENDIX

ABSTRACT

The continuously growing computing power and the advent of advanced computational algorithms have enabled the atomistic simulations of materials at an unprecedented accuracy and scalability. In particular, first-principles calculations based on density functional theory (DFT) provide exceptional predictive capability in studying solid-state materials. In this dissertation, I applied DFT calculations to study a wide range of semiconductors that show great promise in electronic and optoelectronic applications, with a focus on the thermodynamics of point defects in semiconductors and computational discovery of novel semiconductor alloys.

Point defects are pervasive in semiconductors and it is crucial to understand their impact on the properties. Efficient p-type doping of ultrawide bandgap nitride semiconductors has been a long-standing challenge. By calculating the formation energy and charge-transition levels for intrinsic defects and extrinsic Mg dopant, I discover two avenues towards an enhanced p-doping efficiency for AlN and Al-rich AlGaN alloy. The first approach is to engineer the N chemical potentials to be N-rich, which dramatically reduces the formation energy for Mg dopant by about 2 eV and increases the formation energy of compensating N vacancy by almost 3 eV. Another method is to engineer the position of the Fermi level away from the valence band of AlGaN alloy by the formation of Ga/AlGaN Schottky junction during non-equilibrium growth. This leads to an extremely small formation energy of 0.4 eV for Mg dopant. These two approaches can be generalized to a broader range of ultrawide bandgap semiconductors.

Using the same methodology, the electronic properties and defect physics of LaN and Cu_2O are investigated. Contrast to previous claim that LaN is a semimetal, I find that LaN has a direct bandgap of 0.62 eV and is an intrinsic n-type semiconductor. The origin of its electrical conductivity is likely due to the formation of N vacancy and substitutional O impurities. The dominant intrinsic defects of Cu_2O are the Cu simple vacancy and the Cu split vacancy. However, their large ionization energies lead to low hole concentration. I survey a variety of candidate elements for p-type doping and find that N, S, and Mg are effective p-dopants.

Another part of this dissertation studies the thermodynamic and electronic properties of emerging semiconductors and semiconductor alloys. II-IV-N_2 materials exhibit unique properties due to disordering on the cation sublattice. The short-range disorder around the N atom has large impact on the thermodynamic stability. Using $ZnSnN_2$ as a model system, I find that the formation energy decreases with respect to an increased fraction of octet-rule conserving Zn2Sn2 motifs. Interestingly, the bandgap of $ZnSnN_2$ is linearly proportional to the square of the long-range order parameter, which enables alloy-free bandgap engineering. In some cases, configurational disorder can improve the thermodynamic stability by maximizing the entropy of the system. Using high-throughput DFT calculations, I investigate the stability over the entire composition space for GeSnPbSSeTe high entropy chalcogenide alloys (HEC). At the growth temperature of 900 K, 99% of the HEC compositions are stabilized by the large entropy. The bandgap calculations and the transport measurement by my collaborators show that equimolar HEC is an ambipolarly dopable semiconductor.

The computational studies presented here demonstrate the importance of point defects in controlling the properties of semiconductors and pave the way for the adoption of heterovalent ternary nitrides and high entropy chalcogenide alloys in a wide range of functional applications.

CHAPTER I

Introduction

1.1 Semiconductors and technological advancement

Our world has been revolutionized by the development of semiconductor technology over the last half a century, from silicon based large scale integrated circuits that functionalize our smartphone and personal laptop, to visible light emitting diodes (LED) that illuminate our home with efficiency exceeding 90%. Innovation in semiconducting materials still provides large momentum to the development of human civilization in the 21st century. It is therefore crucial to understand the fundamental physics underlying various class of semiconductors that have wide societal applications, which ultimately transforms into the capability of engineering the properties of semiconductors to satisfy certain goals and developing novel semiconducting materials for the future.

The huge potentials of semiconducting materials originate from their two most important properties, which are having a bandgap and controllable doping. These distinguish semiconductors from metals and insulators. The bandgap refers to the energy difference between the highest occupied electronic states (valence band maximum, VBM) and the lowest unoccupied electronic states (conduction band minimum, CBM). Depending on the positions of band extrema in the reciprocal space, the bandgap can either be direct or indirect. A direct bandgap correspond to the VBM and CBM having the same crystal momentum. If not, the bandgap is called indirect. The nature and the magnitude of the gap determines the potential applications. For a semiconductor used in optoelectronics, a direct bandgap is desired for strong optical absorption or emission and the value of the gap determines the absorption/emission peak. For example, a good solar cell material should have a direct bandgap with a value around 1.5 eV to absorb strongly in the solar spectrum. In other applications, the magnitude of the bandgap becomes more important. Consider a semiconductor for high power electronics, the performance can be quantified by the Baliga's figure of merit[4,5] (BFOM)

$$BFOM = \frac{1}{4}\varepsilon_0 \mu E_C^3, \tag{1.1}$$

where ε_0 is the static dielectric constant, μ is the electron mobility, and E_C is the breakdown field. Since BFOM has a cubic dependence on E_C, the breakdown field has the strongest impact on the performance. Generally, materials with larger bandgaps can withstand higher voltage without breaking down and thus ultrawide bandgap semiconductors such as β-Ga_2O_3 and r-GeO_2 are preferred in these applications.[6,7]

In addition to exhibiting a bandgap, another important characteristics of semiconductors is controllable doping. Doping is a process in which impurities are introduced or atoms are removed from the host materials. The purpose is to control the electrical conductivity by donating negatively-charged carriers (electrons) into the conduction band or positively-charged carriers (holes) into the valence band, and these majority carriers can conduct electricity when applying electric field. Different from insulators, the conductivity of semiconductors can be controlled over several orders of magnitude and the type of majority carriers can either be electrons (n-type) or holes (p-type) through doping. This facilitates the creation of a variety of electronic devices such as p-n junctions and field-effect transistors by combining different semiconductors together.

In fact, doping belongs to a much broader issue in semiconductors, which is the point defects. Under ambient environment, the formation of point defects is thermodynamically favorable, and point defects play an important role in determining the properties of semiconductors. Therefore, the following section introduces this issue in more detail.

1.2 Point defects in semiconductors

For a perfect crystal, the structure of materials can be represented by a repetition of the primitive cell in 3 dimension. However, there is barely any perfect crystal under ambient environment and introducing point defects in the crystal structure can reduce the Gibbs free energy by increasing the entropy of the system. Point defects are 0-dimensional imperfection in the crystal structure and can be broadly divided into three categories, which are substitutional defect, interstitial defect, and vacancy, as shown in Figure 1.1. Here, we use the notation of X_Y^q to represent a point defect, where X is the defect species, Y is the position of the defect, and q is the charge of the defect. Subtitutional defect is defined as a foreign atom replacing the original species on the same site. The foreign atom may or may not come from the constituent elements. For example, in a hypothetical material AB with only two species, A site and B site can be replaced by a foreign atom X, where X can be A, B or another species C. In this case, C_A and C_B are called substitutional impurities whereas A_B and B_A are referred to as antisites. For interstitial defect, an atom X is located in the empty space in the crystal structure, i.e. the interstitial sites, denoted as X_i. Vacancy is referred to as the empty site after removing one atom from the crystal structure. The A and B vacancies are denoted as V_A and V_B, respectively. Apart from these three basic types, more complicated defect can exist by a combination of several point defects.

The presence of point defects can have large impact on the properties of semiconductors. Defect can induce energy level within the bandgap. If the defect level

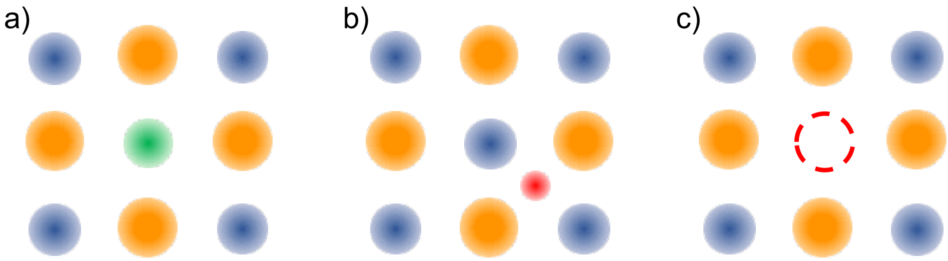

Figure 1.1: Three basic types of point defects. a) Substitutional defect, b) Interstitial defect, and c) Vacancy.

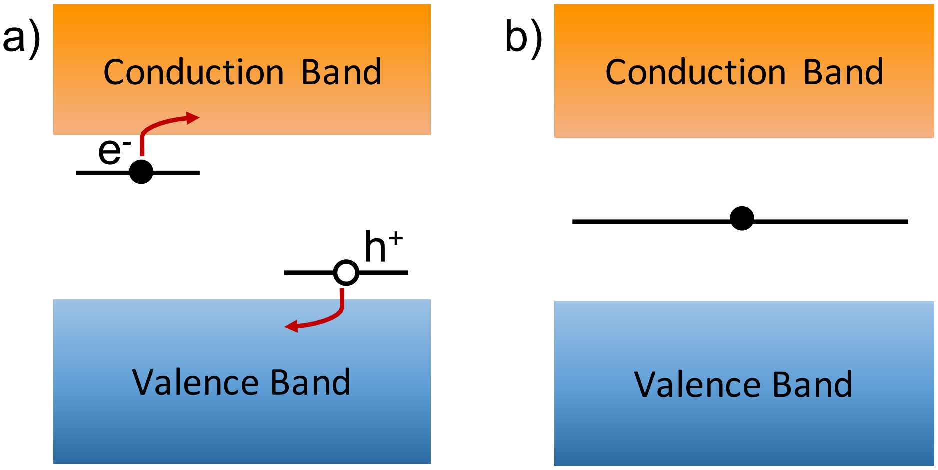

Figure 1.2: Shallow vs. deep nature of point defects in semiconductors. a) Shallow level defects can be ionized due to small ionization energy and b) deep level defects have energy level in the middle of the gap.

is located close to the band edge or even inside the valence or conduction band, this kind of defect is called shallow level defect. On the other hand, a defect is termed as deep level defect if the energy level lies far away from the band edge or in the middle of the gap. The shallow versus deep nature of a point defect (Figure 1.2) will influence the electronic properties in different ways. For shallow level defects, they usually act as donors or acceptors because the defects are ionized due to small energy difference (ionization energy) between the band edge and the defect level. Ionized donors donate free electrons to the conduction band, and ionized acceptors donate free holes to the valence band. This in turn affect the carrier concentration of the semiconductors. To achieve effective doping, shallow level defects are desired after incorporating dopant elements. Deep level defects, on the other hand, are difficult to ionize due to large energy difference between the defect level and the band edge, and they are detrimental to the efficiency of the light emitting devices. Deep level defects usually act as non-radiative recombination centers which capture electron-hole pairs and emit phonons instead of photons. As a result, the energy is dissipated as heat rather than converting to light.

Since point defects play an important role in determining the properties of semiconductors, it is crucial to understand and control the defect formation. The defect formation energy is a quantity that measures the difficulty for a defect to form, and a large part of this dissertation focuses on calculating the formation energy of various point defects in semiconductors, which provides deep insight on their impact on the electronic properties.

1.3 Semiconductor alloys

In the semiconductor community, alloying is a great method to obtain new semiconductors with desired structural and electronic properties. A semiconductor alloy is defined as a homogeneous material by mixing different semiconductors into a single phase. According to the Hume-Rothery rule,[8] a substitutional solid solution can only form if the constituent elements have similar atomic radius and share similar crystal structure. Therefore, many semiconductor alloys are formed by mixing same type of compounds, such as the $In_xGa_{1-x}N$ alloy from mixing InN and GaN. There are many benefits associated with semiconductor alloy. One of the most important benefits is the ability to engineer the bandgap and lattice constants by tuning the alloy compositions. The bandgap and lattice constants of the alloy follow the Vegard's law.[9] Take $In_xGa_{1-x}N$ alloy as an example. The bandgap and lattice constants can be calculated by equation 1.2 and equation 1.3, respectively.

$$E_g(In_xGa_{1-x}N) = xE_g(InN) + (1-x)E_g(GaN) - bx(1-x) \tag{1.2}$$

$$a(In_xGa_{1-x}N) = xa(InN) + (1-x)a(GaN) \tag{1.3}$$

Here, x is the In composition in unit of atomic percent. E_g is the bandgap value. a is the lattice constant. The bandgap relationship has an extra bowing parameter, b, to capture the nonlinearity.

Semiconductor alloys greatly expand the materials space for real applications. The highly efficient blue LED based on $In_xGa_{1-x}N$ revolutionizes the entire lighting industry.[10] The cost per LED light bulb has been reducing continuously over the last decade, and the wide adoption of LEDs over incandescence and fluorescence light bulbs will alleviate the energy crisis and global warming by increasing the overall lighting efficiency. In the thermoelectric community, alloying different semiconductors can enhance the Seebeck coefficient and reduce the thermal conductivity through phonon scattering by alloy disorder. For example, recently developed $SnS_{0.91}Se_{0.09}$ alloys realizes a high thermoelectric figure of merit and pave the way for earth-abundant, low cost thermoelectrics.[11] Alloying semiconductors with different crystal structures can lead to novel phenomena and interesting properties. Mixing rocksalt ScN and wurtzite

AlN together leads to $Sc_xAl_{1-x}N$ alloys that show promising piezoelectric and ferroelectric properties,[12] which triggers a wave of excitement on studying multiferroic in nitride materials.

This dissertation utilizes first-principles calculations to study the thermodynamic stability and electronic properties of semiconductor alloys and discover novel class of semiconducting alloys that show great promise in functional applications.

1.4 Computational methods

1.4.1 Density functional theory

The first-principles calculations performed in this dissertation is based on density functional theory. The electronic structure of solids can be fully described by solving the time independent N-electron Schrödinger equation.[13]

$$\left[-\frac{\hbar^2}{2m}\sum_{i=1}^{N}\nabla_i^2+\sum_{i=1}^{N}V(\mathbf{r}_i)+\sum_{i=1}^{N}\sum_{j<i}U(\mathbf{r}_i,\mathbf{r}_j)\right]\Psi=E\Psi \tag{1.4}$$

The three terms in the square bracket represent the kinetic energy of electrons, the potential energy of electrons due to interaction with nuclei, the potential energy of electrons due to Coulombic interaction with each other, respectively. Ψ is the N-electron wave function $\Psi(\mathbf{r}_1,\mathbf{r}_2,...,\mathbf{r}_N)$ and is often approximated by the product of single electron wave function $\Psi(\mathbf{r}_1,\mathbf{r}_2,...,\mathbf{r}_N)=\psi(\mathbf{r}_1)\psi(\mathbf{r}_2)...\psi(\mathbf{r}_N)$. However, solving the exact Schrödinger equation for N electrons is a many body problem with $3N$ degrees of freedom, which is computationally prohibitive, especially for large periodic system. Fortunately, the introduction of density functional theory enables the practical study of electronic structure of solids by solving a set of Kohn-Sham equations for single electron.[13]

$$\left[-\frac{\hbar^2}{2m}\nabla^2+V(\mathbf{r})+V_H(\mathbf{r})+V_{XC}(\mathbf{r})\right]\psi_i(\mathbf{r})=\varepsilon_i\psi_i(\mathbf{r}) \tag{1.5}$$

Here, the first two terms are still the electron kinetic energy and the potential energy due to nuclei. $V_H(\mathbf{r})$ is the Hartree potential which describes the Coulomb repulsion between one electron and the total electron density of all electrons in the system. $V_{XC}(\mathbf{r})$ is the exchange-correlation potential that includes all the other quantum mechanical effect not captured by the first three terms in the Hamiltonian, and $V_{XC}(\mathbf{r})$ is defined as the functional derivative of the exchange-correlation energy with respect to the electron density,

$$V_{XC}(\mathbf{r}) = \frac{\delta E_{XC}(\mathbf{r})}{\delta n(\mathbf{r})}$$

The solution process of Kohn-Sham equation only involves three degrees of freedom for a single electron and thus is feasible to calculate. However, the exchange-correlation energy needs to be approximated before a solution can be obtained. Two of the most popular approximation for the exchange-correlation functional is the local density approximation (LDA) and generalized-gradient approximation (GGA).[13] LDA assumes that $E_{XC}(\mathbf{r})$ only depends on the local electron density $n(\mathbf{r})$, whereas $E_{XC}(\mathbf{r})$ also depends on the gradient of the local electron density $\nabla n(\mathbf{r})$ in GGA. In this dissertation, the Perdew-Burke-Ernzerhof (PBE) exchange-correlation functional[14] is employed within the GGA approximation. While PBE functional gives a good description of the structural and thermodynamic properties of solids, it fails to predict the bandgap of semiconductors and usually causes an underestimation on the bandgap by about 50%. To address this issue, I adopt the hybrid exchange-correlation functional in this dissertation research when the bandgap is of central interest. The next part explains the ideas behind hybrid functional.

1.4.2 Hybrid exchange-correlation functional

LDA and GGA are both semi-local functional where the exchange-correlation energy only depends on the local properties. Hybrid functional, on the other hand, approximate the $E_{XC}(\mathbf{r})$ as a mixture of the semi-local LDA/GGA functional and the non-local Hartree-Fock exchange. The early PBE0 hybrid functional assumes that the exchange-correlation energy has the following form.[15]

$$E_{XC}^{PBE0} = aE_X^{HF} + (1-a)E_X^{PBE} + E_C^{PBE} \tag{1.6}$$

Here, a is a mixing parameter that controls the fraction of the exact Hartree-Fock exchange contribution. However, calculating the full Hartree-Fock exchange is computationally expensive. To address this issue, Heyd *et al.* developed a hybrid functional based on screened Coulumb potential.[16] The central idea is to separate the $E_{XC}(\mathbf{r})$ into a short-range part and a long-range part, as shown in equation 1.7.

$$E_{XC}^{HSE} = aE_X^{HF,SR}(\omega) + (1-a)E_X^{PBE,SR}(\omega) + E_X^{PBE,LR}(\omega) + E_C^{PBE} \tag{1.7}$$

Here, a range-separation parameter ω is introduced to define the extent of the short-range interaction. The short-range interaction is governed by the mixture of the Hartree-Fock exchange and the PBE exchange, and the long-range part comes purely from PBE. Further, the short-range Hartree-Fock exchange can be obtained by using a screened Coulomb potential when doing the calculation. This effectively reduce the computational cost when using the hybrid functional. In this dissertation, I employ this HSE06 hybrid functional to obtain accurate electronic properties of semiconductors.

1.4.3 Defect calculation

A large part of this dissertation studies defect physics in semiconductors and alloys using DFT calculations. I follow the formalism from Freysoldt *et al.*[17] to calculate the formation energy and charge-transition levels of various point defects. In this formalism, the point defect is modeled using supercells and the defect formation energy is calculated by

$$E_{form}(X,q) = E_{tot}(X,q) - E_{tot}(bulk) - \sum_i n_i \mu_i + q(E_{VBM} + E_F) + E_{corr}. \quad (1.8)$$

$E_{tot}(X,q)$ is the total energy of the supercell with a defect species X in charge state q. $E_{tot}(bulk)$ is the total energy of the pristine supercell for the host material. n_i is the number of atoms of species i that is added to ($n_i > 0$) or remove from ($n_i < 0$) the supercell when forming the defect. μ_i is the chemical potential for species i. E_{VBM} is the Kohn-Sham eigenvalue for the valence band maximum. E_F is the electronic Fermi level referenced to the VBM. E_{corr} is the energy correction for the artificial interaction between charged defect and its periodic images. In this dissertation, E_{corr} is calculated using the correction scheme by Freysoldt *et al.*[18] From equation 1.8, the defect formation energy is a linear function of atomic chemical potential and the Fermi level.

The atomic chemical potential μ_i is calculated by the total energy of species i in the reference state, usually in the most stable elemental phase, plus the relative chemical potential. That is, $\mu_i = E_i^{ref} + \Delta\mu_i$. $\Delta\mu_i$ is determined by a set of thermodynamic constraints. Suppose we are studying the point defects in a compound A_xB_y and there are competing secondary phase of A_rB_s. Firstly, the compound A_xB_y in thermodynamic equilibrium requires the following equality.

$$x\Delta\mu_A + y\Delta\mu_B = \Delta H(A_xB_y)$$

The right hand side is the standard formation enthalpy of A_xB_y. To avoid the formation of the secondary A_rB_s phase and the elemental phases for A and B, the following sets of inequalities must be satisfied.

$$r\Delta\mu_A + s\Delta\mu_B < \Delta H(A_rB_s)$$

$$\Delta\mu_A < 0$$

$$\Delta\mu_B < 0$$

Within these constraints, the atomic chemical potential can have a range of values that defines the thermodynamic stability region for A_xB_y.

In addition to the defect formation energy, another quantity that is of great interest is the charge-transition level, $\varepsilon(q_i, q_j)$, which is defined as the Fermi level position where the formation energies in charge state q_i and q_j are equal. Therefore, it can be calculated by

$$\varepsilon(q_i, q_j) = \frac{E_{tot}(X, q_i) - E_{tot}(X, q_j)}{q_j - q_i}.$$

The charge transition level is the position where the point defects can change their charge state and get ionized. In some scenario, this is equivalent to the ionization energy of the donors or acceptors.

1.5 Organization of dissertation

This dissertation utilizes first-principles calculations based on density functional theory to study the thermodynamic and electronic properties of various defective semiconductors and semiconductor alloys. This work is organized into the following six chapters.

Chapter II focuses on the issue of p-type doping of ultrawide bandgap nitride semiconductors. Two promising avenues to achieve effective p-doping of AlN and AlGaN alloys are revealed using defect calculations based on hybrid functional. Chapter III elucidates the electronic structure of LaN and clarifies the origin of its electrical conductivity. Chapter IV presents a comprehensive computational study of the thermodynamics of intrinsic defects, common impurities, and candidate p-type dopants of Cu_2O. Chapter V explores the impact of cation disorder on the thermodynamic and electronic properties of heterovalent ternary nitride materials (II-IV-N_2). Chapter VI proposes a novel class of high entropy chalcogenide alloys that are semiconducting and ambipolarly dopable using high throughput calculations. Chapter VII gives a summary of this dissertation and some possible avenues for future work.

CHAPTER II

Defect Thermodynamics and P-type Doping of Ultrawide Bandgap Nitride Semiconductors

2.1 Introduction

Ultrawide bandgap nitride semiconductors such as AlN and AlGaN alloy have attracted great research interest over the last decade due to their potential applications in water purification and sterilization through ultraviolet light-emitting diodes (UV-LEDs). Unlike the commercialized Hg-based fluorescence light bulbs, they do not contain toxic elements and thus are considered to be environmentally friendly. However, the external quantum efficiency (EQE) of UV-LEDs still lags behind the visible LEDs.[19] The limiting factors can be revealed from

$$\eta_{EQE} = \eta_{IQE} \cdot \eta_{IE} \cdot \eta_{LEE} \tag{2.1}$$

where η_{IQE} is the internal quantum efficiency, η_{IE} is the injection efficiency, and η_{LEE} is the light extraction efficiency. The η_{IQE} is limited by the non-radiative recombination due to the deep-level point defects. The η_{LEE} is limited by the difficulty in extracting light from the LED device structure, especially for the transverse-magnetic (TM) polarized light. Most important of all, the low η_{IE} arises from the low concentration of dopants and carriers. This is especially true for p-type AlN and AlGaN alloys and therefore achieving heavily p-type doped AlN and AlGaN alloys is the key to the realization of efficient UV-LEDs.

Effective p-type doping in ultrawide bandgap semiconductor has been a longstanding challenge because the valence band maximum is too deep referenced to the vacuum level. It is hard to find dopant species with such low energy level, which can induce a shallow level acceptor state. In terms of AlN and AlGaN alloys, Mg has been established as the only viable p-type dopant. However, substitutional Mg, i.e. Mg replacing Al, has high formation energy in AlN and AlGaN alloy under normal synthesis conditions, which hinders the incorporation of large concentration of Mg dopants. In addition, the thermal ionization energy of Mg accetpors is much larger than the thermal energy $k_B T$, and thus only a small fraction of acceptors gets ionized, which leads to low hole concentration.[20]

To overcome the doping challenge, researchers have studied various approaches to enhance free hole concentration in AlN and high Al content AlGaN, including δ-doping,[21] polarization-induced doping,[22] superlattice doping,[23] tunnel-junction doping,[24] etc. However, none of these methods has proven to be an effective and reliable approach to enhance p-type doping. Recently, Liang *et al.* achieved heavily p-doped $Al_{0.7}Ga_{0.3}N$ using molecular beam epitaxy under liquid-metal growth condition. The Mg impurity concentration can reach up to 5×10^{19} cm^{-3}. The activation energy of Mg acceptor is measured to be 220 meV, much lower than the expected value of 500 meV, which leads to a high free hole concentration of 6×10^{17} cm^{-3}.[25] However, they did not give a clear explanation to the physical mechanism behind their approach as well as the reason why the activation energy of Mg acceptor is lower than expected.

In this chapter, we study the thermodynamic of the substitutional Mg and related intrinsic defects in AlN and AlGaN alloys. Through our computational work, we show that the formation energy and the ionization energy of Mg dopants can be significantly reduced by engineering the atomic chemical potentials and the Fermi level, both of which are corroborated by the experiments. Our result points to a promising route towards addressing the long standing p-type doping problem in ultrawide bandgap semiconductors.

2.2 Computational methods

Density functional theory calculations were performed with the HSE06 hybrid functional[16] and the projector augmented wave method,[26] as implemented in the Vienna *Ab initio* Simulation Package (VASP).[27] GW-compatible pseudopotentials were used,[14] where Mg $3s$, Al $3s3p$, Ga $4s4p$, and N $2s2p$ states were treated as valence electrons. The fraction of nonlocal Hartree-Fock exchange in the hybrid functional is 0.30 for GaN and $\mathrm{Al_{0.5}Ga_{0.5}N}$, and 0.33 for AlN, giving their band gap values of 3.51, 4.65, and 6.20 eV, respectively, in close agreement with the experiments.[28–30] Defect calculations[17] were performed for GaN, $\mathrm{Al_{0.5}Ga_{0.5}N}$ and AlN using 96-atom orthorhombic supercells[31] with $2 \times 2 \times 2$ Γ-centered Brillouin-zone sampling[32] and a plane wave energy cutoff of 500 eV. The special quasirandom supercell of $\mathrm{Al_{0.5}Ga_{0.5}N}$ was generated by the Alloy Theoretic Automated Toolkit (ATAT).[33] All structures were relaxed until the force on ions is less than 0.02 eV Å^{-1}, with spin polarization included for unpaired electrons. The defect formation energies were calculated by

$$E^f(X^q) = E_{tot}(X^q) - E_{tot}(bulk) + \sum_i n_i\mu_i + q(E_F + E_{VBM}) + E_{corr} \tag{2.2}$$

where $E_{tot}(X^q)$ denotes the total energy of the supercell with a defect X in charge state q and $E_{tot}(bulk)$ is the total energy of the perfect supercell. n_i is the number of atoms of species i that the supercell exchanges with the chemical reservoir and μ_i is the chemical potentials. E_F is the Fermi energy referenced to the valence band maximum of the host material. E_{corr} accounts for the correction to the artificial interaction between charged defect and its periodic images in the supercell approach. Here,

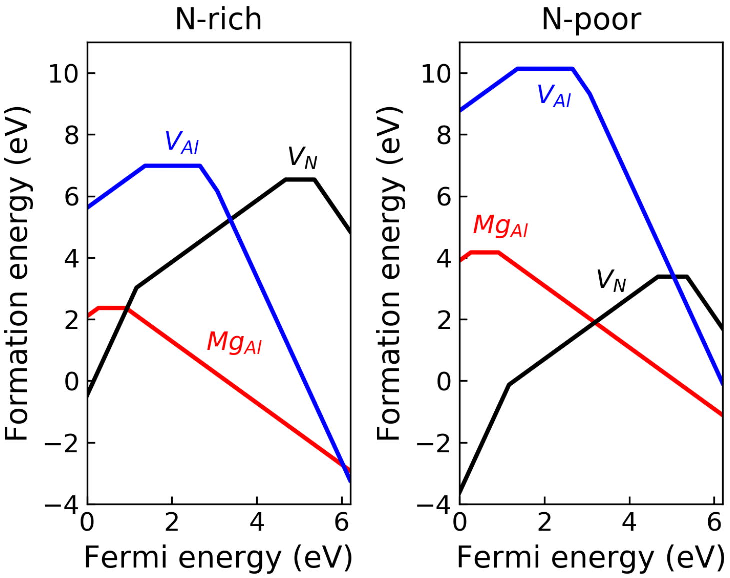

Figure 2.1: Calculated defect formation energy as a function of Fermi level for the nitrogen vacancy (V_N), aluminum vacancy (V_{Al}), Al-substitutional Mg impurity (Mg_{Al}) in AlN under N-rich and N-poor growth conditions. Compared to the N-poor condition, the formation energy of subsitutional Mg is dramatically reduced by 2 eV under N-rich condition.

corrections were based on the Freysoldt's scheme.[18] We assume Mg-rich conditions for doping and the Mg chemical potential is set to be in equilibrium with the formation of the secondary Mg_3N_2 phase.

2.3 P-type doping by chemical potential engineering

To achieve enhanced p-type doping for AlN using Mg, the formation energy of the substitutional Mg (Mg_{Al}) should be small. From equation 2.2, the defect formation energy is controlled by the atomic chemical potentials. It follows naturally that engineering the atomic chemical potential is a viable method to reduce the formation energy of Mg_{Al} and increase its concentration. This can be shown in Figure 2.1.

The conventional growth of AlN thin film adopts the N-poor condition to avoid the degradation of film quality and the formation of dislocations. However, N-poor growth condition leads to a high chemical potential for Al and a low chemical potential

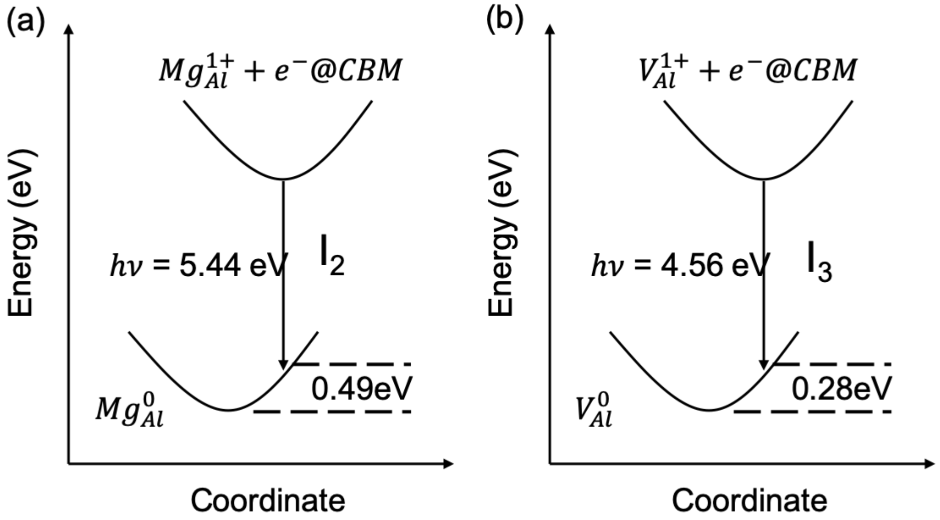

Figure 2.2: Configuration-coordinate diagram illustrating the optical processes related to Mg dopant and Al vacancy in AlN. (a) Recombination of an electron at the CBM with Mg_{Al}^{1+} to form Mg_{Al}^{0} leads to an emission peak at 5.44 eV. (b) Recombination of an electron at the CBM with V_{Al}^{1+} to form V_{Al}^{0} leads to an emission peak at 4.56 eV.

for N, which in turn causes large formation energy for V_{Al} and Mg_{Al}. In addition, the formation energy of V_N is very small. This results in a large compensation from V_N donors, and the equilibrium free hole concentration will be low. In contrast, the formation energy of Mg acceptors are significantly reduced by 2 eV and the formation energy of compensating V_N is increased drastically by 3 eV if N-rich condition is employed instead of N-poor condition, which increases the chemical potential for N and reduces the chemical potential for Al. This can be achieved in growing AlN nanowires and we show in our experiment that p-type AlN nanowires grown under N-rich condition can achieve a Mg concentration of up to 6×10^{19} cm^{-3}. Therefore, enhanced p-type doping can be realized through engineering the atomic chemical potentials during materials growth.

Our calculations also shed light on the optical processes related to the point defects in AlN. The charge of the defect can change upon optical excitation or during the optical emission, and the energy difference correspond to the photon energy that is absorbed or emitted. This can be illustrated using the configuration-coordinate diagram, as shown in Figure 2.2. In panel (a), an electron gets excited into the conduction band from the valence band and then recombine with a singly positively charged substitutional Mg. As a result, a photon with energy of 5.44 eV is emitted. Since the optical emission processes happen instantaneously, the Mg_{Al} defect still stays in the configuration of Mg_{Al}^{1+} after light emission. Mg_{Al} will eventually relax to the stable configuration of neutral state with a relaxation energy of 0.49 eV. Similarly, an emission peak of 4.56 eV can arise from the recombination of V_{Al}^{1+} with an electron at the conduction band minimum, as shown in the panel (b). These two emission peaks are corroborated by our photoluminescence experiments on AlN nanowires with reasonable agreements.[34]

2.4 P-type doping by Fermi-level engineering

In addition to the chemical potential of species, the electronic Fermi level also determines the defect formation energy, as shown in equation 2.2, with slope equal to the charge state of the defect. Therefore, engineering the position of the Fermi level will also be viable way to enhance p-type doping. Acceptors possess negative charge when they get ionized. It follows that the formation energy of acceptors will reduce linearly as the Fermi level moves away from the valence band maximum towards the conduction band.

To investigate how engineering the position of the Fermi-level affects the concentration of the Mg acceptors in AlGaN, we calculated the formation energy of Mg impurities in $Al_{0.5}Ga_{0.5}N$. Unlike their binary counterparts, $Al_{0.5}Ga_{0.5}N$ alloys can host substitutional Mg on either the Ga or Al sites, Mg_{Ga}^{0} and Mg_{Al}^{0} respectively. To determine which sites are more energetically favorable for Mg to occupy, we calculated the formation energy of Mg dopants in 5 random Ga sites and 1 Al site in the $Al_{0.5}Ga_{0.5}N$ supercell, and their values are summarized in the Table 2.1. While the

Site No.	1	2	3	4	5	6
Defect	Mg^0_{Ga}	Mg^0_{Ga}	Mg^0_{Ga}	Mg^0_{Ga}	Mg^0_{Ga}	Mg^0_{Al}
Formation energy (eV)	1.996	1.937	1.999	1.963	1.899	3.944
Activation energy (eV)	0.639	0.636	0.601	0.724	0.668	0.589

Table 2.1: Formation energy and activation energy of neutral Mg dopants on different substitutional sites on $\mathrm{Al_{0.5}Ga_{0.5}N}$ under metal-rich conditions.

activation energies of Mg acceptors on different substitutional sites vary only by approximately 0.1 eV, the formation energy of Mg^0_{Ga} (2.00 eV) is almost 2 eV lower than Mg^0_{Al} (3.94 eV) under Ga(Al)-rich conditions, indicating that Mg dopants prefer to substituting Ga rather than Al sites. This emphasizes the difficulty of incorporating high Mg concentrations in Al rich AlGaN alloys.

Despite the difficulty in doping Al-rich AlGaN alloys, we propose a new synthesis technique called metal-semiconductor junction assisted epitaxy to grow heavily p-type doped AlGaN thin film. The central idea behind this technique is to engineer the position of the Fermi level away from the valence band of AlGaN alloy, which is illustrated in Figure 2.3. Panel (a) shows the schematic of conventional epitaxial growth of Mg-doped p-AlGaN thin film. During growth, the Fermi level at the growth interface is located near the valence band maximum of AlGaN, as shown in the Panel (c). This leads to a large formation energy of Mg dopant and a low free hole concentration in $\mathrm{Al_{0.5}Ga_{0.5}N}$. In contrast, our junction assisted epitaxy facilitates the formation of a metal-semiconductor Schottky junction at the growth interface by simple providing excessive Ga flux in the chamber. A liquid Ga metal layer will then cover the surface of AlGaN. (See Figure 2.3-b) The Schottky junction will cause the band edge of AlGaN to bend downwards to align the work function of Ga metal and the equilibrium Fermi level of AlGaN, which shifts the Fermi level away from the valence band maximum at Ga/AlGaN growth interface, as shown in Panel (d). As a result, the formation energy of Mg dopant is significantly reduced by 1.6 eV, compared to that using conventional epitaxy. (See Figure 2.3-e)

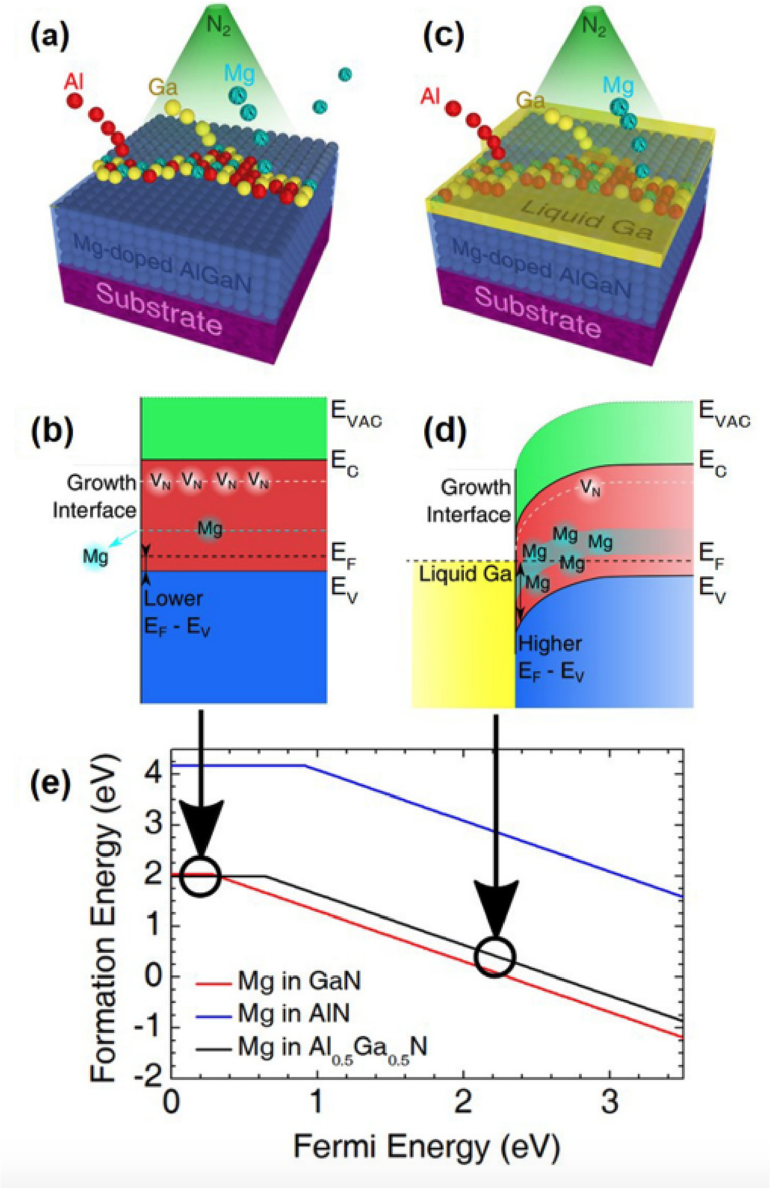

Figure 2.3: (a) Schematic of conventional epitaxy. (b) Energy band diagram of the Mg-doped AlGaN layer during conventional epitaxy. (c) Schematic of metal-semiconductor junction assisted epitaxy, with the presence of a liquid Ga layer on the surface during epitaxy. (d) Energy band diagram at the growth front of Mg-doped AlGaN during metal-semiconductor junction assisted epitaxy, showing the pinning of the surface Fermi level away from the valence band edge. (e) Calculated formation energy for Mg substitution in GaN, AlN, and $Al_{0.5}Ga_{0.5}N$ as a function of the separation between the Fermi level and the valence band with substitutional Mg formation energies for the different growth processes indicated by their respective arrows.

At this Fermi level, Mg dopant has a formation energy of only 0.43 eV. Using the following equation

$$n_{Mg} = n_{site} \cdot exp(-\frac{E^f(Mg_{Ga}^{-1})}{k_B T}) \tag{2.3}$$

and setting the growth temperature to 700 °C, we calculated an estimated Mg concentration in $Al_{0.5}Ga_{0.5}N$ to be $1.4 \times 10^{20}\ cm^{-3}$, if we assume the number of Ga sites in $Al_{0.5}Ga_{0.5}N$ to be $2.26 \times 10^{22}\ cm^{-3}$. This value is in close agreement to the highest Mg concentration in our heavily Mg-doped $Al_{0.75}Ga_{0.25}N$ films (about $2 \times 10^{20}\ cm^{-3}$).[35] Our calculated activation energy of Mg acceptors in $Al_{0.5}Ga_{0.5}N$ is about 0.6 eV, which is higher than that measured in the experiment. (around 0.3 eV) To reconcile this inconsistency, we consider the fact that when the film is heavily doped with a large concentration of Mg impurities, the wave function of Mg acceptors in $Al_{0.5}Ga_{0.5}N$ will start to overlap, leading to the formation of impurity band from isolated defect states. As a result, the effective activation energy is the energy different between the VBM and the lowest energy state of the impurity band, which is lower than the original activation energy of isolated acceptor state. The critical concentration of Mg that facilitate the formation of impurity band can be estimated from the Mott criteria.

$$a_B^* n_{critical}^{1/3} = 0.2 \tag{2.4}$$

$$a_B^* = 0.53 \times \frac{\varepsilon_r}{m_h^*} \text{Å} \tag{2.5}$$

The critical concentration is calculated to be about $2 \times 10^{20}\ cm^{-3}$, which is in perfect agreement with the Mg concentration measured in our experiment.[35] Therefore, the lower activation energy for Mg dopant in heavily p-doped AlGaN film arises from the formation of Mg impurity band in the high impurity concentration regime, which leads to a smaller effective activation energy.

2.5 Conclusions

In summary, we performed hybrid DFT calculations to study the defect thermodynamics of Mg dopants in AlN and AlGaN alloy and propose two strategies to overcome the challenge of achieving heavily p-doped AlN or Al-rich AlGaN. The first approach is to engineer the atomic chemical potentials by utilizing the N-rich conditions for AlN and alloy synthesis. The large chemical potential for N significantly reduces the formation energy of Mg dopant. The second strategy is to engineer the Fermi level position to stay away from the valence band maximum during non-equilibrium growth such as metal-semiconductor junction assisted epitaxy. The formation energy of Mg dopant is reduced dramatically as a result. Both strategies are corroborated by our defect calculations and experimental measurements. We expect these strategies to also apply in a broad range of ultrawide bandgap semiconductors and help address their long-standing challenges for efficient p-doping.

CHAPTER III

Electronic Properties and Defect Physics of Lanthanum Nitride

3.1 Introduction

Nitride compounds are a rich class of functional materials. The main-group III-nitrides are important semiconductors that find applications in electronics, optoelectronics, and photocatalysis. Recently, transition-metal and rare-earth nitrides have attracted attention due to their promise in, e.g., piezoelectric,[36] superconducting,[37] and catalysis applications.[38,39] In particular, Ye *et al.* discovered that lanthanum nitride (LaN) facilitates stable and highly efficient ammonia synthesis through the activation of N_2 gas by nitrogen vacancies at the surface. LaN shows a catalytic performance that is comparable to ruthenium-based catalysts but at a much lower cost.[39] Thus, LaN is a promising nitride material for catalysis and other chemical applications.

While LaN exhibits great promise in functional applications, one fundamental question that has not been fully addressed is whether LaN has a metallic, semi-metallic, or semiconducting nature. Understanding this fundamental electronic character of LaN is critical for its future applications. Many previous theoretical calculations have attempted to elucidate the electronic band structure of LaN. Early density functional theory (DFT) calculations with the augmented plane wave method (APW) showed that the conduction and valence bands of LaN overlap by up to 40 mRy, indicating a semi-metallic nature.[40,41] Vaitheeswaran *et al.* studied the electronic properties of LaN using tight-binding linear muffin-tin orbitals with the local-density approximation (LDA) to the exchange-correlation functional and found a metallic nature for LaN. They also estimated the superconducting transition temperature to be 0.65 K.[42] Later calculations with the generalized gradient approximation (GGA) functional observed the overlap between valence and conduction band in the band structure and characterized LaN either as metallic or as semi-metallic.[43,44] However, these results contradict to the calculations using the hybrid screened-exchange local density approximation (sX-LDA) functional where an indirect bandgap of 0.75 eV was found, suggesting that LaN might be a semiconductor.[45] Recently, more calculations seem to support the semiconducting nature of LaN. Gupta *et al.* used the LDA functional and found an indirect bandgap of 0.5 eV.[46] The GGA + U^{SIC} functional was employed by Meenaatci *et al.*, and an indirect bandgap of 0.65 eV was found.[47] However, by using the LSDA + U functional, Larson *et al.* discovered a small direct bandgap of 0.4 eV for LaN.[48] Similarly, a direct bandgap of 0.6 eV was recently obtained by the Modified Becke-Johnson Local Density Approximation (MBJLDA) functional for both wurtzite and rocksalt LaN.[49,50] In addition, Sreeparvathy *et al.* found a direct bandgap of 0.814 eV using the full potential linearized augmented plane wave (FP-LAPW) method with the TB-mBJ functional,[51] which seems to agree with the experimental bandgap of 0.82 eV measured from optical absorption.[52] Despite the progress from previous theoretical studies, the nature (direct or indirect) and the magnitude of the bandgap are not conclusively determined for LaN due to different methods and functionals employed in the calculations, which necessitates a re-investigation of the electronic properties of LaN with modern electronic structure calculations.

Since LaN is found by the more advanced functionals to exhibit a bandgap and thus to present a semiconducting rather than a semimetallic character, its electrical conductivity must originate from intrinsic or unintentional dopants. However, to the best of our knowledge, there is no theoretical investigation into the thermodynamics of the intrinsic defects and common impurities of LaN, which is the key to understand the origin of its electrical conductivity. This knowledge is also necessary in order to rationally tune its conductivity by controlling the defect formation and doping in experiments. Thus, theoretical insights into the intrinsic defect formation and ionization energies are crucial to enable the adoption of LaN in wider electronic and catalysis applications.

In this work, we study the electronic properties (band structure, effective masses, dielectric constants, and so on) and defect thermodynamics of LaN using first-principles calculations based on DFT with the HSE06 hybrid functional,[16] which predicts accurate electronic properties for a wide range of materials. We find that LaN is a direct-bandgap semiconductor with a bandgap of 0.62 eV at the X point of the Brillouin zone. Our defect calculations attribute the origin of its electrical conductivity to the unintentional formation of N vacancies or substitutional O impurities. Our calculations clarify the semiconducting nature of LaN and reveal candidate defects that are the likely origin of its measured electrical conductivity.

3.2 Computational methods

DFT calculations were performed using the Vienna *ab initio* Simulation Package (VASP).[27] GW-compatible Perdew–Burke–Ernzerhof (PBE) pseudopotentials[14] for La and N and a planewave energy cutoff of 500 eV were employed in all calculations. La $5s^2 5p^6 5d^1 6s^2$ and N $2s^2 2p^3$ were treated as valence electrons. In order to get accurate electronic properties, we used the HSE06 hybrid exchange-correlation functional with a standard mixing parameter of 0.25.[16] The electronic band structures of LaN were calculated with a fully relaxed two-atom rocksalt primitive cell (space group *Fm-3m*) and a Γ-center 8 × 8 × 8 Brillouin zone sampling grid.[32] The special k-point path for plotting the band structure followed the convention of Setyawan and Curtarolo.[53] Spin–orbit coupling effects were included in the band structure. The static and high-frequency dielectric constants were calculated by the self-consistent response to the finite electric field at the HSE level using modern theory of polarization.[54–57] Electron and hole effective masses were extracted by fitting the HSE band structure with the hyperbolic equation,

$$E(k) = \frac{\mp 1 \pm \sqrt{1 + 4\alpha \frac{\hbar^2 k^2}{2m^*}}}{2\alpha} + E_0 \tag{3.1}$$

where E_0 is the energy of the band extremum, m is the effective mass, and α is a fitting parameter to characterize the nonparabolicity of the band. The band alignment of LaN was obtained by aligning the bulk average electrostatic potential to the vacuum level. This was done by performing HSE calculations for the LaN (100) and (110) slabs without surface relaxation. The alignment results for the two slabs differ by only 70 meV. Defect calculations[17] were performed with 2 × 2 × 2 supercells built from the eight-atom rocksalt unit cell (i.e., 64 atoms), and the Brillouin zone was sampled with a Γ-center 2 × 2 × 2 grid. The defect formation energies and charge-transition levels for the O_N defect are found to change by less than 0.05 eV for a larger supercell with 128 atoms (Table A.1). Thus, the 64-atom supercell was employed for all subsequent defect studies to reduce the computational cost. All defect supercells were relaxed with HSE06 by allowing ion displacements until the forces on the ions were less than 0.02 eV·Å^{-1}. Spin polarization was included in calculations with unpaired electrons. We employed the scheme of Freysoldt *et al.*[18] and our calculated static dielectric constant for LaN to correct the artificial periodic charged-defect interactions. The competing phases we considered in the thermodynamic analysis of defect formation are La_2O_3, NO_2, NH_3, and all stable elemental phases.

3.3 Results and discussion

We first investigate the band structure of LaN to determine its electronic character (metal or semiconductor) and the magnitude of its bandgap if one exists. Previous DFT calculations using the GGA functional characterized LaN as a semimetal.[43,44] Indeed, our own PBE band-structure calculations (Figure A.1) reveal that the conduction and valence bands overlap by 115 meV at the X point, which leads to the conclusion that LaN is a semimetal and agrees with many previous theoretical studies. However, calculations with semilocal exchange-correlation functionals such as LDA or PBE severely underestimate the bandgaps of materials and may erroneously lead to a closed gap in LaN. Moreover, we find that even after one-shot GW corrections on top of PBE, the bandgap is still extremely small (0.05 eV from Table 3.1), which indicates that the metallic PBE state is a poor starting point for GW. Thus, the adoption of a non-local functional in the calculations is necessary to give an accurate bandgap and a good starting point for GW corrections. Table 3.1 shows our calculated bandgap for LaN using the HSE06 hybrid functional with GW and spin–orbit coupling corrections, respectively. Under all circumstances, LaN shows a direct bandgap at the X point of the Brillouin zone. The bandgap value is 0.75 eV if we only use HSE in the calculations. Both one-shot GW correction and spin–orbit coupling decrease the bandgap value into the range of 0.6–0.7 eV. Our results are consistent with the most recent studies by Winiarski and Kowalska where they found a direct bandgap of 0.6 eV for LaN using the MBJLDA functional including the relativistic spin–orbit effect.[49,50] This provide the direct evidence that LaN is a semiconductor rather than a semimetal. We therefore attribute the mis-categorization of LaN as a semimetal in previous studies to the systematic bandgap underestimation problem of LDA and GGA.

Method	E_{gap}(eV)	Character
PBE (this work)	0	Semi-metallic
PBE + GW (this work)	0.05	Direct X-X
HSE06 (this work)	0.75	Direct X-X
HSE06 + GW (this work)	0.68	Direct X-X
HSE06 + SOC (this work)	0.62	Direct X-X
APW,[40,41] LDA,[42] GGA,[43,44] HGH[46]	0	Semi-metallic
sx-LDA[45]	0.75	Indirect Γ-X
LDA[46]	0.5	Indirect Γ-X
GGA + U[47]	0.65	Indirect Γ-X
LSDA + U[48]	0.4	Direct X-X
MBJLDA[49,50]	0.6	Direct X-X
FP-LAPW, TB-mBJ[51]	0.814	Direct X-X

Table 3.1: Comparison of the LaN bandgap calculated in this work and previous studies

<table>
<tr><td colspan="2">Crystal structure</td><td colspan="2">Lattice constant (Å)</td></tr>
<tr><td colspan="2">Rocksalt</td><td colspan="2">5.282</td></tr>
<tr><td colspan="2">Bandgap (eV)</td><td colspan="2">Valence band splitting (meV)</td></tr>
<tr><td colspan="2">0.62</td><td colspan="2">85</td></tr>
<tr><td colspan="2">Static dielectric constant, ε_0</td><td colspan="2">High frequency dielectric constant, ε_∞</td></tr>
<tr><td colspan="2">13.32</td><td colspan="2">9.04</td></tr>
<tr><td colspan="4">Electron and hole effective masses</td></tr>
<tr><td></td><td>X-G</td><td>X-W</td><td>X-U</td></tr>
<tr><td>m_e^*/m_0</td><td>1.211</td><td>0.178</td><td>0.136</td></tr>
<tr><td>m_{h1}^*/m_0</td><td>0.329</td><td>0.632</td><td>0.376</td></tr>
<tr><td>m_{h2}^*/m_0</td><td>1.956</td><td>0.246</td><td>0.149</td></tr>
<tr><td>m_{h3}^*/m_0</td><td>0.720</td><td>0.399</td><td>0.254</td></tr>
</table>

Table 3.2: Structural and electronic properties of LaN evaluated with the HSE06 hybrid functional and spin-orbit coupling

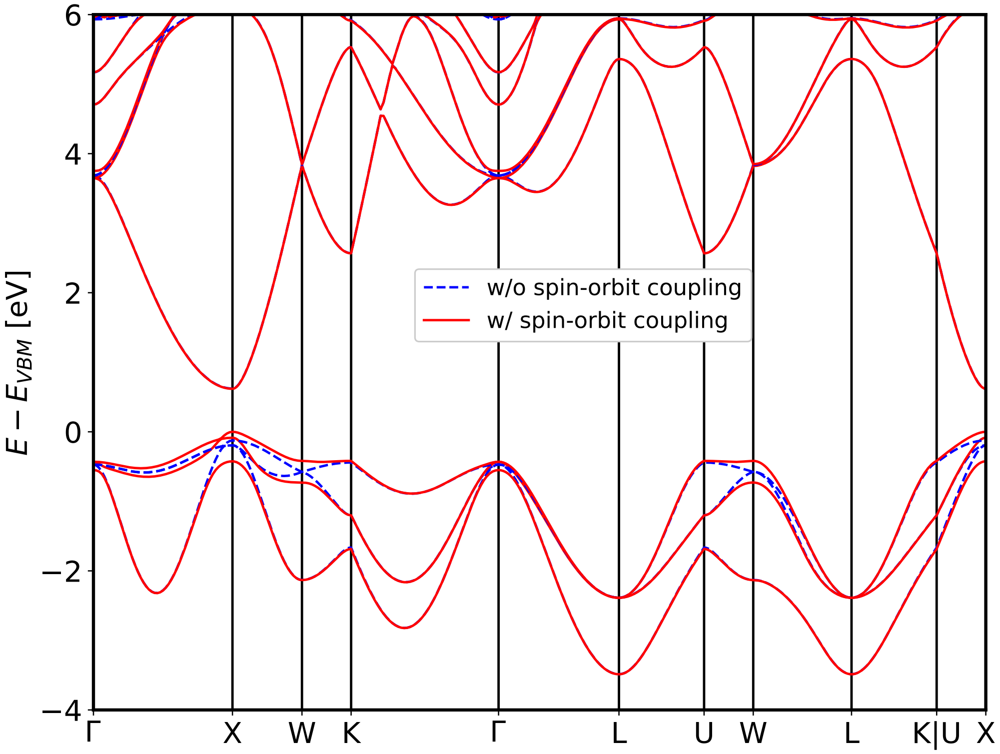

Figure 3.1: The electronic band structure of LaN calculated with the HSE06 hybrid density functional with (w) and without (w/o) spin–orbit coupling. Instead of a semimetal, LaN is a direct bandgap semiconductor with a bandgap of 0.62 eV at the X point.

Figure 3.1 shows the electronic band structure of LaN calculated with HSE and spin–orbit coupling. The conduction band and the valence band are separated by a direct gap of 0.62 eV at X. The valence band of LaN is mainly derived from N 2p orbitals and the conduction band is derived from the spatially extended unoccupied La 5d orbitals, as can be seen from the orbital projected band structure in Figure A.2. Spin–orbit coupling has a profound effect on the structure of the valence band, particularly at the high symmetry points (Γ, X, and W). This arises from the contribution of La p orbitals near those points (Figure A.2). After including the spin–orbit effect, the bandgap decreases from 0.75 to 0.62 eV. The three-fold degenerate N p orbitals at Γ split into a two-fold degenerate $p_{3/2}$ band and a one-fold $p_{1/2}$ band. Similarly, the two-fold degeneracy between the second and third valence bands at the X point and between the first and second valence bands at the W point is broken, with energy splittings of 340 and 301 meV, respectively. Table 3.2 summarizes the structural and electronic properties of LaN. We obtain a lattice constant of 5.282 Å, which is in excellent agreement with the experimental value of 5.284 Å.[58] The conduction band of LaN is dispersive with a bandwidth of several eV, leading to small electron masses especially along the transverse X–W and X–U directions. The hole effective masses are comparable to or even lighter than the hole effective masses of GaN.[59] The energy splitting between the two topmost valence bands is 85 meV, which is larger than the thermal energy $k_B T$ of 26 meV at room temperature. This indicates a much weaker phonon-mediated hole scattering from the valence band maximum to the second-highest valence band, as in the case of strained BAs.[60] The reduced scattering rate coupled with light effective masses may lead to a high hole mobility in LaN, although no p-type conductivity has been observed experimentally so far.

To investigate the band offsets between LaN and the other III-N materials in heterostructures and to understand its properties for photocatalysis, we calculate its absolute band positions by aligning the bulk average electrostatic potentials to the vacuum region. The potentials of the surface can depend on many factors, including surface reconstruction, surface dipoles, and strain effect at the interface. To avoid these complications, the slab calculations were performed without surface relaxation, which reflects a natural band alignment between the bulk region of different semiconductors and is more appropriate to study band offset across a variety of semiconductors in a consistent fashion. Figure 3.2 shows the absolute band alignment for LaN in comparison to other III-N materials. The bandgap and absolute band positions of LaN are similar to ScN, another nitride material with the rocksalt crystal structure, forming a type-II alignment at the interface with a relative band offset of 0.3 eV.

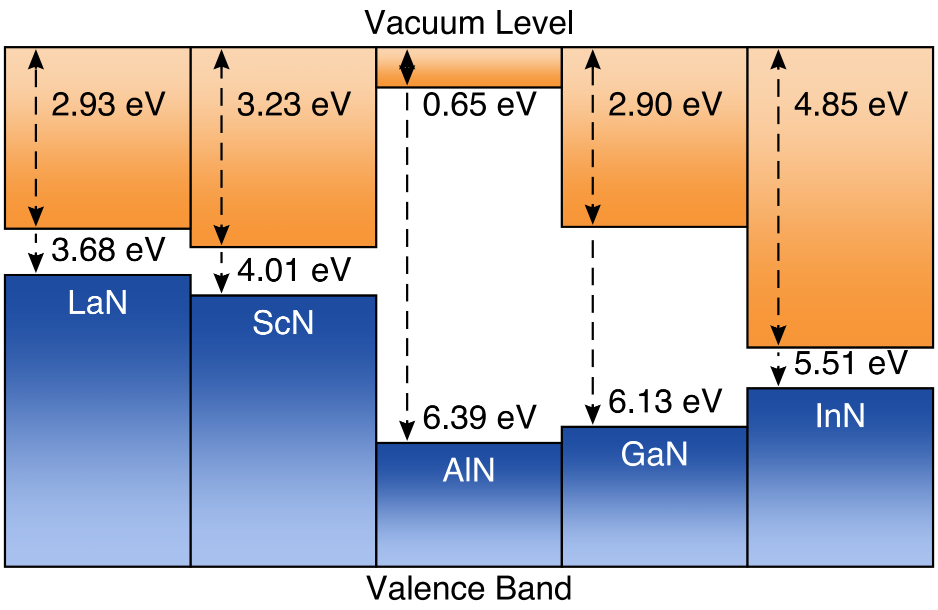

Figure 3.2: Band alignment between LaN and other nitride materials. LaN has a type-II alignment with ScN and a type-I alignment with GaN and AlN. The electron affinity of LaN and GaN is almost identical. The band-alignment data of ScN and III-N are taken from the work of Kumagai *et al.*[1] and Moses *et al.*,[2] respectively.

Interestingly, the electron affinity is almost identical for LaN and GaN. This can find potential applications in LaN/GaN heterostructures where electrons can move across the interface without a potential barrier.

We then turn to the origin of the electrical conduction in LaN that is observed in experiment.[3,61,62] Previous studies attributed the conduction to the semi-metallic character of LaN. However, this explanation is inconsistent with our accurate band-structure results that find LaN to be a semiconductor with a bandgap. An alternative explanation is that the electrical conduction in LaN is caused by unintentional doping by either intrinsic defects or unintentional impurities incorporated during growth. To shed light on this issue, we calculate the formation energy of intrinsic defects (lanthanum vacancies V_{La} and nitrogen vacancies V_N) and common unintentional impurities (substitutional O and H interstitials). Figure 3.3 shows their formation energy as a function of Fermi energy (referenced to the VBM) and growth conditions (N-rich or N-poor). Our key finding is that the donor-like defects (V_N and O_N)

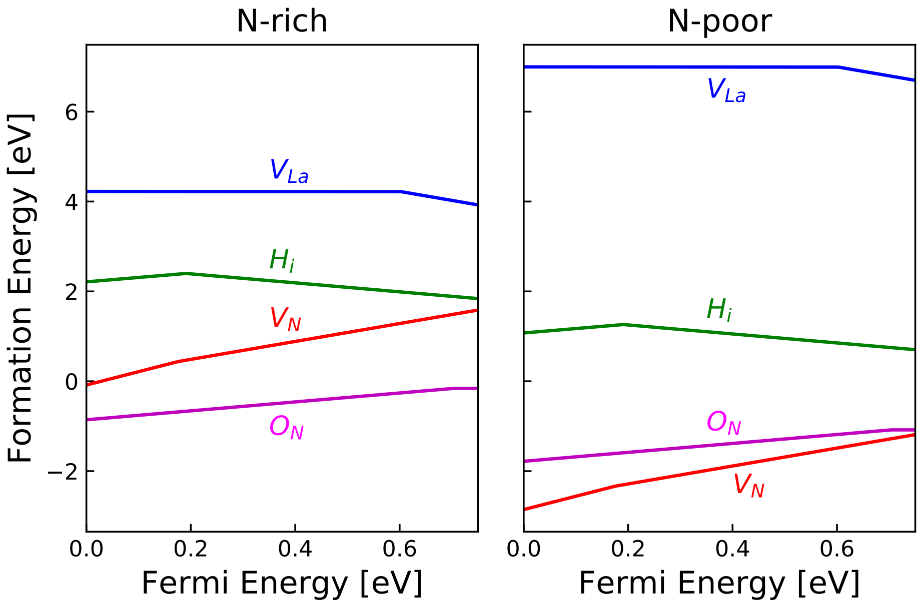

Figure 3.3: Calculated defect formation energy as a function of Fermi level for the nitrogen vacancy (V_N), lanthanum vacancy (V_{La}), hydrogen interstitial (H_i), and N substitutional oxygen impurity (O_N) in LaN. Donor-like defects (V_N and O_N) exhibit the lowest formation energy for every Fermi level, indicating that LaN is an intrinsic n-type semiconductor and its conductivity originates from V_N or O_N.

have significantly lower formation energies (even negative) than acceptor-like defects, which identify LaN to be an intrinsically n-type semiconductor. Nitrogen vacancies act as negative-U double donors and are stable in the +2 charge state for Fermi levels throughout the majority of the bandgap. O impurities are singly charged shallow donors, with an ionization energy of 50 meV. Therefore, both of these donor-like defects are candidate origins of the measured conductivity.

To further confirm the origin of the conductivity, we compare our findings to experimental measurements of the electrical conductivity as a function of temperature measured by four-point probe measurements in the literature. Lesunova *et al.*[3] found an exponentially increasing electrical conductivity with increasing temperature, which is characteristic of thermal activation of dopants in semiconductors. The temperature trend is also in contrast with the typical behavior in metals in which the conductivity decreases with temperature due to increased carrier scattering by phonons. We further extract the donor activation energy by fitting the Arrhenius equation,

$$\sigma(T) = \sigma_0 \cdot \exp(-\frac{E_A}{k_B T}) \tag{3.2}$$

to the experimental electrical-conductivity measurements by Lesunova *et al.*,[3] as shown in Figure 3.4. The fitted value for the activation energy E_A is 40 meV, which is in excellent agreement with our calculated ionization energy for shallow donors (39 meV) evaluated with the Bohr model,

$$E_A = \frac{13.6 \text{ eV} m_e^*}{\varepsilon_r^2} \tag{3.3}$$

using a directionally averaged electron effective mass of 0.51 m_e and a static dielectric constant of 13.32. Based on this qualitative and quantitative agreement with the literature-reported experimental conductivity measurements, we conclude that the electrical conductivity of LaN originates from unintentional doping and V_N and O_N are likely candidate defects.

In our calculation, O_N has a negative formation energy under both N-rich and N-poor conditions. However, this should not be interpreted as a sign of instability for LaN. In fact, the synthesis chemistry of LaN is well understood and LaN has been utilized in catalysts for NH_3 synthesis[39] and for electrodes in supercapacitors.[62] Rather, the negative formation energy indicates that substitutional O is a major source of unintentional impurities, which could possibly lead to degenerate n-type doping for LaN. In comparison, rocksalt ScN and Sc-containing nitride alloys, compounds with similar chemistry as LaN, have been found to have negative formation energy for O_N in defect calculations,[1] and O gets unintentionally incorporated during growth[63,64] and results in degenerate n-type doping.[65] Thus, an oxygen-free growth environment is necessary to prevent the undesired degenerate doping by substitutional O for LaN.

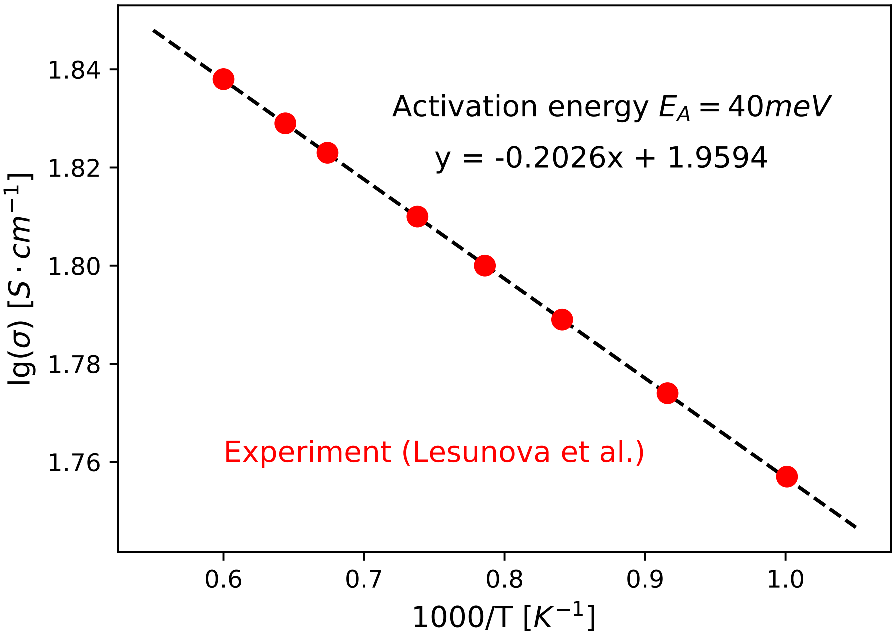

Figure 3.4: Electrical conductivity of LaN as a function of temperature. The experimental data are taken from the measurements of Lesunova *et al.*[3] The dashed line is a least-squares fit to the conductivity data. The donor activation energy extracted from the fitting is 40 meV, in good agreement with the ionization energy for O_N and V_N.

3.4 Conclusions

In conclusion, we study the electronic properties of LaN using DFT calculations based on the HSE06 hybrid functional. In contrast to the semi-metallic nature claimed by most previous studies, we find that LaN is a direct-bandgap semiconductor with a gap of 0.62 eV at the X point. The light electron and hole effective masses and the near-zero conduction-band offset with GaN make LaN promising for electronic and optoelectronic applications. Our defect calculations indicate that LaN is intrinsically n-type and the source of the measured electrical conductivity is attributed to unintentional doping by nitrogen vacancies or substitutional oxygen. Our studies clarify the semiconducting nature of LaN and reveal candidate unintentional donors that explain the origin of its measured electrical conductivity.

CHAPTER IV

Defect Physics and P-type Doping of Cuprous Oxide

4.1 Introduction

Cuprous oxide (Cu_2O) is an important oxide semiconductor due to its p-type conductivity, Earth abundancy, nontoxicity, and low cost.[66] Cu_2O exhibits unique electronic and optoelectronic properties and finds wide applications in photocatalysis,[67,68] gas sensing,[69,70] and thin-film transistors.[71,72] The performance of Cu_2O in these applications is related to the defects present. For example, oxygen vacancies play an important role in enhancing the photocatalytic properties of Cu_2O-based catalysts due to an increase in the lifetime of photogenerated carriers.[73] In addition, an excessively large number of sub-gap trap states can lead to extremely low field-effect mobility of Cu_2O thin-film transistors.[74] Thus, understanding the thermodynamics of defects in Cu_2O is critical to optimize the performance of Cu_2O-based functional devices.

Numerous previous theoretical and experimental studies focused on the defects and dopants of Cu_2O. Experimentally, deep level transient spectroscopy (DLTS) has been used to study the trap states in Cu_2O.[75,76] Two trap states were identified at 0.25 eV and 0.45 eV above the valence band edge of Cu_2O, which were identified as the Cu vacancy and the Cu divacancy, respectively.[76] Temperature-dependent diffusion experiments showed that both the neutral and the singly charged Cu vacancies contribute to cation self-diffusion.[77] Moreover, electrical conductivity measurements as a function of temperature and oxygen partial pressure revealed that electronic transport of non-stoichiometric Cu_2O is enabled by the charged oxygen interstitials with a formation energy and hole-conduction energy of 2 eV and 0.82 eV, respectively.[78] Similar transport experiments showed that the dominant point defects are doubly charged oxygen interstitials at temperatures above 1150 K and singly charged Cu vacancies at temperatures below 950 K.[79] It is therefore evident that intrinsic defects are the key to understand the carrier transport mechanisms in Cu_2O.

On the theory side, first-principles calculations based on density functional theory (DFT) have evolved into a powerful set of methods to study point defects in semiconductors such as Cu_2O.[17] In the earliest DFT study on Cu vacancies by Wright and Nelson using the local density approximation (LDA),[80] they found an intermediate stable configuration for Cu vacancy where a Cu atom moves halfway towards a nearby Cu vacancy, creating the so-called "split" vacancy (V_{Cu}^{split}).[81] The other normal configuration of removing one Cu atom is referred to as simple vacancy (V_{Cu}). They found that the formation energy for V_{Cu}^{split} is 0.1 eV lower than the simple vacancy.[81] Later, Nolan and Elliot used the generalized gradient approximation (GGA) for the exchange correlation functional and found that the formation energies for V_{Cu} and V_{Cu}^{split} using DFT-GGA are 0.41 eV and 0.47 eV, respectively. However, LDA and GGA suffer from the bandgap underestimation problem and cannot give a consistent description of the electronic structure of Cu_2O.[81,82]

To solve this problem, the DFT+U method has been applied to study the formation energies of vacancies. Within DFT+U, V_{Cu} is much more stable than V_{Cu}^{split} [e.g., $E^f(V_{Cu}) = 1.17$ eV, $E^f(V_{Cu}^{split}) = 1.7$ eV from Nolan *et al.*,[82] and $E^f(V_{Cu}) = 0.92$ eV, $E^f(V_{Cu}^{split}) = 1.66$ eV from Scanlon *et al.*[83]]. Despite having an improved description of the localized d orbital electrons of Cu, DFT+U does not recover the correct same ionization energy measured in the experiment.[83] Scanlon *et al.* employed more advanced electronic-structure methods based on hybrid functionals to study the formation and ionization energies of intrinsic defects and H interstitials in Cu_2O.[84,85] They predicted the ionization energy for V_{Cu} and V_{Cu}^{split} to be 0.22 eV and 0.47 eV, respectively, in very good agreement with DLTS measurements.[76] Their calculated formation energies for V_{Cu} and V_{Cu}^{split} are almost the same. However, Isseroff and Carter argued that calculations by Scanlon *et al.* were underconverged because only the Γ-point was used for the sampling of the Brillouin zone. With more converged computational settings, they discovered that the formation energy of V_{Cu} is consistently lower than V_{Cu}^{split} by 0.21 eV regardless of the functional used (GGA, GGA+U, or hybrid).[86] Therefore, despite numerous theoretical studies on defect thermodynamics in Cu_2O, different conclusions have been drawn regarding the nature of Cu vacancies due to the different computational methods employed in each study. Also, a systematic theoretical study on possible cationic and anionic dopants for p-type doping for Cu_2O to tune the electrical properties is lacking from the literature. We thus find it necessary to revisit the problem of defect formation and doping in Cu_2O using DFT calculations with the accurate HSE06 hybrid functional.

In this work, we calculate the formation energies and thermodynamic charge-transition levels for the isolated intrinsic defects of Cu_2O, as well as H and C impurities, and candidate acceptor elements (N, P, S, Mg, and Sn). We also perform temperature-dependent electronic transport measurement to reveal the acceptor states in Cu_2O and confirm our calculated ionization energy. We find that the V_{Cu} and the V_{Cu}^{split} are the two dominant intrinsic defects. The formation energy of V_{Cu} is 0.12 eV lower than that of V_{Cu}^{split}, which indicates that the simple vacancy is more stable than the split vacancy and agrees with previous theoretical work by Isseroff and Carter.[86] Our calculated ionization energies for the simple and split vacancy are

0.36 eV and 0.54 eV, respectively, in good agreement with our own transport measurements and previous reports in the literature. We also find that N, S, and Mg are effective p-type dopants that increase the concentration of acceptors in Cu_2O. Our calculations clarify the thermodynamics of defects and impurities of Cu_2O, and propose possible doping strategies to engineer its the electronic properties.

4.2 Methodology

4.2.1 First-principles calculations

The electronic band structure and defect thermodynamics of Cu_2O were studied by first-principles calculations based on density functional theory (DFT) using the Vienna *ab initio* Simulation Package (VASP).[27] Perdew-Burke-Ernzerhof (PBE) pseudopotentials[14] were employed for Cu, O, and the impurity and dopant elements presented in this study. The interactions between the core and the valence electrons were treated by the projector-augmented wave method as implemented in the VASP package.[26] We used a plane-wave energy cutoff of 550 eV in all calculations to converge the total energy to 1 meV/atom. In order to get accurate electronic and defect properties, we used the HSE06 hybrid exchange-correlation functional with a mixing parameter of 0.28,[16] which gives a bandgap value of 2.15 eV for Cu_2O, in close agreement with previous calculations and experiments.[66,84] The electronic band structures were calculated with a fully relaxed 6-atom primitive cell and a Γ-center 8×8×8 Brillouin zone sampling grid.[32] The phase boundaries between CuO/Cu_2O and Cu_2O/Cu were calculated by finding the crossing point of the oxygen grand potential in different phases followed by converting oxygen chemical potential into (T, P) space using the tabulated data in NIST-JANAF Thermochemical Tables.[87] Defect calculations[17] were performed with 2×2×2 supercells built from the 6-atom primitive cell for Cu_2O and the Brillouin zone was sampled with a Γ-centered 2×2×2 grid. The defect formation energy is calculated by

$$E^f(X^q) = E_t(X^q) - E_t(Cu_2O) + \sum_i n_i\mu_i + q(E_{VBM} + E_F) + E_{corr} \tag{4.1}$$

where $E_t(X^q)$ denotes the total energy of the supercell with a defect X in charge state q and $E_t(Cu_2O)$ is the total energy of the pristine supercell. n_i is the number of atoms that the supercell exchanges with the chemical reservoir and μ_i is the chemical potential of species i. E_F is the Fermi energy referenced to the valence band maximum of Cu_2O. E_{corr} corrects the artificial interaction between charged defects and their periodic images. Convergence of the formation energy and charge-transition levels were tested for V_{Cu} in a 3×3×3 supercell (Table B.1), which shows that the charge-transition levels and the formation energy were converged to 20 meV and 0.3 eV, respectively. All defect supercells were relaxed with the HSE06 functional by allowing ion displacements until the forces on the ions were lower than 0.02 eV Å^{-1}. Spin polarization was included in calculations with unpaired electrons. We employed the scheme of Freysoldt *et al.*[18] and the experimental static dielectric constant of 7.11 to correct the artificial periodic charged-defect interactions.[88] The competing phases we considered in the thermodynamic analysis of defect formation are CuO, Cu_3N, Cu_2S, H_2O, P_2O_5, SnO, SnO_2, CO_2, MgO, and all stable elemental phases.

4.2.2 Experiments

To study the electrical properties of Cu_2O films, thin film transistors (TFTs) were fabricated using the same method described in our previous study.[89,90] The Cu_2O layers in samples S#1 and S#2 were deposited by RF magnetron sputtering (physical vapor deposition, PVD)[89] while in sample S#3 it was deposited by atomic layer deposition (ALD).[90] Temperature-dependent current-voltage measurements were performed in the dark, in vacuum, at temperatures from 140 K to 300 K (with 20 K steps) using a Lakeshore Cryotronics TTPX cryogenic probe station.

4.3 Band structure and thermodynamic stability

We first revisit the basic thermodynamic and electronic properties of Cu_2O using the HSE06 hybrid functional. This allows us to verify the accuracy of the computational approach we will later employ for the defect and dopant studies. Figure 4.1 shows our calculated electronic band structure for Cu_2O. Cu_2O is a direct bandgap semiconductor with a bandgap value of 2.15 eV. Our calculated band structure is in agreement with numerous previous theoretical calculations.[66,82,91–96] Our hybrid functional calculation addresses the systematic bandgap underestimation of previous LDA/GGA or DFT+U calculations and is in good agreement with other studies using hybrid functionals[66,82,83,96,97] and many-body GW methods.[94,95] Both the conduction band minimum (CBM) and the valence band maximum (VBM) are mainly derived from Cu 3*d* orbitals (Figure B.1 and Table B.2), which leads the fundamental bandgap from CBM to VBM to be parity-forbidden. However, the second conduction band at Γ has Cu 4*p* orbital character (Table S2). This indicates that the lowest allowed optical transition at Γ occurs from the VBM to the second lowest conduction band, with an energy difference of 2.77 eV. This is also evidenced by our calculated imaginary part of the dielectric function (Figure B.2), where the first absorption peak appears around $\hbar\omega = 2.8$ eV. The optically allowed transitions have also been well studied by previous experiments for Cu_2O.[98–101] Our calculations results are in good quantitative agreement with literature[98–101] and our experimentally measured optical band gap of 2.6 eV (Figure B.3).

Next, we investigate the thermodynamic stability of Cu_2O by calculating the phase diagram for the Cu-O system, which is shown in Figure 4.2. As the O_2 pressure increases during the synthesis of Cu_2O, the stable phase changes from Cu to Cu_2O and finally to CuO. The narrow stability region for Cu_2O is defined by the phase bound-

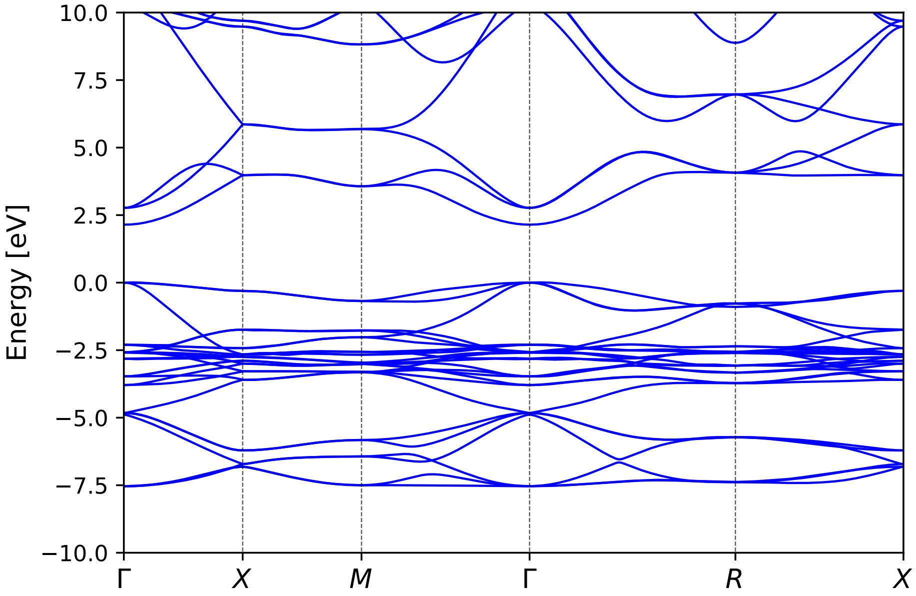

Figure 4.1: Electronic band structure of Cu_2O calculated using the HSE06 hybrid functional. The valence band maximum is set to 0 eV. Cu_2O is a direct gap semiconductor with a dipole-forbidden band gap of 2.15 eV at the Γ point.

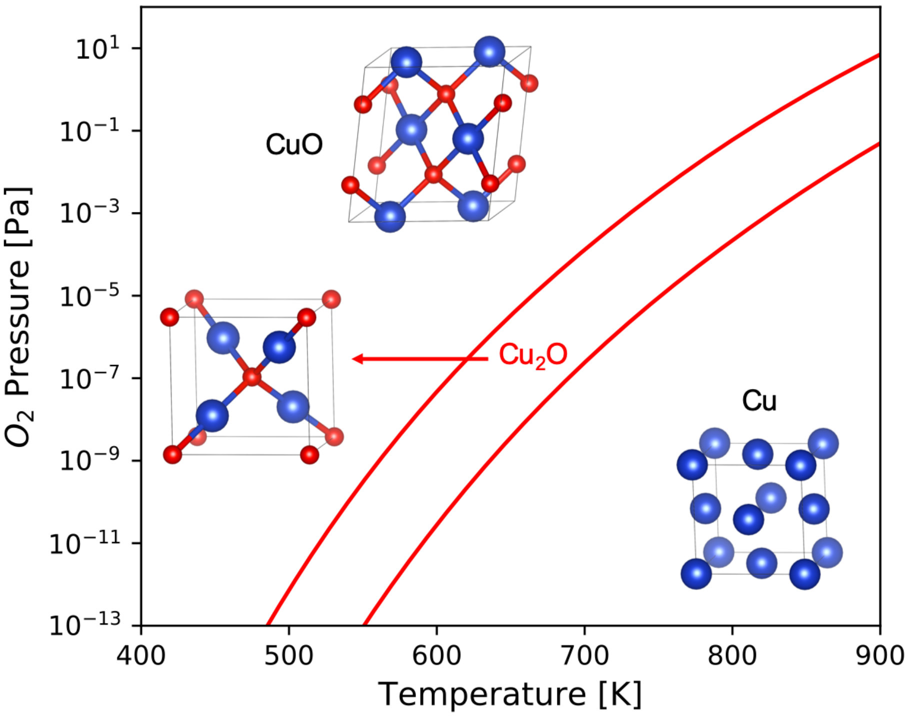

Figure 4.2: Thermodynamic stability region for Cu_2O in the (T, P) space. Cu_2O has a narrow stability region (bounded by the red lines) due to phase competition between CuO/Cu_2O and Cu_2O/Cu.

aries between CuO/Cu_2O and Cu_2O/Cu. This indicates the need to carefully control the temperature and the O_2 pressure during growth to obtain phase-pure Cu_2O. Previous experimental studies show that controlling the growth conditions of the Cu-O system is critical to obtaining the desired crystal orientation, stoichiometry, bandgap, hole concentration, mobility, and electrical conductivity.[66,102] Our calculated phase diagram agrees well with previous theoretical studies and experimental phase diagrams,[96,103] and can serve as a guide for future experimental synthesis.

4.4 Thermodynamics of intrinsic defects

Many of the electrical properties of Cu_2O are largely determined by the formation of intrinsic defects present in the crystal. We therefore calculated the formation energy for the most common isolated intrinsic defects in Cu_2O, namely the Cu vacancies (V_{Cu} and V_{Cu}^{split}), the Cu interstitial (Cu_i), the O vacancy (V_O), and the O interstitial (O_i). Figure 4.3-a shows their formation energy as a function of Fermi energy referenced to the VBM. Cu simple vacancies (Figure 4.3-b) and split vacancies (Figure 4.3-c) are the dominant defects with low formation energies for Fermi levels across the entire bandgap. Cu vacancies act as acceptors and render Cu_2O an intrinsic p-type semiconductor. The nature of simple versus the split vacancy is quite different. In contrast to previous claims that the split vacancy is more stable[81,84] or that the simple vacancy has a significantly lower formation energy,[82,83] our calculations show that the simple vacancy has a formation energy that is 0.12 eV lower than the split vacancy at the VBM, in agreement with the more recent calculations with the HSE06 hybrid functional by Isseroff and Carter.[86] Thus our results indicate that both vacancies are likely to form during the synthesis of Cu_2O, with the simple vacancy being slightly more stable.

The simple and split vacancies have evident differences in their charge-transition levels and charge localization. The simple vacancy has a (0/-1) charge-transition level

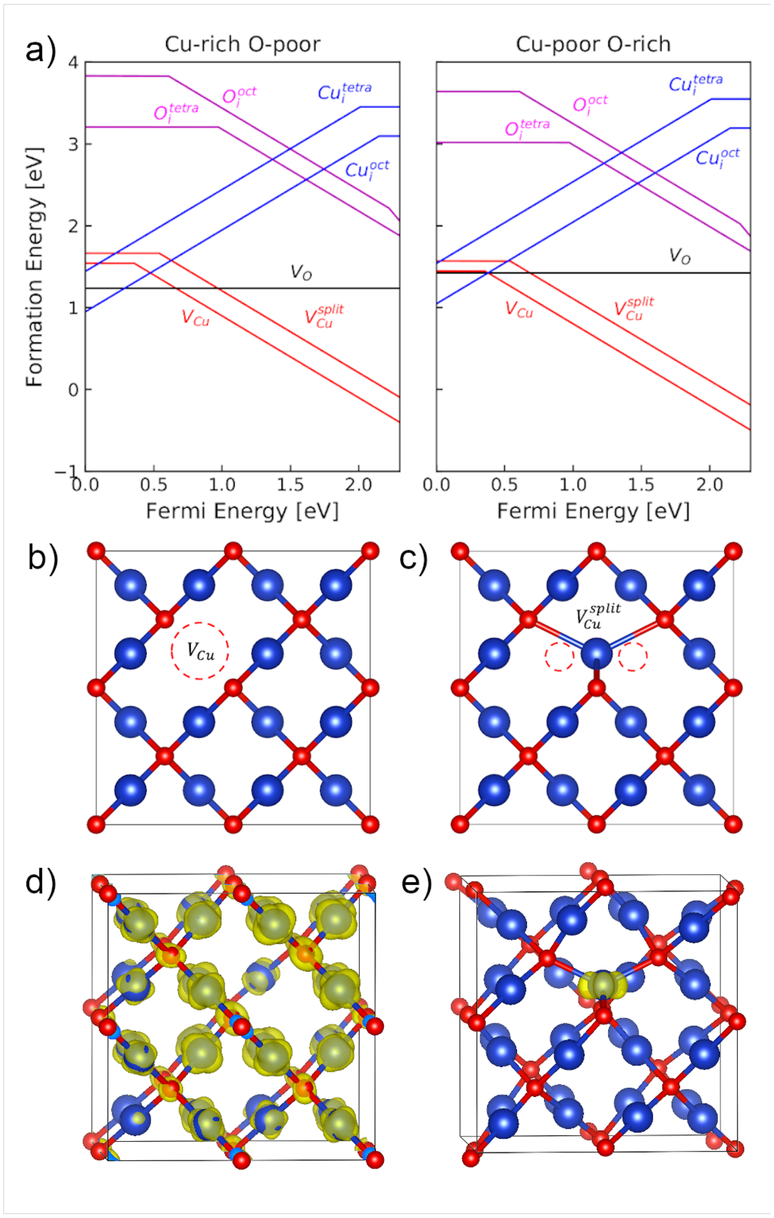

Figure 4.3: a) Formation energy of intrinsic defects in Cu_2O as a function of Fermi energy referenced to the valence band maximum. Cu_2O is an intrinsic p-type semiconductor due to the formation of Cu vacancies. b,c) Atomic configurations of the simple vacancy and the split vacancy, respectively. Blue atoms are Cu and red atoms are O. d,e) Spin charge density of the simple vacancy and the split vacancy in their neutral charge states, respectively. Isosurfaces for 10% of the maximum charge density is plotted. The hole carrier contributed by the simple vacancy is delocalized, whereas the hole bonded to the split vacancy is strongly localized on the Cu atom at the center of the split vacancy.

at 0.36 eV above the VBM whereas that of the split vacancy is at 0.54 eV. Both vacancies act as deep acceptors with relatively high ionization energies. These two levels are in good agreement with previous DLTS measurements that detect two distinct defect states at 0.25 eV and 0.45 eV.[76] Thus, we assign the 0.25 eV signal to the (0/-1) charge transition of the simple vacancy and the 0.45 eV level to the same transition for the split vacancy. A similar defect study by Scanlon *et al.* established such connections as well.[84] Further, we support this assignment using our temperature-dependent cryogenic measurements. The temperature-dependent current-voltage traces for the three samples are shown in Figure 4.4 (a-c). An Arrhenius activation energy (E_A) was extracted for each Cu_2O film, based on the TFT drain current in the off state, at $V_{GS} = 16$ V. The TFT off-state current is used because it represents conduction through the Cu_2O film in depletion. The equation used was

$$I_D = I_0 e^{-\frac{E_A}{k_B T}} \tag{4.2}$$

where I_D is the drain current, I_0 is a constant, k_B is the Boltzmann constant, and T is the temperature. In the $ln(I_D)$ vs. $1/k_B T$ curves (Figure 4.4 (d)), the slope indicates the activation energy E_A. E_A values obtained for samples S#1, S#2, and S#3 were 229 meV, 272 meV, and 479 meV, respectively. For comparison, the theoretically predicted ionization energies of a Cu simple vacancy and a Cu split vacancy are 360 meV and 540 meV, respectively. Therefore, we conclude that the Cu simple vacancy is dominant in the PVD samples (S#1 and S#2), while the Cu split vacancy is dominant in the ALD sample (S#3). The charge localization of Cu vacancies is shown in Figure 4.3-d and e. The hole contributed by the simple vacancy is much more delocalized than that from the split vacancy. We therefore find that the simple vacancy is more desirable than the split vacancy for more efficient acceptor ionization and hole transport in Cu_2O samples.

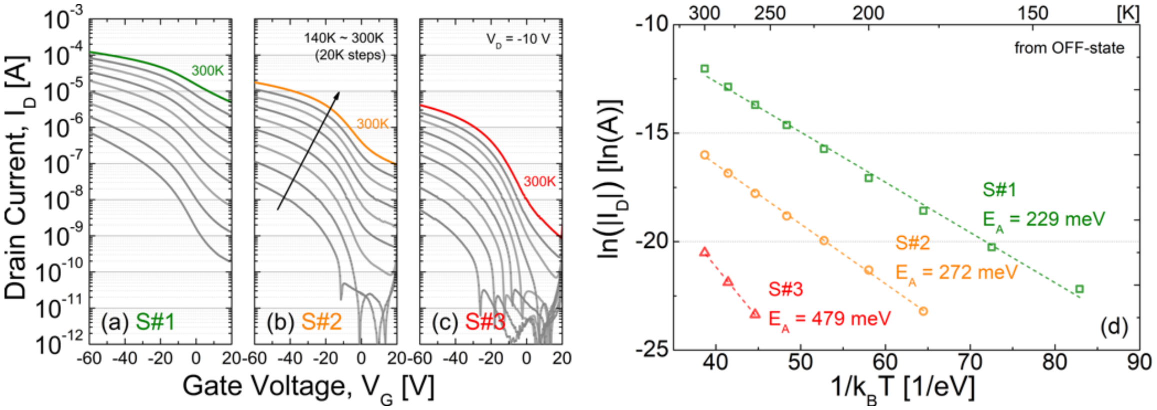

Figure 4.4: Drain current (I_D) versus gate voltage (V_G) curves at measurement temperatures from 140K to 300K, in 20K steps for (a) PVD Cu_2O sample S#1, (b) PVD Cu_2O sample S#2, and (c) ALD Cu_2O sample S#3. The drain voltage (V_D) is –10 V for all three TFTs. (d) $\ln(|I_D|)$ versus $1/k_BT$ plot. Data points in (d) were obtained from the curves in (a)-(c) at $V_{GS} = 16$ V. Dashed lines show fits to Arrhenius equations with activation energy E_A. The E_A values for S#1, S#2, and S#3 were extracted in the temperature ranges of 160 K–300 K, 180 K–300 K, and 260 K–300 K, respectively.

In terms of other isolated intrinsic defects, Cu_i and O_i have higher formation energy than the Cu vacancies. O_i have deep (0/-1) charge-transition levels of 0.61 eV for the octahedral site and 0.97 eV for the tetrahedral site. In contrast, octahedral Cu_i is a shallow donor with a (+1/0) charge-transition level right at the CBM, while tetrahedral Cu_i is a donor with a (+1/0) level at 0.14 eV below the CBM. Cu_i tends to occupy the octahedral site whereas O is more stable on the tetrahedral site. V_O is another intrinsic defect with low formation energy. However, our results show that V_O does not have charge-transition levels within the bandgap, indicating that V_O is only stable in its neutral state and does not act as a donor in Cu_2O, similar to what Allen *et al.* found for V_O in SnO.[104] Therefore, V_O does not compensate V_{Cu} acceptors.

Combining the formation energies for all intrinsic defects in Figure 4.3, we calculate the equilibrium hole concentration and Fermi level self-consistently using the SC-FERMI code.[105] The temperature dependence of these two properties is shown in Figure 4.5. As the growth temperature increases, more Cu vacancies are formed, generating more hole carriers in the valence band and shifting the Fermi level towards

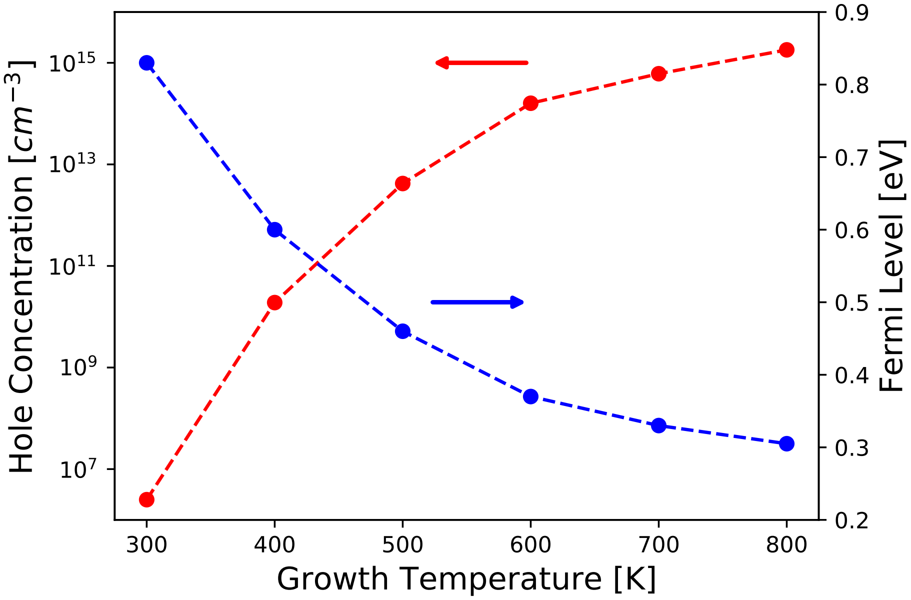

Figure 4.5: Theoretically calculated equilibrium room-temperature hole concentration and self-consistent Fermi level of Cu_2O as a function of the growth temperature. Intrinsic Cu_2O has a relatively low hole concentration and a Fermi level away from the VBM.

the VBM. The equilibrium hole concentration at 300 K is lower than 10^7 cm^{-3}. However, this assumes thermodynamic equilibrium for defect formation and neglects any kinetic effects. Experimentally, barriers may exist that prevent the annihilation of the point defects formed during growth due to slow kinetics, and the concentration of those point defects is effectively frozen. In this respect, it is reasonable to assume that the concentration of V_{Cu} at room temperature equals its equilibrium value at the growth/annealing temperature. This indicates that the hole concentration measured at room temperature should lie within these two extremes of 10^7 cm^{-3} and 10^{15} cm^{-3}, assuming a growth temperature of 800 K. Many experimentally measured hole concentrations for Cu_2O fall within this range.[106,107] Due to the high ionization energy of V_{Cu} acceptors and compensation by Cu_i donors, undoped Cu_2O has a low hole concentration and extrinsic doping may be necessary to tune the carrier concentration to an optimal level for electronic and optoelectronic applications.

4.5 Thermodynamics of H and C impurities

In addition to intrinsic defects, unintentional impurities can also play an important role in determining the electrical properties of oxide semiconductors. H is one of the most important impurity atoms for oxides due to the strong affinity of H to O ions. We therefore study H impurities at interstitial positions with various local configurations: H at an octahedral interstitial position (H_i^{oct}), H at a tetrahedral interstitial position (H_i^{tet}), H bonded to O at the Cu-O bond center (H_i^{BC}), and H bonded to O in the Cu-O antibonding configuration (H_i^{AB}). Their local structures are shown in Figure 4.6 a-d. In most oxide semiconductors, H is more stable when it is bonded to O, acting as either a H^+ donor or H^- acceptor. For example, ZnO is found to be natively n-type because the unintentional O-bonded H^+ donors have very low formation energy and donate electrons into the conduction band.[108,109] In contrast to other oxides, Cu_2O has two different stable configurations for H interstitials depending on the position of the Fermi level (Figure 4.6-e). Under heavy p-type doping conditions for which the Fermi level is near the VBM, H favors bonding with O in the antibonding configuration and acts as a H^+ donor, similar to the general behavior of cationic H in oxides. However, when the Fermi level lies away from the VBM, H is more stable in the tetrahedral site, coordinated with four Cu ions. Since Cu can take either of the +1 or the +2 charge states, H_i^{tet} shows three distinct behaviors, acting as an H^+ donor under p-type conditions, as an H^- acceptor under n-type conditions, and adopting the neutral state when the Fermi level is near the middle of the gap. By replacing one O ion, H can also act as a donor (H_O^+). Both interstitial and substitutional H act as deep donors under p-type conditions and compensate hole carriers, which decreases the equilibrium hole concentration of Cu_2O. Interstitial H can also passivate V_{Cu} by either replacing a Cu ion (H_{Cu}) or forming an $H_i - V_{Cu}$ defect complex, both of which are electrically neutral. Even though the presence of H impurities compensates hole carriers and increases the hole scattering from point

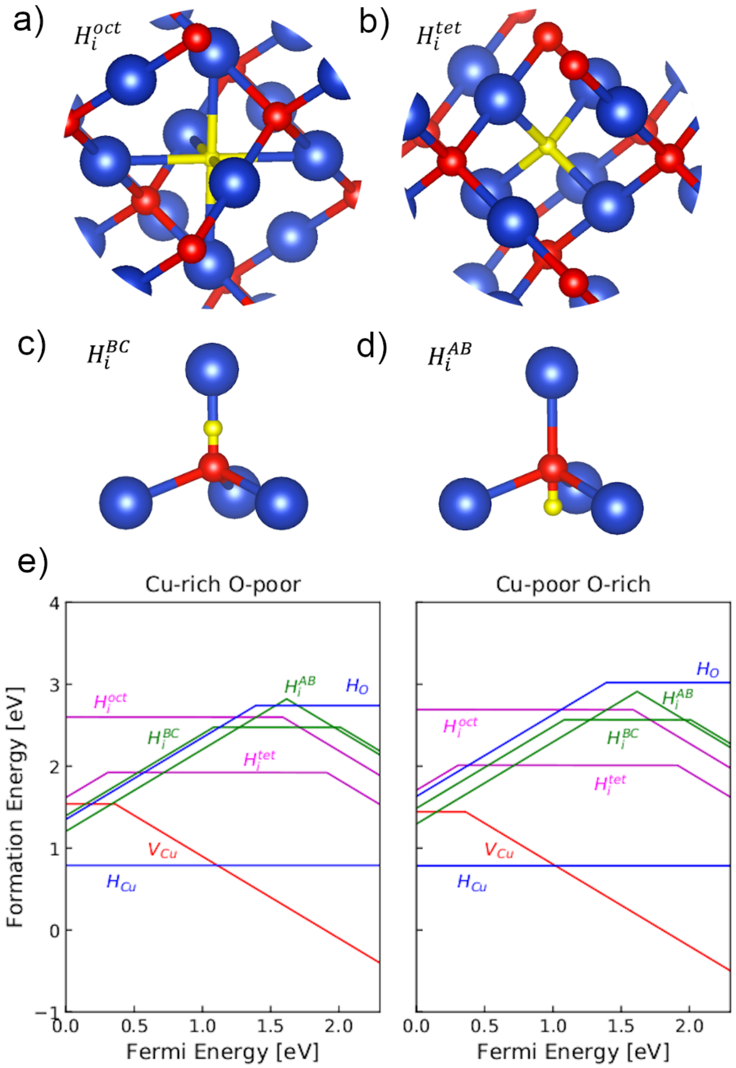

Figure 4.6: a-d) Local atomic structures of H interstitials in octahedral (H_i^{oct}), tetrahedral (H_i^{tet}), bond-centered (H_i^{BC}), and anti-bonding (H_i^{AB}) configurations, respectively. Blue atoms are Cu, red atoms are O, and yellow atoms are H. e) Formation energy of H impurities in Cu_2O as a function of Fermi energy referenced to the VBM. H interstitials act as compensating donors in Cu_2O.

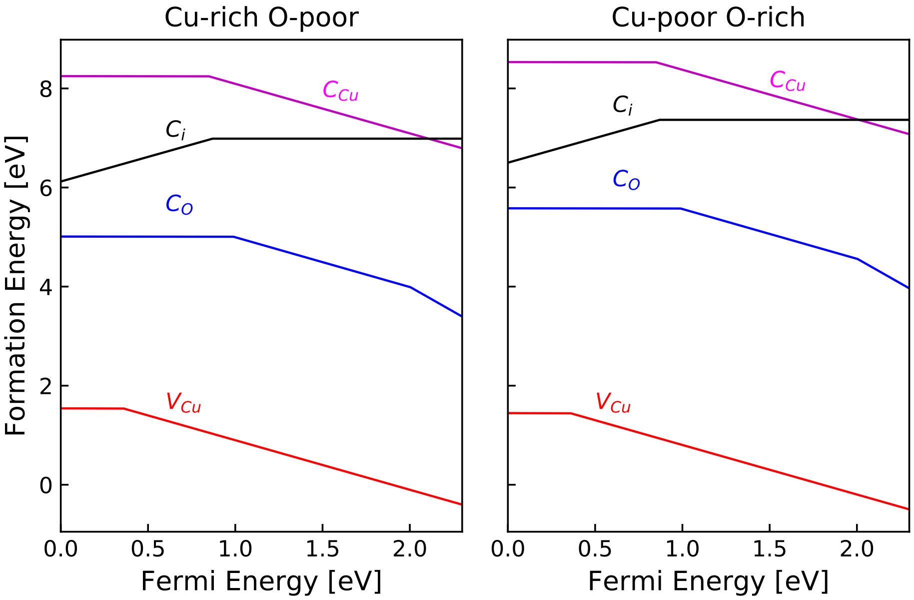

Figure 4.7: Formation energy of C impurities in Cu_2O as a function of Fermi energy referenced to the VBM. Substitutional C impurities are deep acceptors while C interstitials are deep donors in Cu_2O.

defects, it does not systematically lead to a mobility reduction in experimentally grown Cu_2O samples. In fact, previous experiments show that the Hall mobility of Cu_2O thin films can be enhanced under proper H treatment because H preferentially segregates at the grain boundaries of poly-crystalline thin films and passivates the dangling bonds, leading to reduced grain-boundary scattering.[110] Thus, controlling H can also be an effective way to tune the electrical properties of Cu_2O.

Besides H, C is another common impurity in oxide materials. We therefore study the formation of substitutional and interstitial C impurities in Cu_2O. Our results in Figure 4.7 show that C impurities lead to deep defect states. C_{Cu} and C_O are deep acceptors with ionization energies of 0.84 eV and 0.99 eV, respectively. Interstitial C acts as a deep donor with a $(+1/0)$ charge-transition level of 0.86 eV. While these mid-gap states may serve as non-radiative recombination centers, the formation energies of C impurities are much higher than the dominant V_{Cu} defect, indicating the difficulty of incorporating C into Cu_2O during growth. We therefore do not expect C impurities

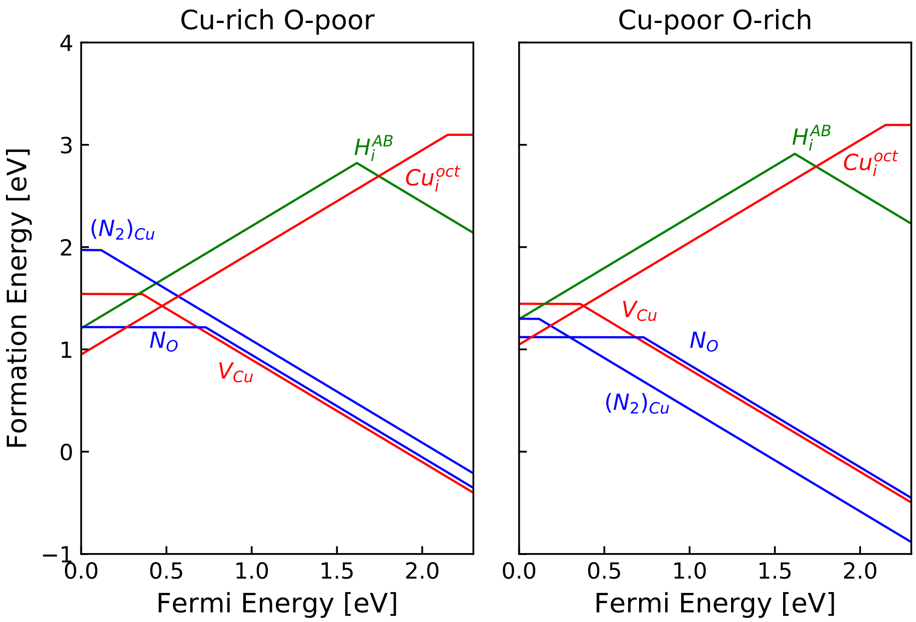

Figure 4.8: Formation energy of N dopants in Cu_2O as a function of Fermi energy referenced to the valence band maximum. The N chemical potential is set to be in equilibrium with the formation of Cu_3N phase. Using an activated N source (nitrogen plasma) and Cu-poor growth conditions could enable effective p-doping for Cu_2O with $(N_2)_{Cu}$.

to play a major role in hole transport in Cu_2O materials.

4.6 Investigation of candidate acceptors

Intrinsic Cu_2O has a relatively low hole concentration as we discussed in the previous section. To better control the electrical properties of Cu_2O, a systematic study of possible candidate impurities that can increase the hole concentration is needed. In this section, we discuss our calculations for candidate impurity atoms on both the anion and cation sites that may act as acceptors. On the O site, we focus on N, P, and S. On the cation site, divalent cations (Sn, Mg) are investigated.

Both N and P are group-V elements that have one less electron than O, indicating they may act as acceptors by replacing O. Using N_2 gas as the nitrogen source for doping, the formation energies of N defects are 0.5 eV higher than the dominant V_{Cu}

species (Figure B.4). This is due to the difficulty of breaking the strong N triple bond in N_2 molecules. However, the chemical potential of N can exceed its equilibrium value in N_2 during experiments by using an activated N source, for example nitrogen plasma. Under this condition, our calculated N chemical potential is $\mu_N = \triangle H(Cu_3N) - 3\mu_{Cu}$ $= 0.72$ eV, which greatly reduces the formation energy for N dopants, shown in Figure 4.8. This agrees with previous calculations by T-Thienprasert *et al.*[111] As expected, N_O acts an acceptor with a similar formation energy to V_{Cu} for the -1 charge state and a neutral state that is 0.4 eV lower in energy. Despite its small formation energy, N_O acts as a deep acceptor with a high ionization energy of 0.73 eV. This greatly decreases the fraction of holes that can be activated into the valence band by N_O. Another possible acceptor state occurs when the N dimer replaces Cu $[(N_2)_{Cu}]$.[111] The nominal charge is 0 for the N dimer and +1 for the Cu ion. Therefore, $(N_2)_{Cu}$ can act as a singly charged acceptor in Cu_2O. Figure 4.8 shows that $(N_2)_{Cu}$ is a much shallower acceptor than N_O with an ionization energy of only 0.11 eV. Under Cu-poor conditions and with activated N, $(N_2)_{Cu}$ has even lower formation energy than V_{Cu} and N_O, and experiences weak compensation from H_i and Cu_i. Successful N doping in Cu_2O has been realized in numerous experimental studies,[112,113] which show that the hole concentration can be enhanced by several orders of magnitude. In addition, previous Raman measurements[114] show that both $(N_2)_{Cu}$ and N_O are likely present in N-doped Cu_2O, which further supports our calculations. Thus, activated N can be an effective acceptor in Cu_2O.

While N dopant is effective, anion doping with P, another group V element, does not show any promise. Figure 4.9 shows the formation energy of substitutional and interstitial P in Cu_2O. A distinct feature for P-related defects is that their formation energies are extremely high, indicating the difficulty of incorporating P into Cu_2O. This is probably due to the fact that P does not prefer the tetrahedral coordination environment of Cu, nor does it maintain a coordination number of two like O in Cu_2O.

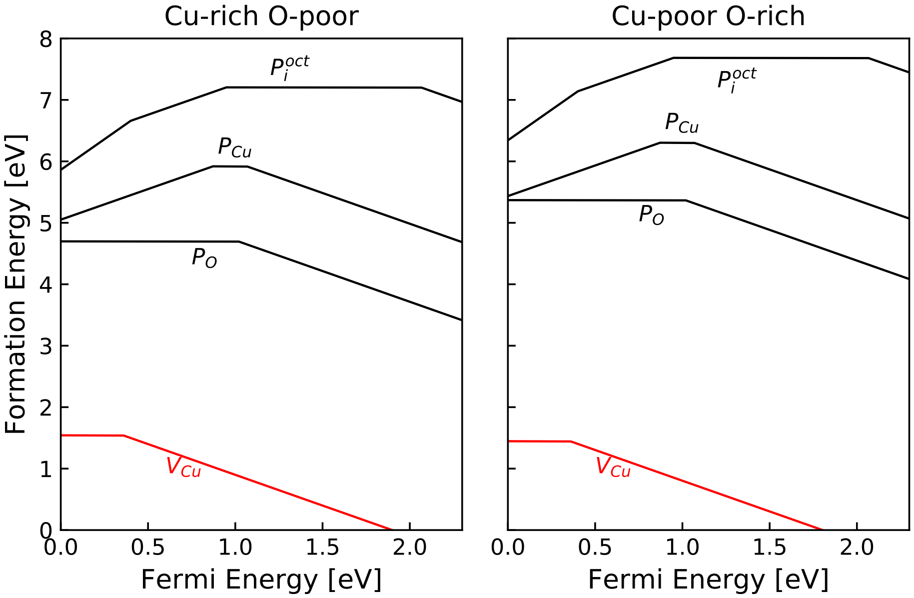

Figure 4.9: Formation energy of P dopants in Cu_2O as a function of Fermi energy referenced to the valence band maximum. P incorporation into Cu_2O is difficult due to its very large formation energy compared to the dominant intrinsic Cu vacancies.

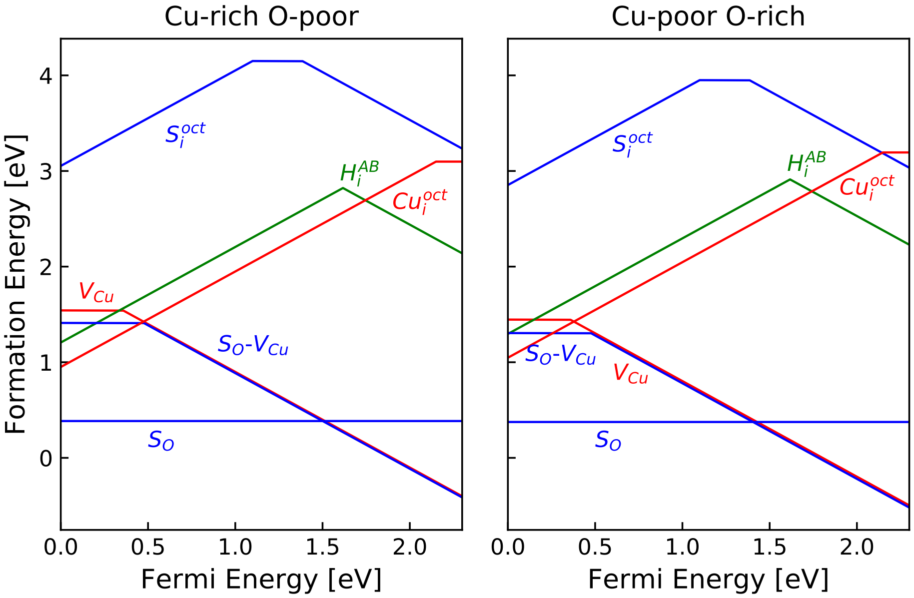

Figure 4.10: Formation energy of S dopants in Cu_2O as a function of Fermi energy referenced to the valence band maximum. The substitution of O by S can promote the formation of Cu vacancies in Cu_2O.

The last candidate dopant on the anion site that we study is S. The intuition behind p-doping with S lies in the fact that Cu_2S has a higher hole concentration than Cu_2O, typically on the order of 10^{19} cm^{-3}.[115,116] We hypothesize that substituting a fraction of O by S will promote the formation of V_{Cu}, thereby increasing the acceptor and hole concentrations. Our results in Figure 4.10 show that S incorporation onto the O site is relatively easy due to the small formation energy of only 0.4 eV for S_O. S_O is electrically neutral because S and O have the same number of valence electrons. S_O interacts with V_{Cu} by forming a defect complex ($S_O - V_{Cu}$) with a binding energy of 0.5 eV. This defect complex has a (0/-1) charge-transition level of 0.48 eV and acts as a deep acceptor. The negative binding energy of the defect complex ($S_O - V_{Cu}$) may originate from the relaxation of local strain induced by S_O enabled by the formation of a nearby V_{Cu}. This supports our hypothesis that S incorporation promotes the formation of V_{Cu} and forms a stable defect complex, which can enhance the p-type conductivity of Cu_2O.

Proposing candidate dopants for the anion site is much more straightforward than for the cation site. Since Cu has +1 valence charge, p-dopant on Cu site should have a nominal charge of 0, which has only been demonstrated with previously mentioned $(N_2)_{Cu}$ acceptors. Similar to the mechanism of S doping, another doping strategy is to introduce cation dopants into Cu_2O that promote the formation of V_{Cu} acceptors. In the early theoretical study by Nolan and Elliot, substituting the Cu^+ ion with a divalent cation (Ba^{2+}, Sn^{2+}, Cd^{2+}, etc.) induces large, localized structural distortions accompanied by the formation of a double V_{Cu} defect. The first copper vacancy passivates the II^+_{Cu} defect, while the second vacancy acts as an acceptor.[117] To get further insights into divalent cation doping in Cu_2O, we calculate the formation energy of Sn and Mg dopants, shown in Figure 4.11.

As expected, replacing Cu with divalent cations, i.e. Sn_{Cu} and Mg_{Cu}, creates donor states in the bandgap. Both donors are deep with high ionization energies.

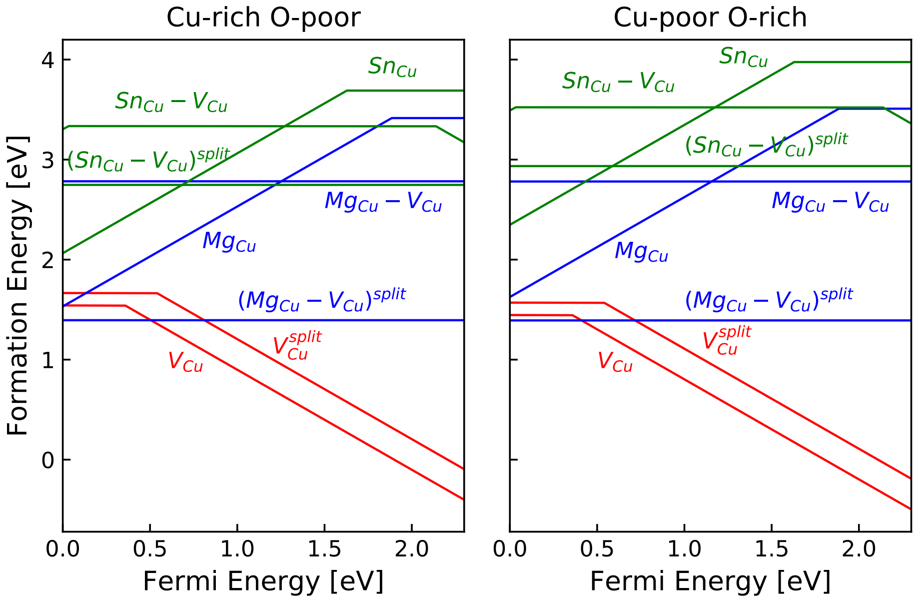

Figure 4.11: Formation energy of divalent cation dopants (Mg and Sn) in Cu_2O as a function of Fermi energy referenced to the valence band maximum. Divalent cations passivate the split vacancies and promote the formation of simple vacancies.

However, it is thermodynamically more favorable for Sn_{Cu} and Mg_{Cu} to be passivated by a simple vacancy or a split vacancy to form a stable neutral defect complex. Interestingly, the formation energy of $(Sn_{Cu} - V_{Cu})^{split}$ is 0.6 eV lower than $(Sn_{Cu} - V_{Cu})$ and the formation energy of $(Mg_{Cu} - V_{Cu})^{split}$ is 1.4 eV lower than $(Mg_{Cu} - V_{Cu})$. This can be explained by the fact that Mg and Sn have a +2 nominal charge and they are more stable when bonded to four O atoms in the center of the split vacancy than to two O atoms in the center of the simple vacancy to maintain charge balance. However, Sn incorporation is not promising for enhancing p-type conductivity due to the large formation energy for Sn-related defects. Previous experiment on Sn incorporation into Cu_2O focuses on the impact on the bandgap but not carrier concentration. In contrast, Mg seems to hold promise in p-doping for Cu_2O. The formation energy of $(Mg_{Cu} - V_{Cu})^{split}$ is lower than the dominant Cu vacancies, and its binding energy is 1.7 eV. This implies that Mg can passivate the formation of the localized split vacancy. During annealing, the desired simple vacancies, which are more delocalized, will be more likely to form than the localized split vacancies, contributing more hole carriers. This observation is consistent with recent experiments on Mg-doped Cu_2O where the hole concentration increases by one order of magnitude upon 2% Mg doping.[118]

4.7 Conclusions

In summary, we perform a comprehensive study on the thermodynamics of intrinsic defects, common impurities, and candidate acceptors in Cu_2O using hybrid DFT calculations and temperature-dependent experiments. The two most dominant intrinsic defects for Cu_2O are the Cu simple vacancy and split vacancy, with calculated ionization energies of 0.36 eV and 0.54 eV, respectively. These two acceptor states are identified by the good agreement between our calculated ionization energies and our experimentally-measured activation energies of 272 meV and 479 meV. Intrinsic Cu_2O has a relatively low hole concentration and extrinsic dopants are needed to increase the concentration of the hole carriers. Our calculations indicate that N, S, and Mg can be effective p-dopants by promoting the formation of V_{Cu}, whereas P and Sn are not promising due to their high formation energies. Our work presents a holistic view of the defect thermodynamics of Cu_2O and provides useful insights for engineering the defect properties of Cu_2O to enable its use in a broad range of functional applications.

CHAPTER V

Impact of Cation Disorder on the Thermodynamic and Electronic Properties of II-IV-N_2 Semiconductors

5.1 Introduction

III-N materials have achieved great success in numerous semiconductor functional applications, such as high efficiency light-emitting diodes,[119] high electron mobility transistors,[120] etc. Recently, II-IV-N_2 attracts great research interests for their interesting electronic and optoelectronic properties. II-IV-N_2 has the same underlying wurtzite crystal structure as many III-N materials except that two group-III cations are replaced by a group-II cation and a group-IV cation, which still maintains charge balance. Due to this cation substitution, the lattice is reduced from hexagonal symmetry to orthorhombic symmetry. In addition, two cation species with different formal charge introduce another degree of freedom by allowing disorder in the cation sublattice. As a result, the local bonding environment of N atom can vary drastically depending on its 4 nearest cation neighbors, which leads to different structural motifs. For example, the N is bonded to 2 group-II cations and 2 group-IV cations at the ground state (2-2 motifs). It is also possible for N to bond to 3 group-II cations and 1 group-IV cation (3-1 motifs), or even to 4 group-II cations (4-motifs), and vice versa.

Naturally, this cation disorder and structural motifs can have large impact on the thermodynamic stability and electronic properties of II-IV-N_2. The effect of disorder has been studied for $ZnSnN_2$ by previous studies. Feldberg *et al.* performed DFT calculations using the PBE0 functional and found that the fully-ordered $ZnSnN_2$ has a bandgap of 2.09 eV whereas the cation disorder reduces the bandgap dramatically to 1.12 eV. They also synthesized the $ZnSnN_2$ thin film and observed the lowering of the absorption onset.[121] Quayle *et al.*, on the other hand, argued that disorder does not change the bandgap much as long as the crystal structure only consists of octet-rule conserving 2-2 motifs. The other 3-1 motifs and 4-motifs causes a significant increase in energy.[122] This issue is further elaborated by the Monte-Carlo simulations performed by Lany *et al.* that 4-motifs are thermodynamically unfavorable and unlikely to form even at very high temperature. However, they did observe the bandgap narrowing of $ZnSnN_2$ by cation disorder.[123] Whether the bandgap variation arises from the presence of cation disorder remains controversial. Another opinion is based on the fact that the as synthesized $ZnSnN_2$ suffers from severe unintentional n-type doping by Sn_{Zn} antisite defects and thus a large free electron concentration on the order of 10^{20} cm^{-3}. As a result, the optical bandgap shifts to higher energy, an effect known as Burstein-Moss shift. Early $ZnSnN_2$ experiments measured a bandgap near 2 eV. Considering the Burstein-Moss shift, the real bandgap of $ZnSnN_2$ may be 1.4 eV.[124]

In this work, we seek to shed light on the effect of cation disorder on the thermodynamic and electronic properties of II-IV-N_2, taking $ZnSnN_2$ as a model system. By employing density functional theory calculations on various disorder $ZnSnN_2$ supercells, we find that 4-motifs are very unfavorable from the thermodynamic standpoint and that the energy of the $ZnSnN_2$ increases with the fraction of 3-1 motifs. We also find that the bandgap decreases with increased disorder and that the bandgap is proportional to the square of the long-range order parameter. In addition, we investigate the cation disorder into a broader set of II-IV-N_2 materials and discover that cation size mismatch is a good metric to determine the tendency toward disorder in II-IV-N_2 systems. Therefore, rational control of the degree of disorder can be achieved through choosing the desired pair of cations.

5.2 Computational methods

The thermodynamic and electronic properties of $ZnSnN_2$ and other II-IV-N_2 materials were studied by density functional theory calculations using the projector-augmented wave method[26] as implemented in the Vienna *ab initio* Simulation Package (VASP).[27] PBE pseudopotentials[14] were employed with a plane-wave cutoff energy of 500 eV, which converged the total energy to 10 meV/f.u. To address the bandgap underestimation problem of semilocal functionals, we employed the HSE06 hybrid functional[16] with a mixing parameter of 0.31 for $ZnSnN_2$ studies. For a systematic analysis of the cation disorder and thermodynamic properties for a broad range of II-IV-N_2, a mixing parameter of 0.25 was used to get a consistent treatment across all materials. $4 \times 4 \times 4$ k-point grids[32] were used to sample the Brillouin zone of primitive cells of space group $Pna2_1$. Partially ordered $ZnSnN_2$ was modeled with a 2x2x2 supercell (128 atoms) and the Brilloin zone was sampled using only the Γ point to reduce the computational cost. The cation disorder was included by swaping cation pairs and we discarded the supercell with 4-motifs. For comparison, special quasi-random structure was generated with the Alloy Theoretic Automatic Toolkit (ATAT).[33] All structure are fully relaxed. Bandgaps were calculated by the difference between the conduction band minimum and the average of the top 3 valence band eigenvalues.

5.3 Cation disorder and thermodynamic properties

To study the cation disorder in II-IV-N_2 materials system, we need to quantify this property. The most common method is to use the long-range order parameter S, which is defined as

$$S = r_\alpha + r_\beta - 1 \tag{5.1}$$

where r_α is the fraction of group-II site that is occupied by group-II cations and r_β is the fraction of group-IV site that is occupied by group-IV cations. In the fully order structure, all group-II sites will be occupied by group-II cation and vice versa. Then $r_\alpha = r_\beta = 1$ and $S = 1$. In the fully disorder structure, each cation site will be equally probable to be occupied by group-II or group-IV atoms. Therefore, $r_\alpha = r_\beta = 0.5$ and $S = 0$. In the stoichiometric materials, $r_\alpha = r_\beta = r$ and $S = 2r - 1$.

From long-range order parameter, we can derive the fraction of 2-2, 3-1, and 4-motifs using probability. Figure 5.1 shows the fractions of various motifs as a function of the order parameter. For the perfect ordering, crystal structure only has the octet-rule conserving 2-2 motifs. As $ZnSnN_2$ becomes more disorder, i.e. smaller S, the fraction of 3-1 and 4-motifs increases. Note that this ignores any thermodynamic penalty associated with each motif and only considers the probability. However, 3-1 motifs and 4-motifs break the local charge neutrality surrounding the N atoms and are expected to significantly increase the total energy of the system.

To investigate the thermodynamic effect of disordering, we generated the random structures using 128-atom supercells with long-range order parameter S to be 0.25, 0.5 and 0.75. Since the random statistics cannot be fully captured by a single supercell, 7 random supercells were generated for each S value, including one special quasirandom structure (SQS) that allows the presence of 4-motifs. The formation energies of these random structures with respect to the order $ZnSnN_2$ are shown in Figure 5.2. A distinct feature is that the SQS has the highest formation energy among

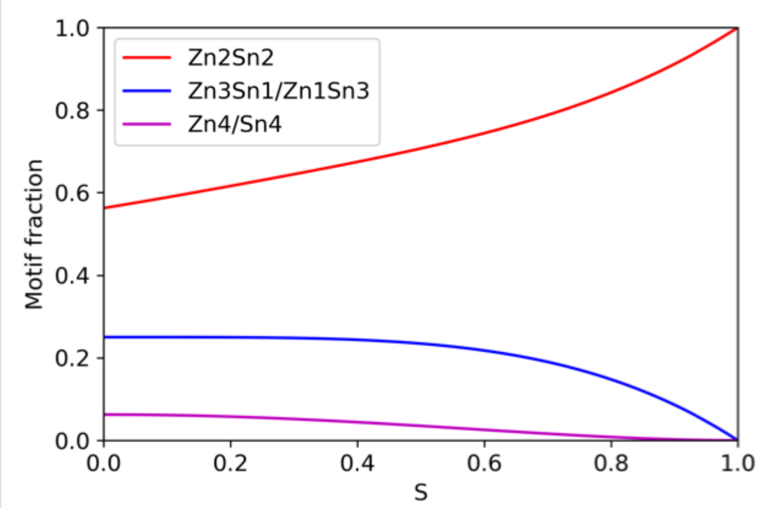

Figure 5.1: Motif fraction in $ZnSnN_2$ as a function of long-range order parameter S. As $ZnSnN_2$ becomes more disorder, the fraction of octet-rule violating 3-1 motifs and 4-motifs increases.

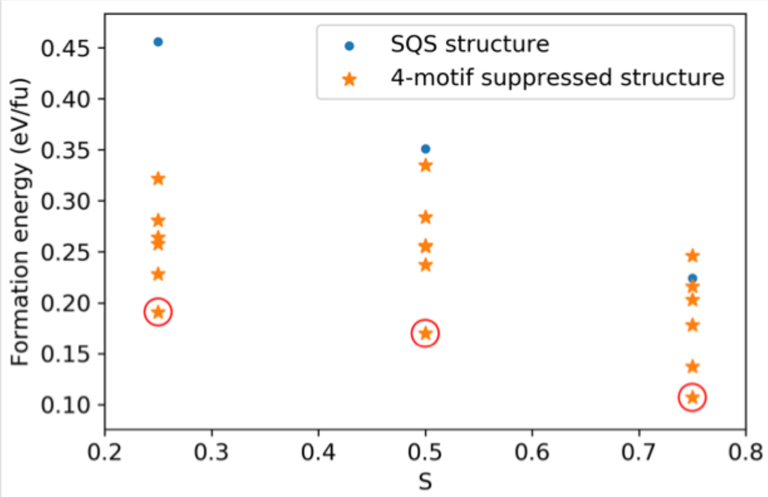

Figure 5.2: Formation energies of random $ZnSnN_2$ with respect to the ordered groundstate. SQSs are very unfavorable due to the presence of 4-motifs. Red circle indicates the most stable structure for each S value.

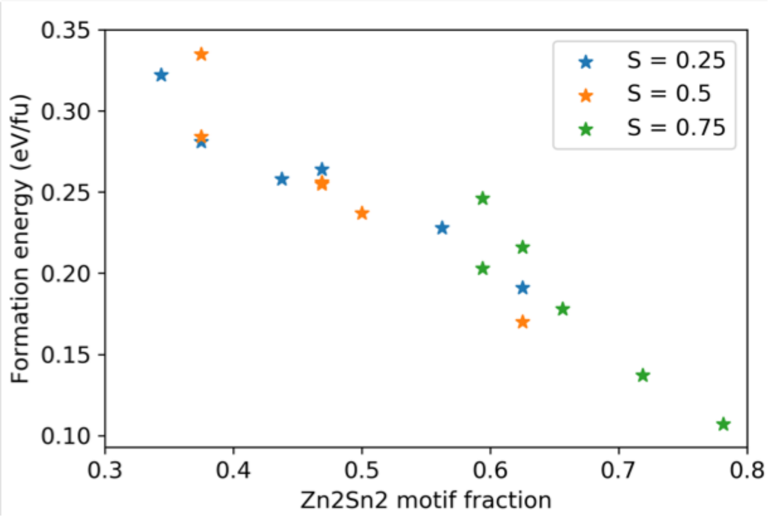

Figure 5.3: Formation energies of random $ZnSnN_2$ as a function of the fraction of 2-2 motifs. For each S value, the random structures tend to maximize the fraction of the octet-rule conserving motifs.

all structures except for $S = 0.75$. The only difference is that SQSs have 4-motifs whereas other random structures do not. This implies that Zn4 and Sn4 motifs are thermodynamically unfavorable to form. On the other hand, while 3-1 motifs were shown to be possible by previous Monte-Carlo simulations,[123] they will still increase the total energy of the system. The dependence of the formation energy on the motif fraction is shown in Figure 5.3. For each S value, the formation energy decreases with the fraction of 2-2 motifs. This can be explained by the fact that only 2-2 motif obeys the octet rule, which does not cause a large thermodynamic penalty. The more 2-2 motifs means the less 3-1 motifs and smaller penalty. Therefore, random structures tend to maximize the fraction of 2-2 motifs and obey the octet rule, which is consistent with the argument by Quayle *et al.*[122]

5.4 Cation disorder and electronic properties

We then turn to the effect of cation disorder on the electronic properties of $ZnSnN_2$, focusing on the bandgap. We calculated the bandgap of disorder $ZnSnN_2$ with differ-

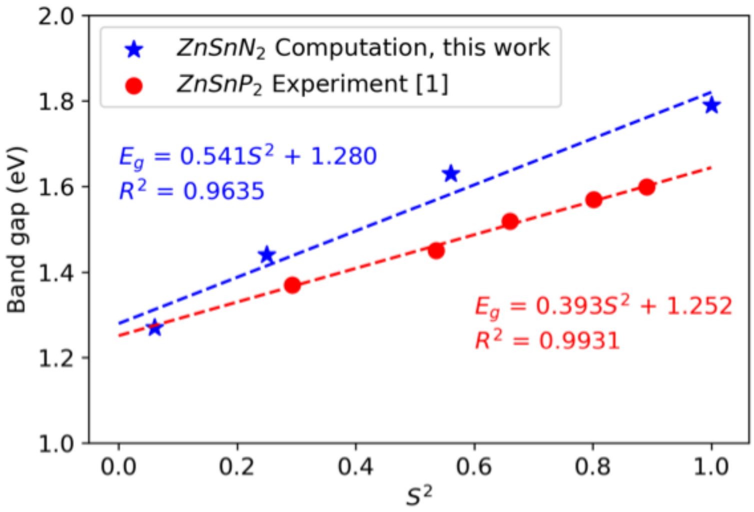

Figure 5.4: Bandgap of partially disordered $ZnSnN_2$ calculated from the HSE06 hybrid functional. The bandgap decreases with the degree of disorder for $ZnSnN_2$, and it is proportional to S^2.

ent S value. For each S value, we chose the random structure that has the highest 2-2 motif fraction due to their lowest formation energy. The bandgap of partially disordered $ZnSnN_2$ is shown in Figure 5.4, where the bandgap decreases with an increased degree of disorder, i.e. a smaller S value. Since a smaller S value correlates to a smaller 2-2 motif fraction, the bandgap shrinks as a result of a decreased fraction of the octet-rule conserving 2-2 motif, which is consistent with what Lany *et al.*[123] found in their motif-based Monte-Carlo simulation. Moreover, we discovered that the bandgap follows a linear relationship with the square of the long-range order parameter S. We fitted the data points with the following linear equation.

$$E_g(S^2) = \Delta E_g \cdot S^2 + E_g(S^2 = 0) \tag{5.2}$$

For $ZnSnN_2$, the fitted ΔE_g is 0.51 eV, which implies that Zn/Sn disorder can reduce the bandgap by 0.51 eV when the cation sublattice goes from perfect order to completely disorder. The magnitude of bandgap reduction is smaller than what Feldberg *et al.* found in their PBE0 calculation.[121] This is due to the fact that they used SQS to model the disorder structure, which allows the thermodynamically unfavorable 4-motifs. In fact, we also found that 4-motifs significantly shrinks the bandgap in our SQSs for disorder $ZnSnN_2$.

Interestingly, the linear relationship between the bandgap and S^2 holds in a wide range of heterovalent ternary alloys from our own experiments,[125] including $ZnSnN_2$, $ZnGeN_2$, $ZnSnP_2$, $GaInS_2$, $MgSnN_2$, etc. We explain the narrower bandgap from the interaction of the structural motifs and orbital electrons. Take $ZnSnN_2$ as an example. The formal charge is +2 for Zn, +4 for Sn, and -3 for N, respectively. Therefore, Zn3Sn1 motifs are negatively charged whereas Zn1Sn3 motifs have positive charge. For $ZnSnN_2$, the valence band maximum (VBM) is derived from N $2p$ orbital and the conduction band minimum (CBM) is derived from Sn $5d$ orbital. The CBM is thus pulled down by the Coulombic attraction between the positively charged Zn1Sn3 motifs and the orbital electrons. On the other hand, the VBM gets pushed up by the Coulombic repulsion between negatively charged Zn3Sn1 motifs and the electrons at the VBM. A decrease of CBM and an increase of VBM cause a reduction on the bandgap. As $ZnSnN_2$ becomes more disordered, the fraction of 3-1 motifs increases from Figure 5.1, which leads to larger Coulombic interaction and thus smaller bandgap.

5.5 Cation size mismatch and tendency towards disorder

So far, we have studied the effect of cation disorder on the thermodynamic stability and the bandgap of $ZnSnN_2$. While cation disorder can have interesting application such as engineering the bandgap without alloying, it is more desirable to have ordered materials especially for electronic applications due to their better transport properties. However, the as-synthesized II-IV-N_2 materials can often exhibit cation disordering, which has been shown in previous experiments on $ZnSnN_2$, $ZnGeN_2$, and $MgSnN_2$. It is therefore crucial to investigate how to rationally control the degree of disorder

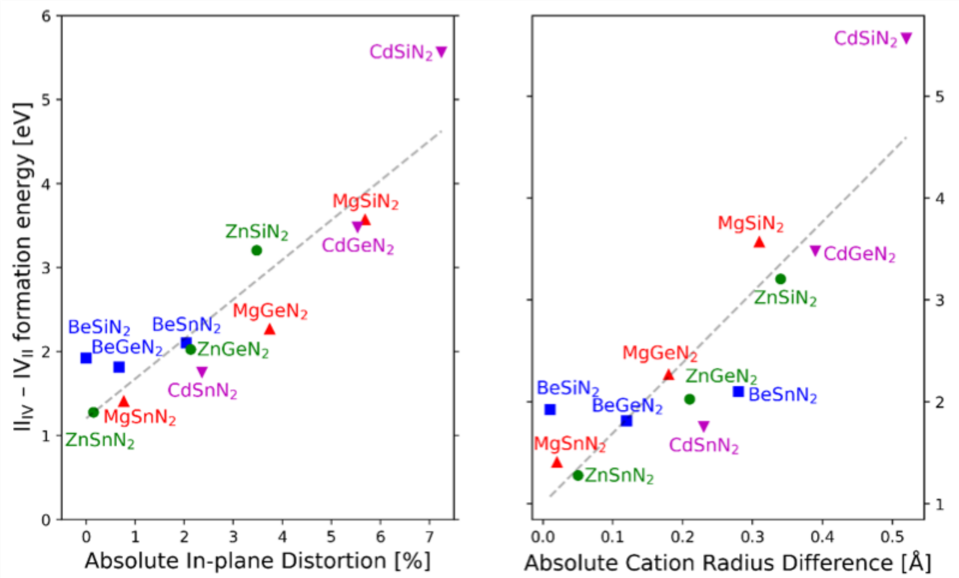

Figure 5.5: Formation energy of cation antisite pairs as a function of in-plane distortion and cation radius difference. A strong positive correlation exists between antisite pair formation energy and the size mismatch.

in II-IV-N_2 materials system.

The cation disorder in II-IV-N_2 can be viewed as progressively swaping group-II cations with group-IV cations. Swaping a single cation pair creates a $II_{IV} - IV_{II}$ antisite pair defect complex and thus the formation energy of this defect complex indicates the difficulty for this II-IV-N_2 to exhibit cation disordering. Intuitively, the size difference between the group-II and group-IV cations correlates to the formation energy of the antisite pairs and ultimately to the tendency towards disorder. Therefore, we calculated the cation antisite pair formation energy for a broad range of II-IV-N_2 and investigate their correlation with the size mismatch.

We use the $|r_{II} - r_{IV}|$ to quantify the size mismatch between the cations, where r_{II} and r_{IV} are the Shannon ionic radius[126] for the group-II and group-IV cations, respectively. Due to the size difference and the heterovalency of the cation pair, the wurtzite basal plane of II-IV-N_2 will have in-plane distortion, deviating from the perfect hexagon of the lattice with ideal hexagonal symmetry. We therefore use the following quantity to measure in-plane distortion. a and b are the lattice constants of the orthorhombic unit cell of II-IV-N_2 with space group $Pna2_1$.

$$\frac{\frac{a}{b} - \frac{\sqrt{3}}{2}}{\frac{\sqrt{3}}{2}} \times 100\% \tag{5.3}$$

Figure 5.5 shows the strong linear correlation between the antisite pair formation energy and the in-plane lattice distortion and the size mismatch, indicating that the large size mismatch prevents swaping of the cation pairs and thus suppresses the degree of disorder in II-IV-N_2. Since each cation swap corresponds to the formation of a $(II)_1$-$(IV)_3$ motif and a $(II)_3$-$(IV)_1$ motif, a larger lattice distortion and a higher antisite pair formation energy implies a decresed fraction of 3-1 motifs and a increased fraction of 2-2 motifs. Interestingly, each series of materials with a common group-II cation (e.g., Be-IV-N_2, Mg-IV-N_2) appears to follow slightly stronger linear trends, the slope of which correlates with the size of the group-II atom. The Be-IV-N_2 materials have a very small slope, roughly outlining a horizontal line, corresponding to the small ionic radius of beryllium (0.27 Å). Cadmium has a large ionic radius (0.78 Å), and the Cd-containing materials outline a steeper line than the trend for all 12 materials. Mg-IV-N_2 and Zn-IV-N_2 materials do not differ noticeably in their trends, as their group-II ionic radii are nearly identical (0.57 and 0.60 Å, respectively). The series formed by each group-IV cation (e.g., II-Si-N_2) do not display as strong trends as their group-II counterparts, most likely because the group-II ions are all larger than the group-IV ions in this study, apart from beryllium, which is approximately equal in size to Si (0.26 Å) and smaller than Ge and Sn (0.38 and 0.55 Å, respectively). Because of this exception, we note that Be-IV-N_2 does not strictly follow the positive linear trend of the other materials. Due to the strong linear correlation, we believe that the cation size mismatch is a good metric to predict the tendency of II-IV-N_2 to exhibit disordering on the cation sublattice, which allows rational control on the cation disorder through choosing the desired pair of cations.

5.6 Conclusions

In conclusion, we study the effect of cation disorder on the thermodynamic and electronic properties of II-IV-N_2 semiconductors. Instead of the long-range disorder, we find that the cation disorder in the short range, i.e. the structural motifs, determines the thermodynamic stability and the bandgap. 4-motifs are thermodynamically unfavorable whereas 3-1 motifs have small thermodynamic penalty and can be formed in experiments. The bandgap of II-IV-N_2 is linearly proportional to the square of the long-range order parameter, which implies the possibility to engineer the bandgap of semiconductor without alloying. Despite the interesting effect on the bandgap, cation disordering is often considered to have negative impact on the transport properties of semiconductors. We propose the cation size mismatch as a good indicator to measure the tendency of II-IV-N_2 towards disorder. Therefore, choosing the desired pair of cations can realize the rational control of cation disordering in a broad range of heterovalent ternary semiconductors.

CHAPTER VI

Semiconducting High-Entropy Chalcogenide Alloys with Ambi-ionic Entropy Stabilization and Ambipolar Doping

6.1 Introduction

Materials design by entropy stabilization has proven an efficient approach to engineer new materials with unique properties. Entropy stabilization exploits the large configurational entropy of multiprincipal-element alloys to overcome the mixing-enthalpy barrier and stabilize solid solutions of otherwise immiscible materials in simple crystal structures. Early work focused on metals[127–129] and demonstrated their superior mechanical behavior[130,131] and corrosion resistance.[132] Subsequently, the principle of entropy stabilization was demonstrated to also apply to ceramics[133–137] such as (Mg, Co, Ni, Cu, Zn)O,[133] which form a rocksalt solid solution even though the constituent binaries crystallize in different crystal structures. Besides early emphasis on mechanical behavior, high entropy materials have also shown intriguing functional properties such as superconductivity,[138] colossal dielectric constant,[139] reversible energy storage,[140] etc. These results hinted at the possibility that, other than metals and ceramics, entropy-stabilized materials can be deployed in electronic applications.

Despite the recent progress in the field, entropy-stabilized alloys with semiconducting character, that is, exhibiting a band gap and controllable ambipolar doping, have not been demonstrated. Semiconductors are important for a broad range of applications such as transistors,[141] solar cells,[142] and energy conversion.[143] Alloyed semiconductors in particular enable the engineering of their structural and functional behavior through chemical substitution to realize desirable structural and functional properties (e.g., lattice matching to a substrate,[144] tuned optical emission,[145] increased carrier mobility,[146] low thermal conductivity,[147] etc.). However, many semiconductor applications are limited by alloy phase segregation or the high temperatures needed for semiconductor growth. Entropy stabilization is thus a promising method to overcome the solubility limits of traditional semiconductor alloys, lower their processing temperatures, and synthesize new semiconducting materials with targeted functionalities.

Configurational disorder has been explored in the conventional as well as the multiprincipal-element chalcogenide alloys to engineer their structural and functional properties. For example, chalcogenide compounds show great promise in thermoelectric energy conversion, and doping engineering has been applied over the years to improve the thermoelectric performance of materials such as the established $Bi_2(Te,Se)_3$ alloys and the more recently developed Sn(S,Se) and GeTe phases.[148–152] Furthermore, recent work focused on enhancing the thermoelectric power factor and lowering the lattice thermal conductivity by introducing configurational entropy through doping or alloying,[153] such as in $Ge_{0.84}In_{0.01}Pb_{0.1}Sb_{0.05}Te_{0.997}I_{0.003}$,[154] PbSnTeSe,[155] PbTe-PbSe-PbS,[147] and $(Sn_{0.7}Ge_{0.2}Pb_{0.1})_{0.75}Mn_{0.275}Te$,[156] to name a few. While entropy does play an important role in stabilizing these alloys and controlling their properties, these systems are not classified as high-entropy alloys because their stoichiometry is far from the equimolar ratio and their configurational entropy is lower than 1.61 $R{\cdot}\mathrm{mol}^{-1}$.[157] Recently, semiconducting $Cu_3SnMgInZnS_7$ was proposed and termed as high-entropy sulfide.[158] We note that this material is designed by enthalpy minimization rather than entropy stabilization, and can be seen as a solid solution of Cu_3SnS_4, $CuInS_2$, ZnS, and MgS. As a result, the metal ions show the local ordering of the parent compounds to locally satisfy the octet rule rather than a random distribution on the cation sublattice. On the other hand, there is a dearth of work on semiconducting highentropy chalcogenide based on entropy stabilization, which is the focus of the present study.

Moreover, most high-entropy ceramics developed so far only utilize the configurational entropy of the cation sublattice to stabilize the solid-solution phase while keeping the composition of the anion site unary. However, there is no reason to rule out the anionic stabilization.[159] By also exploiting the configurational entropy of the anion sublattice, strong entropy stabilization can be realized with a smaller number of elements. For example, for an alloy of N cations and M anions with one site for each ion type in the unit cell, the molar entropy at the equi-ionic composition is $R(\ln N + \ln M) = R \ln NM$, or equal to the equimolar mixing of $N \times M$ cations, if only cation mixing is performed. This multicationic and -anionic entropy stabilization has recently been demonstrated in high-entropy Li-ion battery material.[160] Thus, ambi-ionic alloying promotes the formation of entropy-stabilized materials using a smaller number of constituent elements.

Here, we extend the principle of multicationic and -anionic entropy stabilization to 6-component chalcogenide alloys based on the (Ge,Sn,Pb)(S,Se,Te) formula and demonstrate the stabilization of single-phase solid solutions in the rocksalt crystal structure by exploiting the disorder of both the anion and cation sublattices. The synthesized high-entropy chalcogenide alloys (HECs) are thermodynamically stable at the growth temperature and kinetically metastable at room temperature, while at intermediate temperatures they phase segregate with spinodal-like decomposition into SnSe-rich lamellar inclusions within a SnSe-poor rocksalt matrix. The resulting composites are semiconducting, as demonstrated by the sign reversal of the Seebeck coefficient after controllable ambipolar doping by Bi donors and Na acceptors. Our results pave the way for the adoption of entropy-stabilized alloys in a wider array of semiconductor functional applications

6.2 Methodology

6.2.1 First-Principles Calculations

We sampled the composition space of GeSnPbSSeTe HEC in 1/6 composition increments for each element (i.e., $Ge_xSn_yPb_{1-x-y}S_zSe_tTe_{1-z-t}$ with x = 0, 1/6, 2/6, ..., 1, and similarly for y, z, and t) for a total of 775 compositions. We then generated special quasirandom structures (SQSs) for each composition with the Alloy Theoretic Automatic Toolkit (ATAT)[33] by minimizing the difference with the pair-correlation function of the fully random alloy up to a radius of 6 Å. We fixed the size of the SQSs to a 3 × 3 × 2 multiple of the 2-atom rocksalt primitive cell. We subsequently performed high-throughput calculations based on density functional theory (DFT) and the Perdew-Burke-Ernzerhof (PBE) exchange-correlation functional[14] with the Vienna *ab initio* Simulation Package (VASP).[27] The interaction between the core and valence electrons is described with the projector augmented wave method (PAW)[26] using a plane-wave energy cutoff of 500 eV. To evaluate the influence of the filled *d* shell of Sn ($4d^{10}$) and Pb ($5d^{10}$) on the thermodynamic and structural alloy properties, we performed calculations with and without the filled *d* shell in the valence for $Ge_{0.5}Sn_{0.5}Te$ and $Sn_{0.5}Pb_{0.5}Te$ and found that the formation enthalpy differs by less than 5 meV/f.u., while the lattice constant varies by less than 0.5%. Thus, we treated the cation *d* electrons as core electrons in subsequent calculations. We also used a 2 × 2 × 2 Monkhorst-Pack grid[32] to sample the supercell Brillouin zone and allowed the lattice vectors, cell volume, and ion positions to relax until the forces on the ions were less than 0.01 eV Å^{-1}. We investigated the phase stability of each composition by evaluating the energy above the convex hull, E_{hull}, and the configurational entropy ΔS. We constructed the convex hull by calculating the total energy of the binary ingredients using primitive cells in the orthorhombic $Pnma$ space group for GeS, GeSe, SnS, and SnSe, the $R3m$ space group for GeTe, and rocksalt ($Fm\overline{3}m$) for SnTe, PbS, PbSe, and PbTe. The configurational entropy was calculated with the equation for the ideal solution model:

$$\Delta S = -k_B \sum_i x_i \ln x_i \tag{6.1}$$

Finally, we determined the phase-transition temperature between the single-phase solid solution and the phase segregation to its binary ingredients by

$$T_{transition} = \frac{E_{hull}}{\Delta S} \tag{6.2}$$

We constructed the ternary heatmap of the phase-transition temperature as a function of cation and anion composition by training a Gaussian Kernel Ridge Regression machine learning model on the $T_{transition}$ data obtained from the high-throughput calculations. The regularization parameter and the broadening of the Gaussian kernel function were chosen by five-fold cross validation to prevent overfitting. The finalized hyperparameter set gave a mean-absolute-error of 37 K on the training set, and 65 K on the validation set. We investigated the electronic properties of the equimolar HEC composition ($Ge_{1/3}Sn_{1/3}Pb_{1/3}S_{1/3}Se_{1/3}Te_{1/3}$) with DFT calculations based on the PBE-GGA and the hybrid HSE06 functionals.[16] We set the HSE06 mixing parameter to its standard value of 0.25. We employed Γ-centered grids to sample the Brillouin zone of the supercell (4 × 4 × 4 for the GGA and 2 × 2 × 2 for the hybrid calculations), and we determined the band gap as the energy difference between the highest occupied and the lowest unoccupied states of the sampled Brillouin points. Spinorbit coupling was included in both the GGA and the hybrid calculations.

6.2.2 Synthesis and Processing

Polycrystalline ingots of $(GeSnPb)_{1/3}(SSeTe)_{1/3}$ as well as the Bi or Na doped samples used in this study were synthesized using a two-steps solid state reaction process. In the first step, stoichiometric mixtures of the elements (total weight: 10 g) were thoroughly ground under argon atmosphere in a glovebox and sealed in a quartz tube under a residual pressure of 10^{-3} Torr. The sample was heated to 1000 °C over 20 h, dwelled at this temperature for 2 h while rocking the furnace to maximize intermixing of the components in the liquid state, and finally cool to room temperature in 24 h. The resulting ingots were then crushed and mixed under argon atmosphere in a glovebox and sealed in another quartz tube under 10^{-3} Torr. For this second reaction step, the samples were heated at 900 °C, dwelled for 1 h, and then quenched either in liquid nitrogen or in water at room temperature. To investigate the thermodynamics of the metastable HEC alloy $(GeSnPb)_{1/3}(SSeTe)_{1/3}$ obtained by fast cooling in liquid nitrogen, the ingot was broken into several pieces and annealed at various temperatures (200 °C, 300 °C, and 400 °C) for 50 h to induce the decomposition of the homogeneous solid solution phase. To probe the reversibility of the phase transition between the metastable HEC homogeneous solid solution and the thermodynamically stable mixture of phases, a portion of the sample previously annealed at 400 °C for 50 h was further annealed at 550 °C for 60 h and quenched in liquid nitrogen.

6.2.3 Characterization

Samples obtained from the solidstate synthesis and various post synthesis thermal treatments were characterized by X-ray powder diffraction (PXRD) using monochromatic Cu-Kα radiation on a Rigaku Smartlab operating at 40 kV and 40 mA. The thermal stability of the ingot obtained by fast cooling in liquid nitrogen was investigated by differential scanning calorimetry (DSC) using a heating and cooling rate of 5 K per minute on an F401 DSC apparatus from NETZSCH. The reversibility of the phase transition was probed by measuring temperature dependent XRD patterns from 100 to 700 °C using the phase separated HEC sample obtained from slow quenching in water. The sample was sealed in a capillary quartz tube, and the XRD data were collected using monochromatic Mo-Kα radiation on an IPDS-2T (STOE) diffractometer operating at 50 kV and 40 mA. A JEOL JSM-7800FLV scanning electron microscope equipped with Oxford XMaxN 80 mm^2 silicon-drift energydispersive X-ray spectrometer was used to collect backscattered electron (BSE) images and composition mapping on liquid nitrogen quenched samples after annealing at 300 °C for 50 h.

6.2.4 Electronic and Thermal Transport Measurements

To measure the thermoelectric properties, ingots of undoped and doped samples obtained by quenching in liquid nitrogen were crushed and consolidated at 400 °C under 100 MPa using a uniaxial hot press. The electrical conductivity and thermopower were measured simultaneously under a lowpressure helium atmosphere using the four-probe method on a commercial ULVAC-RIKO ZEM-3 system. The thermal conductivity was calculated ($\kappa = \rho C_P D$, where ρ, C_P, and D are density, specific heat capacity, and thermal diffusivity, respectively) from thermal diffusivity and heat capacity data measured by laser flash method on a Linseis LFA-1000 laser flash system.

6.3 Thermodynamic stability of GeSnPbSSeTe high-entropy chalcogenide

We first investigate the thermodynamic landscape of GeSnPbSSeTe alloys in 1/6 composition increments over their entire composition space using high-throughput DFT calculations (Figure 6.1). The competition between the energy above the con-

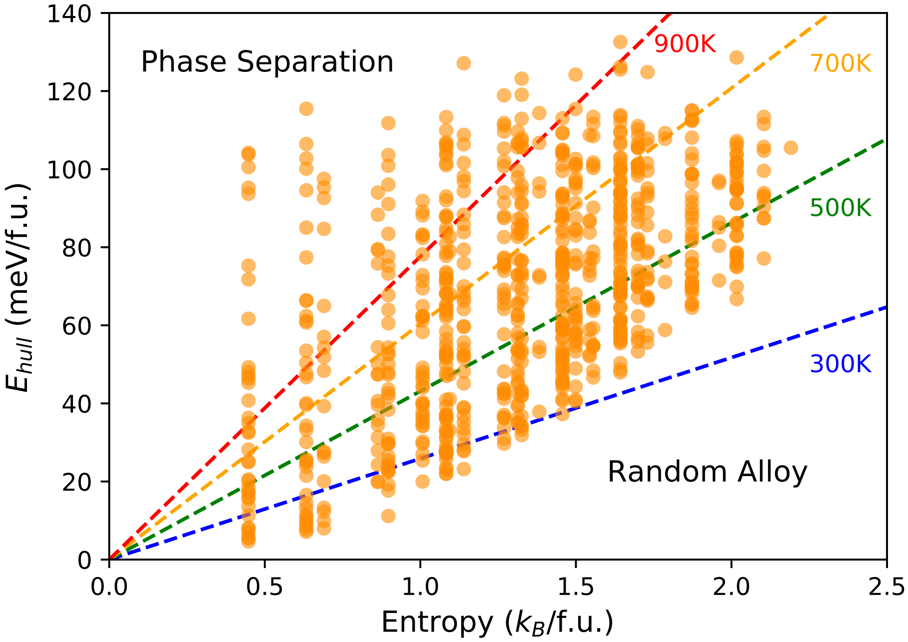

Figure 6.1: Energy per formula unit (f.u.) above the convex hull versus entropy for the 775 investigated HEC compositions. The lines correspond to the phase-transition temperature that stabilizes the high-entropy single-phase solid solutions. Compositions that lie above each line are thermodynamically unstable at that temperature against phase segregation to the binary ingredients.

vex hull, calculated here as the enthalpy of mixing with respect to the most stable combination of binaries, and the configurational entropy determines the thermodynamic stability of single-phase HECs, characterized by the phasetransition temperature. A lower phase-transition temperature causes slower kinetics enabling the formation of the metastable high-entropy phase through faster cooling, and increases the likelihood that the high-entropy metastable solid solution remains stabilized at room temperature. At room temperature (300 K), most of the compositions are not thermodynamically stable, that is, the free-energy reduction by the configurational entropy cannot counterbalance the mixing enthalpy. However, nearly all (99%) HEC compositions (i.e., alloys with configurational entropy S higher than 1.6 k_B per formula unit (f.u.)) are thermodynamically stable with respect to the binary ingredients at the typical chalcogenide growth temperature (T $\approx$ 900 K).[150,161] After equilibra-

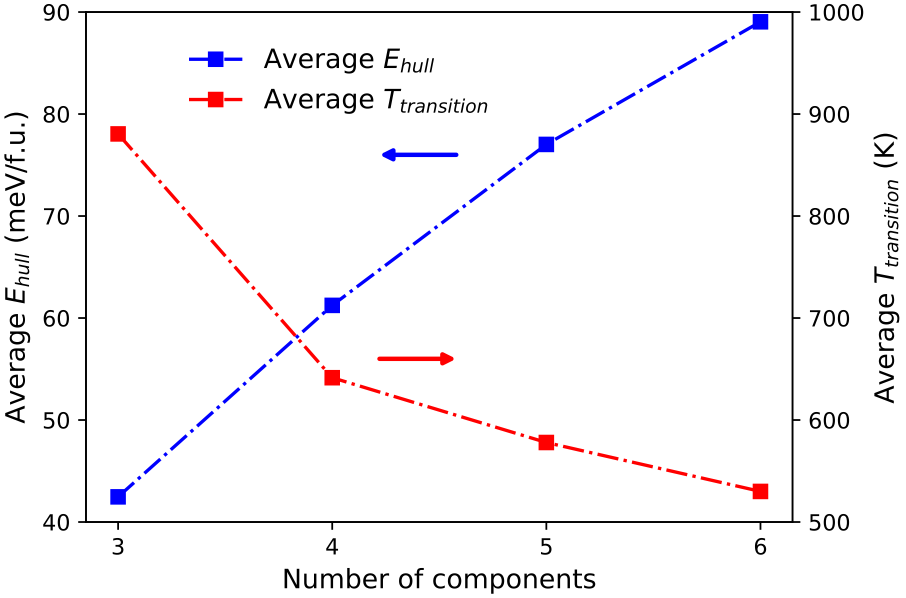

Figure 6.2: Average energy above the convex hull and average transition temperature as a function of the number of alloy components. Incorporating a larger number of principal components increases the configurational entropy and improves the thermodynamic stability, even though the average mixing enthalpy increases.

tion at the growth temperature and the formation of a homogeneous rocksalt solid solution, the single-phase HEC can be kinetically stabilized at room temperature by fast quenching. Thus, single-phase GeSnPbSSeTe HEC alloys can be synthesized over a wide range of compositions and metastabilized in ambient conditions.

We then explore the effects of entropy on the alloy stability. The solubility of each element in conventional alloys is limited by the enthalpic penalty from the unfavorable chemical bonding and the microscopic strain induced by the difference of atomic radii. However, the solubility limit can be overcome when multiple elements are mixed together. This entropy-stabilization effect is illustrated in Figure 6.2: the average phase-transition temperature of the ternary subset of compositions is high (900 K). This is because the random ternary alloys are unfavorable with respect to decomposition into ordered binaries. However, the average phase-transition temperature drops by 300 K for alloys composed of five or more ions, even though the

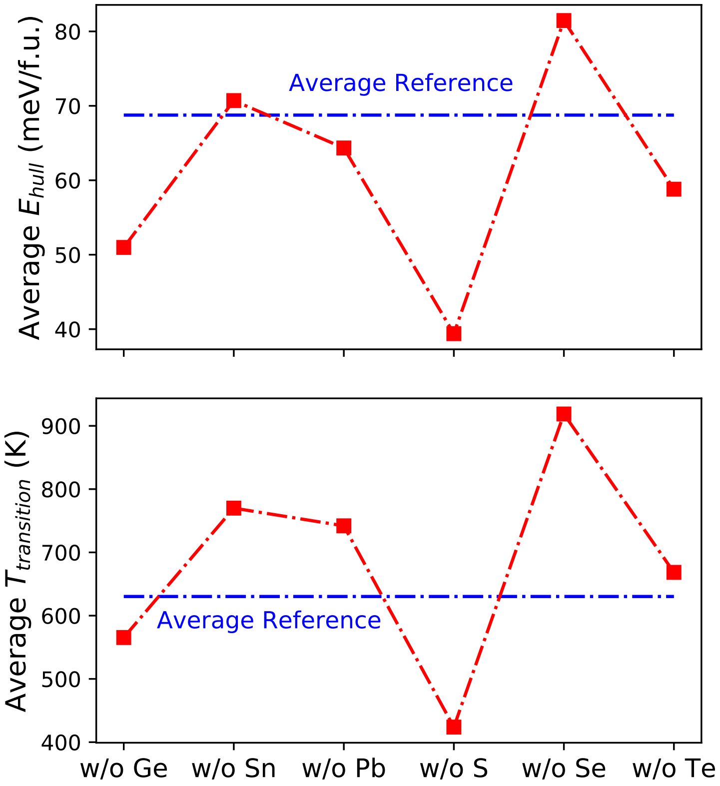

Figure 6.3: Average energy above the convex hull and average transition temperature for alloy compositions that lack one of the component elements. The dashed line represents the average E_{hull} and $T_{transition}$ of the 775 calculated HEC compositions. S and Ge are most detrimental to the thermodynamic stability while Se, Sn, and Pb help improve stability.

enthalpic penalty increases. This improved phase stability is enabled by the large configurational entropy of the two sublattices and would otherwise be impossible with conventional semiconductor alloys, for which the entropy stabilization effect is smaller.

Next, we analyze the contributions by the various elements to the enthalpy of mixing. Even though the average configurational entropy increases monotonically with the inclusion of more elements, the effect of chemical composition on the enthalpy is not intuitive. We thus examine the average enthalpy of mixing and the average transition temperature for alloy compositions that lack one of the components (Figure 6.3), and find that the average energy above the hull is lower than the ensemble av-

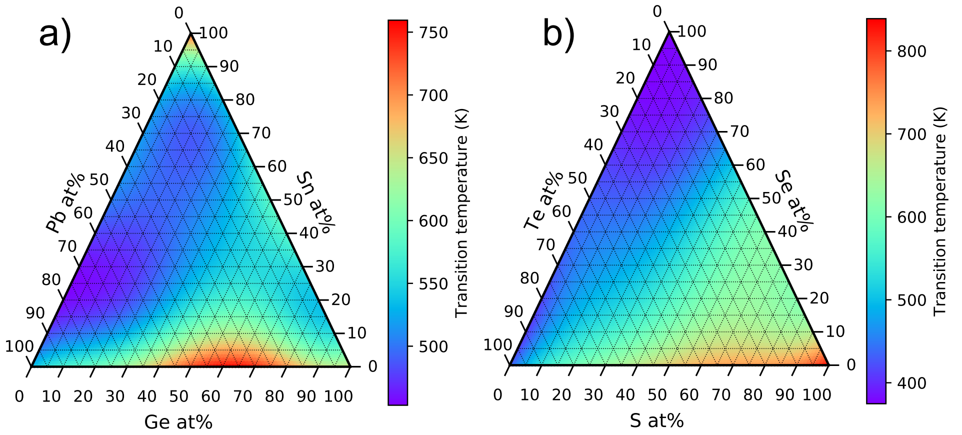

Figure 6.4: Phase-transition temperature as a function of (a) cation and (b) anion compositions for the equimolar (a) anion and (b) cation composition. Mixing Sn and Pb on the cation sites, and Se and Te on the anion sites enable the highest thermodynamic stability.

erage for compositions that exclude Ge, Pb, S, and Te, respectively. A combination of low mixing enthalpy with high configurational entropy is indicative of favorable thermodynamic stability, which is reflected in the phase transition temperature. Our results show that the transition temperature is lower by 200 K for compositions that lack S, while excluding Sn, Pb, and Se increases the transition temperature significantly, for example, by 300 K for Se. The variation of the transition temperature with the cation and anion composition is more comprehensively seen in the ternary map of the transition temperature (Figure 6.4) obtained by fitting the high-throughput data with a machine-learning model. The model illustrates that Ge-poor compositions on the cation site and S-poor compositions on the anion site further stabilize the HECs by lowering the phase-transition temperature. Therefore, we predict that compositions richer in Sn, Pb, and Se, and poorer in S, compared to the equimolar are thermodynamically more stable and easier to synthesize experimentally.

6.4 Phase Purity and Thermal Stability of Equimolar HEC

To experimentally validate our computational predictions on the thermodynamics of HECs, we focus on the equimolar composition ($Ge_{1/3}Sn_{1/3}Pb_{1/3}S_{1/3}Se_{1/3}Te_{1/3}$), which has the highest configurational entropy ($S = k_B \ln 9 = 2.2 k_B \cdot f.u.^{-1}$, or 2.2 $R \cdot mol^{-1}$). With conventional cationic entropy stabilization only, such a high entropy value requires the equimolar mixing of $3 \times 3 = 9$ elements, yet ambi-ionic alloying enables such high mixing entropy with only $3 + 3 = 6$ ion species. We synthesize the equimolar HEC by a two-step reaction of the elements at 1000 °C, and then 900 °C followed by quenching. Consistent with our calculations, which predict that the equimolar composition is thermodynamically metastable at room temperature, we find that the phase purity of the resulting sample depends on the cooling rate (Figure 6.5). For instance, if the HEC sample is quenched fast using liquid nitrogen, the XRD pattern shows a series of sharp and welldefined peaks associated with a single-phase solid solution in the rocksalt structure. However, diffraction peaks corresponding to an SnSe-rich orthorhombic secondary phase appear on the XRD pattern if the sample is quenched slowly in roomtemperature water. Even though the solid-solution phase obtained by fast quenching is metastable at room temperature, it remains robust despite large thermal perturbations and does not phase segregate until extended annealing at temperatures exceeding 300 °C (Figure 6.6). The resulting microstructure (Figure 6.7) consists of fine SnSe-rich lamellae embedded in a SnSe-poor rocksalt matrix, which resembles a spinodal decomposition-like transformation of the metastable solid solution upon annealing at temperatures above 300 °C (Figure 6.6). The phase-segregated sample reverses back to the solidsolution phase after annealing at 550 °C followed by fast quenching, indicating the reversibility of the phase transition. One question that remains open for future investigation is whether there is any microscopic local ordering of the cation and anion sublattices in the metastable solid solution phase. In high-entropy oxides, extended X-ray absorption fine structure

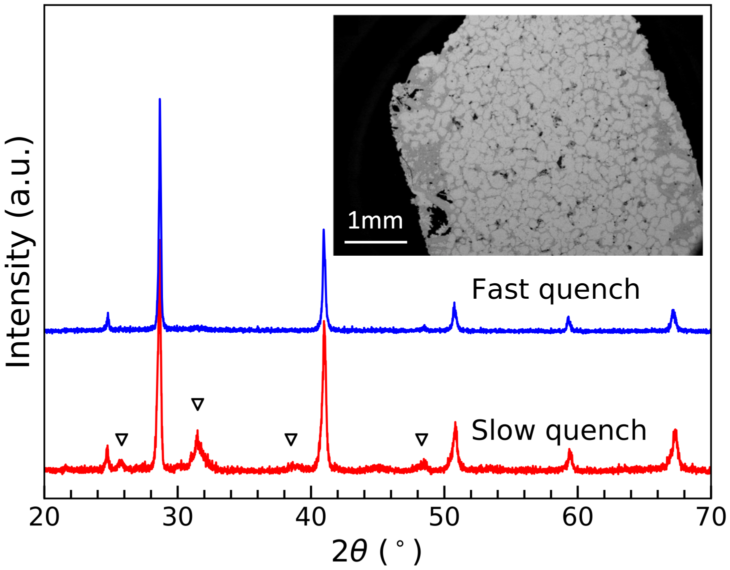

Figure 6.5: X-ray diffraction pattern (XRD) with Cu-Kα radiation of equimolar GeSnPbSSeTe after quenching from the molten phase in liquid nitrogen (fast) or room-temperature water (slow), showing well-defined rocksalt peaks. Slow quenching also shows secondary orthorhombic peaks (triangles). Inset: backscattered electron image of the fast-quenched sample after annealing, showing a majority rocksalt phase (brighter section).

(EXAFS) experiments found that there is no significant cation local ordering.[133,162] A similar analysis would be helpful to shed light on the issue of short-range order in high-entropy chalcogenides.

We further examine the thermodynamics of the metastable solid solution by differential scanning calorimetry (DSC). An exothermic transition with an onset at around 300 °C and a peak at 400 °C was observed on the first DSC heating curve (Figure 8), attributed to the phase segregation of the solid solution. Further heating above 430 °C transforms the sample back to the single-phase solid solution, followed by congruent melting around 620 °C. Upon cooling, the sample recrystallizes into the single-phase solid solution at around 610 °C and phase segregates at 420 °C. The reversible phase transition at around 430 °C is therefore driven by the configurational entropy. The second DSC heating curve only shows the endothermic peak associated with the transformation of the phase-segregated composites to the rocksalt solid

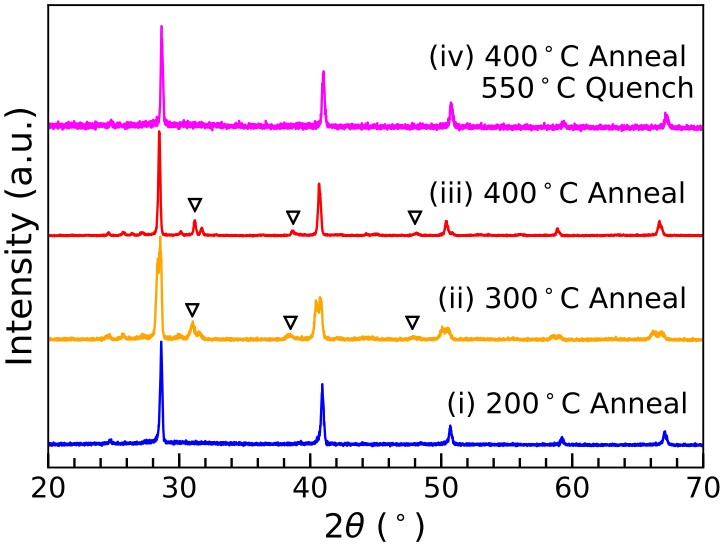

Figure 6.6: XRD pattern of the fast-quenched equimolar HEC after the two-step synthesis annealed at (i) 200 °C, (ii) 300 °C, and (iii) 400 °C, plus a sample annealed at (iv) 550 °C and quenched in liquid nitrogen. Triangles indicate diffraction peaks associated with the SnSe-rich phase formed after phase segregation. The rocksalt solid solution remains metastable after annealing at 200 °C, but phase separates between 200 and 300 °C. Between 430 and 620 °C the phase-separated sample reversibly transforms back to the rocksalt phase.

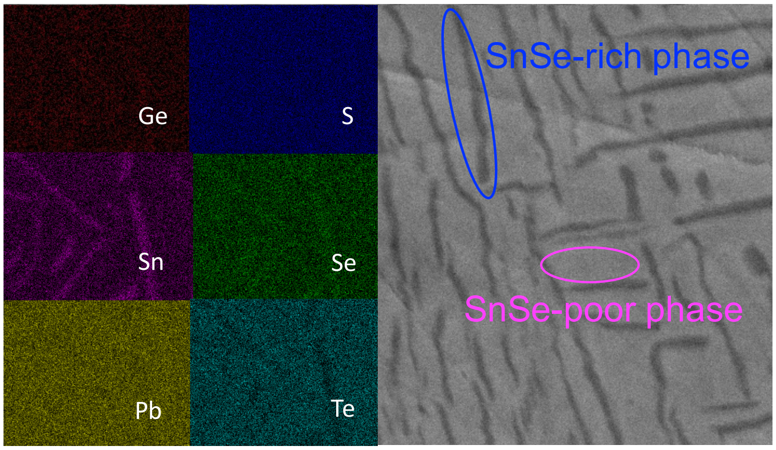

Figure 6.7: Backscattered SEM image of the fast-quenched equimolar HEC after extended annealing at 300 °C showing the fine lamellar microstructure reminiscent of spinodal decomposition. The dark-gray nanoribbons are the orthorhombic SnSe-rich phase, while the lightgray matrix is the rocksalt SnSe-poor phase.

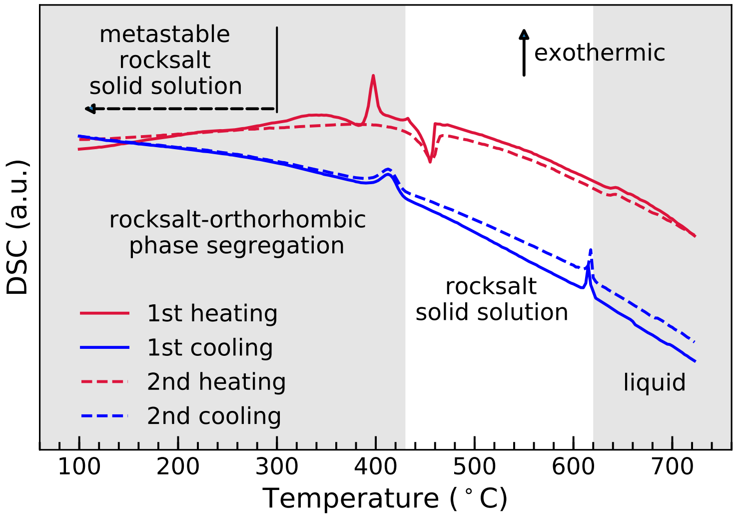

Figure 6.8: Differential scanning calorimetry (DSC) analysis on fast quenched equimolar HEC. The endothermic peak at 430 °C during heating and the exothermic peak at 420 °C during cooling show the reversible phase transition driven by the configurational entropy between the single-phase rocksalt solid solution and the phase-segregated regime.

solution, with no sign of the exothermic peak observed at 400 °C during the first heating. This implies that the slow cooling rate (5 K min^{-1}) during DSC causes complete segregation of the highentropy solid solution and further confirms that the solid solution can only be metastabilized at room temperature via fast quenching, consistent with the X-ray diffraction results (Figure 6.6).

To confirm the stability regions of the various phases observed in DSC and further demonstrate the reversibility of the phase transition, we recorded temperature-dependent XRD data (Figure 6.9). The secondary phase persists even at 500 °C, while the solid solution appears at 600 °C, and the sample melts at 700 °C. Qualitatively identical XRD patterns are obtained during cooling. We attribute the slightly different phase-transition temperature in the DSC measurements (430 °C) to the closer contact between the sample holder and the temperature probe during DSC, which provides a more accurate temperature measurement.

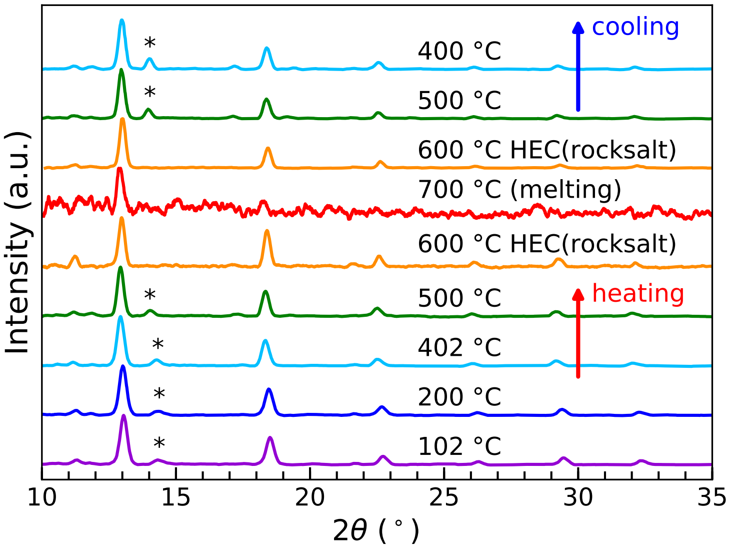

Figure 6.9: Temperature-dependent XRD with Mo-Kα radiation of the equimolar GeSnPbSSeTe during heating and cooling. The asterisks indicate the diffraction peaks associated with the SnSe-rich secondary phase. The sample transformed from phase-segregated composites to single-phase rocksalt solid solution upon heating above 500 °C

6.5 Dopability and Transport Properties of Equimolar HEC

In addition to the thermodynamic, structural, and chemical properties, which have traditionally been the focus of previous reports on high-entropy materials, we have extended our investigation to the electronic and thermal transport properties of the synthesized HECs. Here, we demonstrate the dopability of the equimolar alloy and characterize its semiconducting properties both with DFT calculations and with experimental transport measurements. The calculated band gap of $Ge_{1/3}Sn_{1/3}Pb_{1/3}S_{1/3}Se_{1/3}Te_{1/3}$ is 0.86 eV, which is a typical value of semiconductors and of similar magnitude to its binary ingredients such as SnSe[161] (0.86 eV) and SnS[163] (1.07 eV). A key characteristic, though, that distinguishes semiconductors from insulators is the possibility of controllable doping. Our investigation reveals that the equimolar HEC shows promising ambipolar dopability. Thermopower measurements (Figure 6.10a) reveal p-type transport for the nominally undoped equimolar

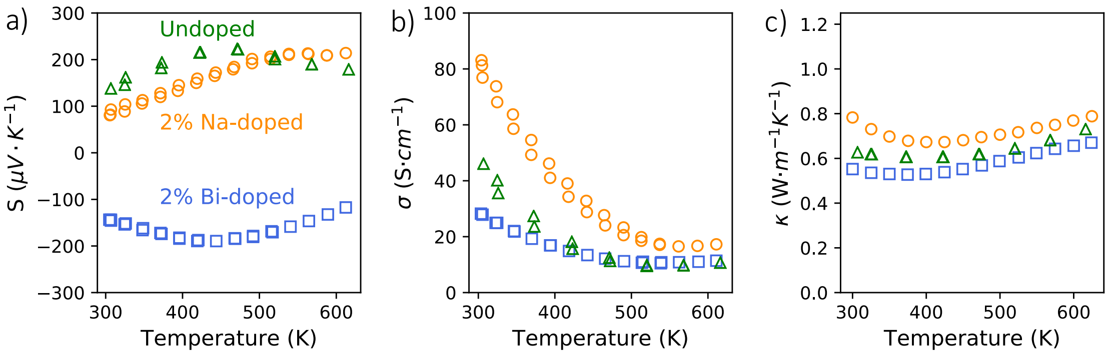

Figure 6.10: (a-c) Transport properties of undoped and doped equimolar HEC. Temperature-dependent (a) Seebeck coefficient, (b) electrical conductivity, and (c) thermal conductivity. The sign of the Seebeck coefficient indicates that GeSnPbSSeTe HEC is an ambipolarly dopable semiconductor (n-type with Bi donors and p-type with Na acceptors). The thermal conductivity is exceptionally low and nearly independent of temperature. The electrical conductivity decreases with temperature, indicative of heavily doped semiconducting behavior.

HEC sample, which we tentatively attribute to the formation of cation vacancies. We also found that controllable doping can be achieved by substituting divalent cations with monovalent (p-type) or trivalent (n-type) elements. For example, by substituting host cations with Na, the thermopower remains positive and exhibits a peak at higher temperature (Figure 6.10a) while the conductivity increases (Figure 6.10b), which indicates the addition of free holes to the valence band. On the other hand, when Bi substitutes divalent host cations, the sign of the Seebeck coefficient becomes negative indicating n-type transport.

This ambipolar dopability of the GeSnPbSSeTe HEC with acceptors (Na) and donors (Bi) opens up possibilities for the application of HEC in electronic and optoelectronic devices. Thermal transport measurement reveals ultralow thermal conductivity for the equimolar HEC, which we ascribe to phonon scattering by strong mass fluctuations owing to the significant atomic disorder of both sublattices (Figure 6.10c). Such low thermal conductivity paves the way for applications of HECs as thermal barrier coatings in, for example, chalcogenide-based thermoelectric devices. The principle of entropy stabilization introduced here for the semiconducting GeSnPbSSeTe HECs can be extended more broadly to numerous functional chalcogenide applications such as spintronic,[164] topological insulating (e.g., rocksalt SnSe),[165] or superconducting (e.g., FeSe) materials.[166] In addition, engineering the resulting microstructure of phase-segregated metastable compounds may enable the design of functional meta-materials composed of phases with complementary functionalities. We therefore expect that the discovery of semiconducting highentropy chalcogenides will catalyze their wider exploration and adoption in functional applications.

6.6 Conclusions

In conclusion, we demonstrated the synthesis of high-entropy semiconducting chalcogenide alloys, stabilized by the large configurational entropy of both cation and anion sublattices. Although alloy disorder in semiconductors is traditionally seen as an unavoidable compromise to control the material properties, our work demonstrates that the configurational entropy can be exploited to stabilize semiconductor compositions that are otherwise impossible due to phase segregation. By demonstrating the possibility of ambipolar doping, our results pave the way for the realization of functional applications of entropy-stabilized semiconducting materials in electronic, optoelectronic, photovoltaic, and thermoelectric devices.

CHAPTER VII

Summary and Future Work

7.1 Summary

In conclusion, we employed first-principles calculations based on density functional theory to study the thermodynamic and electronic properties of semiconductors. In particular, we investigated the impact of point defects in a wide range of semiconducting materials, including AlN, AlGaN alloy, LaN, and Cu_2O. In addition, thermodynamic stability of the disordered II-IV-N_2 and high entropy chalcogenide alloys was also studied in depth. The detailed findings of each chapter are as follows.

Chapter II aimes at addressing the long-standing challenge of achieving heavy p-doping for ultrawide bandgap nitride semiconductors, with a focus on the AlN and AlGaN alloy. From the basic defect thermodynamics, we proposed two strategies to enhance the p-doping efficiency, which are chemical potential engineering and Fermi level engineering. A large free hole concentration can be realized by growing dislocation-free AlN nanowires under N-rich condition. This grow condition causes a high chemical potential for N and a low chemical potential for Al, which significantly decreases the formation energy of Mg dopants and increases the formation energy of compensating N vacancies. The same principles can also be achieved by pinning the Fermi level at the grow surface away from the valence band maximum of AlGaN through metal-semiconductor junction assisted epitaxy. These two strategies can be applied more broadly in other ultrawide bandgap semiconductors.

Chapter III investigates the band structure, band alignment, intrinsic defects and common impurities of LaN. Contrast to previous claims that LaN is a semimetal, our calculations show that LaN is a direct bandgap semiconductor with a direct gap of 0.62 eV at the X point of the Brillouin zone. Further calculations on the formation energy of intrinsic defects and common impurities reveal that N vacancy and the N-substitutional O impurity have low formation energy and behave as shallow donors. These defects explains the origin of the electrical conductivity of LaN. Our calculations clarify the semiconducting nature and the source of conductivity for LaN, which lays the foundation for LaN to be used for a broad range of functional applications.

Chapter IV presents a comprehensive study on the intrinsic defects, common impurities, and various candidate p-type dopants for Cu_2O. Among all intrinsic defects, the Cu simple vacancy and the Cu split vacancy are dominant due to their low formation energy. Due to the large ionization energy of Cu vacancy acceptor, the equilibrium free hole concentration of Cu_2O is relatively low. H impurities can further compensate Cu vacancies by forming neutralized defect complex. Our survey over a series of candidate p-dopants shows that N, S, and Mg are promising elements to be use for effective p-type doping in Cu_2O. This work sheds light on the thermodynamic of point defects in Cu_2O and proposes possible dopants for effective p-doping.

Chapter V focuses on the issue of cation disorder in heterovalent ternary nitride (II-IV-N_2). We used $ZnSnN_2$ as a model system to study the impact of cation disorder on the thermodynamic stability and bandgap, where the octet rule plays an important role. We find that 4-motifs are extremely unfavorable from a thermodynamic point of view, characterized by a large increase in formation energy. For partially disordered $ZnSnN_2$, the fraction of octet rule conserving motifs is maximized to lower the overall energy. The bandgap of $ZnSnN_2$ and other heterovalent ternary semiconductors is linearly proportional to the square of the long-range order parameter. We also discover that the size mismatch between group-II and group-IV cations is a good indicator to the tendency towards disordering. Large size mismatch results in a large inplane distortion and a more ordered material. Thus, choosing cation pairs with a desired size mismatch can enable rational control on the degree of disordering in II-IV-N_2. Our calculations emphasize the effect of cation disorder in II-IV-N_2 system and propose ways to rational control the disordering.

Chapter VI presents a high-throughput DFT calculations on the GeSnPbSSeTe high entropy chalcogenide alloys. The entire composition space was sampled evenly using DFT and the convex hull was constructed. Near room temperature, most of the compositions are not thermodynamically stable. However, over 90% of the composition are stable at a typical growth temperature for chalcogenide synthesis. Further analysis shows that Sn and Se help improve the thermodynamic stability whereas S is detrimental to the stability. We also synthesized the equimolar GeSnPbSSeTe and showed that it can crystalize in a rocksalt structure upon fast quenching in liquid nitrogen. DSC and temperature dependent XRD shows the reversible transition between the high entropy rocksalt phase and the multiple phase regime. Bandgap calculations and transport measurement show that the equimolar GeSnPbSSeTe is an ambipolarly dopable semiconductor. Our work presents a seminal breakthrough by proposing a novel class of semiconducting high entropy materials and catalyzing the utilization of high entropy chalcogenide alloys in a broad range of semiconductor functional applications.

7.2 Future work

This dissertation presents in-depth research on the thermodynamics of point defects as well as the thermodynamics of semiconductor alloys in several important material systems. The scope and the impact of this work can potentially be further expanded in the following avenues.

Semiconducting materials that can be p-type doped are of great importance for the next generation devices, such as transparent electronics. The sparsity of suitable p-type semiconductors in comparison to their n-type counterpart is a big obstacle, and a breakthrough in materials discovery is needed. The dopability of a semiconductor is determined by the interplay between the intrinsic defects and extrinsic dopants, and the defect calculation presented in this work is a powerful tool to predict the dopability of semiconductors from theory. Therefore, a computational study over a wide range of semiconductors using defect calculations in a high-throughput manner can efficiently screen thousands of potential candidates for p-doping and lead to the discovery of novel p-type semiconductors with great technological importance.

Also, the effect of cation disorder on the properties of II-IV-N_2 was investigated using a simple model based on nearest-neighbor motifs. It is possible that the interactions beyond first-nearest neighbors in the cation sublattices also play an important role. In the future, more advanced thermodynamic model such as the cluster expansion approach can be applied to quantify the thermodynamic contribution of each possible clusters, which can give valuable insights on the effect of medium-range disorder on the thermodynamic and electronic properties of II-IV-N_2 systems.

In addition, the high throughput DFT studies presented in Chapter VI can be extended to predict the thermodynamic stability of other high entropy material systems, such as high entropy oxides. High entropy oxides have attracted tremendous interests for their superior stability and intriguing properties. Many high entropy oxide research focus on the $(MgCoNiCuZn)_{0.2}O$ and its close variant, but there are endless possibilities of other high entropy oxides if different cation species and composition are chosen. And a straightforward way to investigate their stability is to calculate the energy above the hull and the configurational entropy. Their interplay will give a holistic picture of their stability over the entire composition space, which can shed light on the possibility for experimental synthesis.

Last but not least, the configurational entropy plays an important role in stabilizing high entropy chalcogenide alloys. Our calculations employed the ideal solution model for the entropy, which assumes complete randomness of the cation and anion sublattices. However, there can exist chemical short range ordering among cations and anions. Some cations may prefer bonding to a particular anion instead of treating all anions in the same way. This short range ordering can decrease the entropy and influence the thermodynamic stability. Therefore, Monte Carlo simulations or molecular dynamic simulations can be employed to study the temperature evolution of atomic arrangement of high entropy chalcogenide alloys. This will provide valuable insights on the short range ordering and its impact on the overall thermodynamic stability.

APPENDICES

APPENDIX A

Supplemental Materials for LaN Calculations

A.1 Convergence for Defect Calculations in LaN

	64-atom supercell	128-atom supercell	Difference
$E^f(O_N, 0)$	-0.158 eV	-0.186 eV	0.028 eV
$E^f(O_N, +1)$	-0.857 eV	-0.890 eV	0.033 eV
$\varepsilon(+1/0)$	0.698 eV	0.703 eV	0.005 eV

Table A.1: Convergence on defect formation energy $E^f(X, q)$ and charge-transition level $\varepsilon(+1/0)$

A.2 PBE Band Structure of LaN

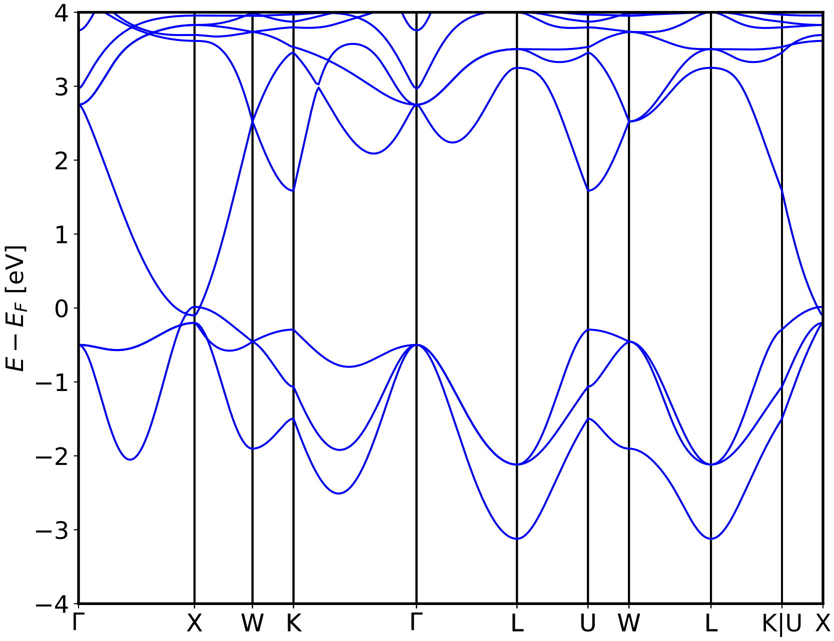

Figure A.1: The electronic band structure of LaN calculated with the PBE functional. The valence and conduction bands overlap by 115 meV at the X point, indicating that semilocal functionals predict LaN to be a semimetal, in agreement with early theoretical studies.

A.3 Orbital Projected HSE Band Structure of LaN

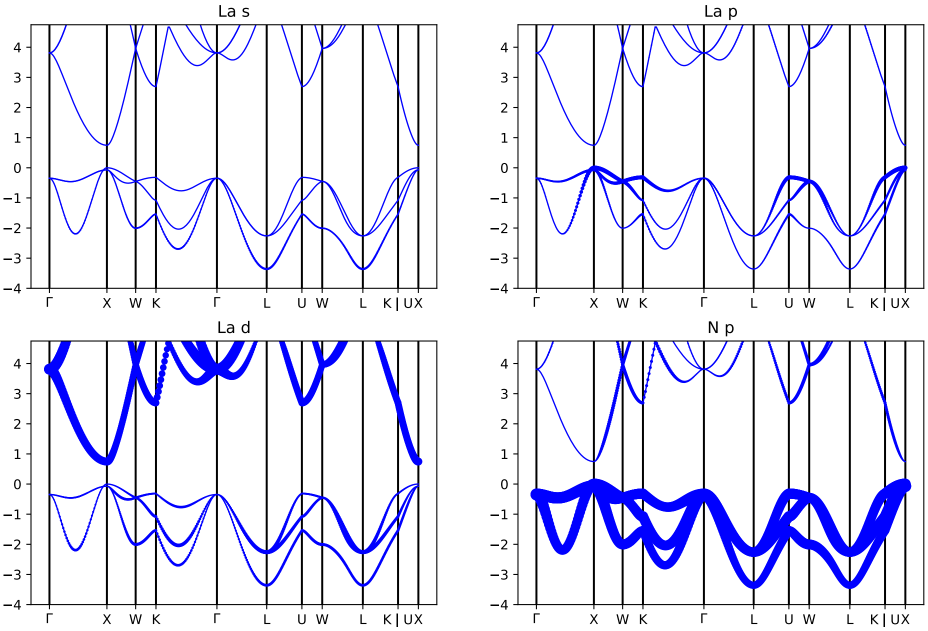

Figure A.2: Orbital projected HSE band structure of LaN. The thickness of the band curve corresponds to the strength of the orbital contribution. The valence band is mainly derived from N 2p orbitals and the conduction band is mainly from La 5d orbitals. The valence band near X and W also has sizable La p characteristics, which gives rise to spin-orbit coupling that breaks the valence-band degeneracy.

APPENDIX B

Supplemental Materials for Cu_2O Calculations

B.1 Convergence for Defect Calculations in Cu_2O

Supercell size	$E^f(V_{Cu}, 0)$ (eV)	$E^f(V_{Cu}, -1)$ (eV)	(0/-1) $\varepsilon(0/-1)$ (eV)
2×2×2	1.44	1.80	0.36
3×3×3	1.17	1.51	0.34

Table B.1: Convergence on defect formation energy and charge-transition level for V_{Cu}

B.2 Orbital Character Projection at Γ

	O s state (eV)	O p state	Cu s state	Cu p state	Cu d state
VBM	0%	14.5%	11.2%	0%	74.3%
CBM	15.2%	0%	13.2%	0%	71.6%
2^{nd} CB	0%	0%	0%	100%	0%

Table B.2: Orbital character projection onto the eigenvalues at Γ for the VBM, CBM, and the second conduction band (2^{nd} CB)

B.3 Orbital-Projected Density of States

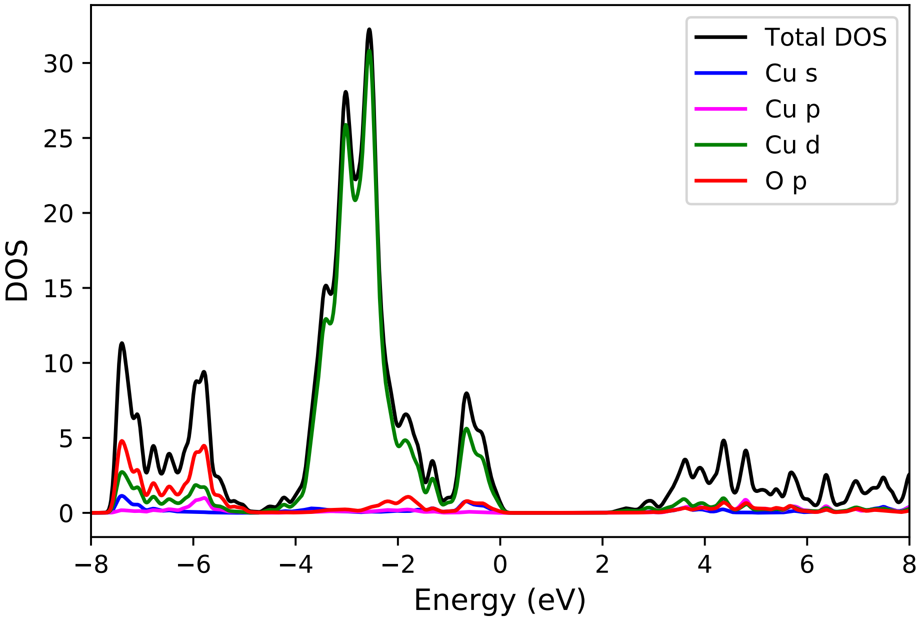

Figure B.1: Orbital-projected density of states for Cu_2O calculated using the HSE06 hybrid functional. The valence band maximum (VBM) and the conduction band minimum (CBM) are mainly derived from Cu $3d$ orbitals.

B.4 Imaginary Part of the Dielectric Function

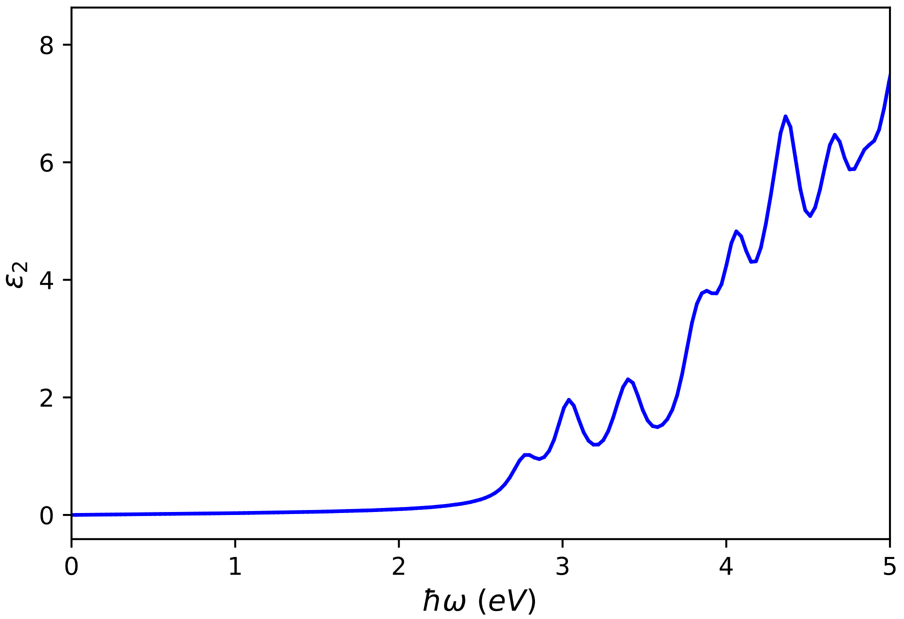

Figure B.2: Imaginary part of the dielectric function for Cu2O as a function of photon energy calculated using the independent particle approximation and the HSE06 hybrid functional. The first absorption peak appears around 2.8 eV, which corresponds to the first optically allowed transition at Γ from the VBM to the 2^{nd} CB.

B.5 Tauc Analysis of PVD Cu_2O Thin Film

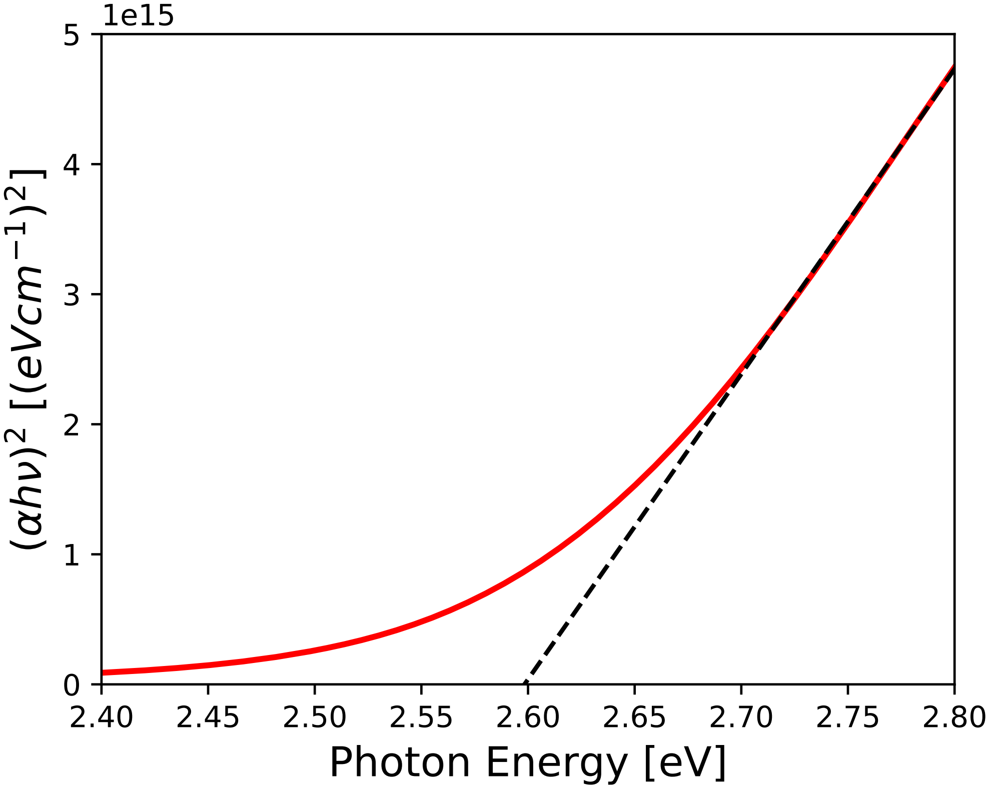

Figure B.3: Tauc analysis for PVD Cu_2O film. Cu_2O has a direct optical band gap of 2.6 eV.

B.6 Formation Energy of N dopants with N Chemical Potential in Equilibrium with N_2 Gas

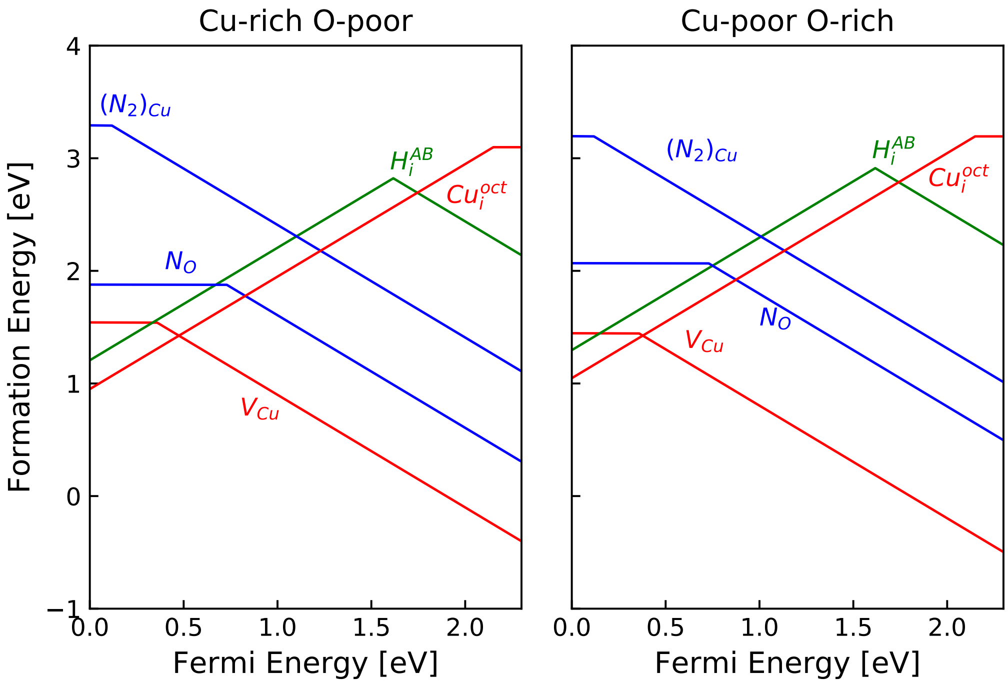

Figure B.4: Formation energy of N dopants in Cu_2O as a function of Fermi energy referenced to the valence band maximum. The N chemical potential is set to be in equilibrium with N_2 gas. The strong triple bond between N in N_2 molecule hinders effective p-doping by N.

BIBLIOGRAPHY

BIBLIOGRAPHY

[1] Y. Kumagai, N. Tsunoda, and F. Oba, "Point Defects and p-Type Doping in ScN from First Principles," *Physical Review Applied*, vol. 9, no. 3, p. 34019, mar 2018. [Online]. Available: https://link.aps.org/doi/10.1103/PhysRevApplied.9.034019

[2] P. G. Moses, M. Miao, Q. Yan, and C. G. Van de Walle, "Hybrid functional investigations of band gaps and band alignments for AlN, GaN, InN, and InGaN," *The Journal of Chemical Physics*, vol. 134, no. 8, p. 84703, feb 2011. [Online]. Available: https://doi.org/10.1063/1.3548872

[3] R. P. Lesunova, L. S. Karenina, S. F. Palguev, and E. I. Burmakin, "The investigation of electrical conductivity of lanthanum, calcium and aluminium nitrides," *Solid State Ionics*, vol. 36, no. 3, pp. 275–278, 1989. [Online]. Available: http://www.sciencedirect.com/science/article/pii/0167273889901902

[4] B. J. Baliga, "Semiconductors for high-voltage, vertical channel field-effect transistors," *Journal of Applied Physics*, vol. 53, no. 3, pp. 1759–1764, mar 1982. [Online]. Available: https://doi.org/10.1063/1.331646

[5] B. Baliga, "Power semiconductor device figure of merit for high-frequency applications," *IEEE Electron Device Letters*, vol. 10, no. 10, pp. 455–457, 1989.

[6] A. J. Green, J. Speck, G. Xing, P. Moens, F. Allerstam, K. Gumaelius, T. Neyer, A. Arias-Purdue, V. Mehrotra, A. Kuramata, K. Sasaki, S. Watanabe, K. Koshi, J. Blevins, O. Bierwagen, S. Krishnamoorthy, K. Leedy, A. R. Arehart, A. T. Neal, S. Mou, S. A. Ringel, A. Kumar, A. Sharma, K. Ghosh, U. Singisetti, W. Li, K. Chabak, K. Liddy, A. Islam, S. Rajan, S. Graham, S. Choi, Z. Cheng, and M. Higashiwaki, "β-Gallium oxide power electronics," *APL Materials*, vol. 10, no. 2, p. 29201, feb 2022. [Online]. Available: https://doi.org/10.1063/5.0060327

[7] S. Chae, K. Mengle, K. Bushick, J. Lee, N. Sanders, Z. Deng, Z. Mi, P. F. P. Poudeu, H. Paik, J. T. Heron, and E. Kioupakis, "Toward the predictive discovery of ambipolarly dopable ultra-wide-band-gap semiconductors: The case of rutile GeO_2," *Applied Physics Letters*, vol. 118, no. 26, p. 260501, jun 2021. [Online]. Available: https://doi.org/10.1063/5.0056674

[8] W. Callister and D. Rethwisch, *Materials Science and Engineering: An Introduction, 8th Edition.* Wiley, 2009. [Online]. Available: https://books.google.com/books?id=OaIbAAAAQBAJ

[9] A. R. Denton and N. W. Ashcroft, "Vegard's law," *Phys. Rev. A*, vol. 43, pp. 3161–3164, Mar 1991. [Online]. Available: https://link.aps.org/doi/10.1103/PhysRevA.43.3161

[10] M. Auf der Maur, A. Pecchia, G. Penazzi, W. Rodrigues, and A. Di Carlo, "Efficiency drop in green ingan/gan light emitting diodes: The role of random alloy fluctuations," *Phys. Rev. Lett.*, vol. 116, p. 027401, Jan 2016. [Online]. Available: https://link.aps.org/doi/10.1103/PhysRevLett.116.027401

[11] W. He, D. Wang, H. Wu, Y. Xiao, Y. Zhang, D. He, Y. Feng, Y.-J. Hao, J.-F. Dong, R. Chetty, L. Hao, D. Chen, J. Qin, Q. Yang, X. Li, J.-M. Song, Y. Zhu, W. Xu, C. Niu, X. Li, G. Wang, C. Liu, M. Ohta, S. J. Pennycook, J. He, J.-F. Li, and L.-D. Zhao, "High thermoelectric performance in low-cost $SnS_{0.91}Se_{0.09}$ crystals," *Science*, vol. 365, no. 6460, pp. 1418 LP – 1424, sep 2019. [Online]. Available: http://science.sciencemag.org/content/365/6460/1418.abstract

[12] S. Mertin, B. Heinz, O. Rattunde, G. Christmann, M.-A. Dubois, S. Nicolay, and P. Muralt, "Piezoelectric and structural properties of c-axis textured aluminium scandium nitride thin films up to high scandium content," *Surface and Coatings Technology*, vol. 343, pp. 2–6, 2018. [Online]. Available: http://www.sciencedirect.com/science/article/pii/S0257897218300549

[13] D. Sholl and J. Steckel, "What is Density Functional Theory?" pp. 1–33, mar 2009. [Online]. Available: https://doi.org/10.1002/9780470447710.ch1

[14] J. P. Perdew, K. Burke, and M. Ernzerhof, "Generalized gradient approximation made simple." *Physical Review Letters*, vol. 77, pp. 3865–3868, 1996.

[15] J. P. Perdew, M. Ernzerhof, and K. Burke, "Rationale for mixing exact exchange with density functional approximations," *The Journal of Chemical Physics*, vol. 105, no. 22, pp. 9982–9985, dec 1996. [Online]. Available: https://doi.org/10.1063/1.472933

[16] J. Heyd, G. E. Scuseria, and M. Ernzerhof, "Hybrid functionals based on a screened Coulomb potential," *Journal of Chemical Physics*, vol. 118, no. 18, pp. 8207–8215, 2003.

[17] C. Freysoldt, B. Grabowski, T. Hickel, J. Neugebauer, G. Kresse, A. Janotti, and C. G. Van de Walle, "First-principles calculations for point defects in solids," *Reviews of Modern Physics*, vol. 86, no. 1, pp. 253–305, mar 2014. [Online]. Available: https://link.aps.org/doi/10.1103/RevModPhys.86.253

[18] C. Freysoldt, J. Neugebauer, and C. G. Van de Walle, "Electrostatic interactions between charged defects in supercells," *physica status solidi*

(b), vol. 248, no. 5, pp. 1067–1076, may 2011. [Online]. Available: https://doi.org/10.1002/pssb.201046289

[19] J. Chen, S. Loeb, and J.-H. Kim, "LED revolution: fundamentals and prospects for UV disinfection applications," *Environmental Science: Water Research Technology*, vol. 3, no. 2, pp. 188–202, 2017. [Online]. Available: http://dx.doi.org/10.1039/C6EW00241B

[20] J. L. Lyons, A. Janotti, and C. G. Van de Walle, "Shallow versus deep nature of mg acceptors in nitride semiconductors," *Phys. Rev. Lett.*, vol. 108, p. 156403, Apr 2012. [Online]. Available: https://link.aps.org/doi/10.1103/PhysRevLett.108.156403

[21] Y. Chen, H. Wu, E. Han, G. Yue, Z. Chen, Z. Wu, G. Wang, and H. Jiang, "High hole concentration in p-type AlGaN by indium-surfactant-assisted Mg-delta doping," *Applied Physics Letters*, vol. 106, no. 16, p. 162102, apr 2015. [Online]. Available: https://doi.org/10.1063/1.4919005

[22] S. John, P. Vladimir, L. Chuanxin, X. Huili, and J. Debdeep, "Polarization-Induced Hole Doping in Wide–Band-Gap Uniaxial Semiconductor Heterostructures," *Science*, vol. 327, no. 5961, pp. 60–64, jan 2010. [Online]. Available: https://doi.org/10.1126/science.1183226

[23] M. Martens, C. Kuhn, E. Ziffer, T. Simoneit, V. Kueller, A. Knauer, J. Rass, T. Wernicke, S. Einfeldt, M. Weyers, and M. Kneissl, "Low absorption loss p-AlGaN superlattice cladding layer for current-injection deep ultraviolet laser diodes," *Applied Physics Letters*, vol. 108, no. 15, p. 151108, apr 2016. [Online]. Available: https://doi.org/10.1063/1.4947102

[24] Y. Zhang, S. Krishnamoorthy, F. Akyol, A. A. Allerman, M. W. Moseley, A. M. Armstrong, and S. Rajan, "Design of p-type cladding layers for tunnel-injected UV-A light emitting diodes," *Applied Physics Letters*, vol. 109, no. 19, p. 191105, nov 2016. [Online]. Available: https://doi.org/10.1063/1.4967698

[25] Y. H. Liang and E. Towe, "Heavy Mg-doping of (Al,Ga)N films for potential applications in deep ultraviolet light-emitting structures," *Journal of Applied Physics*, vol. 123, no. 9, p. 95303, mar 2018. [Online]. Available: https://doi.org/10.1063/1.5009937

[26] P. E. Blochl, "Projector augmented-wave method," *Physical Review B*, vol. 50, pp. 17 953–17 979, 1994.

[27] G. Kresse and J. Furthmüller, "Efficient iterative schemes for ab initio total-energy calculations using a plane-wave basis set," *Physical Review B*, vol. 54, no. 16, pp. 11 169–11 186, 1996.

[28] R. Dingle, D. D. Sell, S. E. Stokowski, and M. Ilegems, "Absorption, reflectance, and luminescence of gan epitaxial layers," *Phys. Rev. B*, vol. 4, pp.

1211–1218, Aug 1971. [Online]. Available: https://link.aps.org/doi/10.1103/PhysRevB.4.1211

[29] W. M. Yim, E. J. Stofko, P. J. Zanzucchi, J. I. Pankove, M. Ettenberg, and S. L. Gilbert, "Epitaxially grown AlN and its optical band gap," *Journal of Applied Physics*, vol. 44, no. 1, pp. 292–296, jan 1973. [Online]. Available: https://doi.org/10.1063/1.1661876

[30] F. Yun, M. A. Reshchikov, L. He, T. King, H. Morkoç, S. W. Novak, and L. Wei, "Energy band bowing parameter in AlxGa1xN alloys," *Journal of Applied Physics*, vol. 92, no. 8, pp. 4837–4839, oct 2002. [Online]. Available: https://doi.org/10.1063/1.1508420

[31] C. G. Van de Walle, S. Limpijumnong, and J. Neugebauer, "First-principles studies of beryllium doping of gan," *Phys. Rev. B*, vol. 63, p. 245205, Jun 2001. [Online]. Available: https://link.aps.org/doi/10.1103/PhysRevB.63.245205

[32] H. J. Monkhorst and J. D. Pack, "Special points for Brillonin-zone integrations," *Physical Review B*, vol. 13, pp. 5188–5192, 1976.

[33] A. van de Walle, P. Tiwary, M. De Jong, D. L. Olmsted, M. Asta, A. Dick, D. Shin, Y. Wang, L. Q. Chen, and Z. K. Liu, "Efficient stochastic generation of special quasirandom structures," *Calphad*, vol. 42, pp. 13–18, 2013.

[34] Y. Wu, D. A. Laleyan, Z. Deng, C. Ahn, A. F. Aiello, A. Pandey, X. Liu, P. Wang, K. Sun, E. Ahmadi, Y. Sun, M. Kira, P. K. Bhattacharya, E. Kioupakis, and Z. Mi, "Controlling Defect Formation of Nanoscale AlN: Toward Efficient Current Conduction of Ultrawide-Bandgap Semiconductors," *Advanced Electronic Materials*, vol. 6, no. 9, p. 2000337, sep 2020. [Online]. Available: https://doi.org/10.1002/aelm.202000337

[35] A. Pandey, X. Liu, Z. Deng, W. J. Shin, D. A. Laleyan, K. Mashooq, E. T. Reid, E. Kioupakis, P. Bhattacharya, and Z. Mi, "Enhanced doping efficiency of ultrawide band gap semiconductors by metal-semiconductor junction assisted epitaxy," *Phys. Rev. Materials*, vol. 3, p. 053401, May 2019. [Online]. Available: https://link.aps.org/doi/10.1103/PhysRevMaterials.3.053401

[36] S. Mertin, B. Heinz, O. Rattunde, G. Christmann, M.-A. Dubois, S. Nicolay, and P. Muralt, "Piezoelectric and structural properties of c-axis textured aluminium scandium nitride thin films up to high scandium content," *Surface and Coatings Technology*, vol. 343, pp. 2–6, 2018, selected papers of the "E-MRS 2017 – Symposium Q". [Online]. Available: https://www.sciencedirect.com/science/article/pii/S0257897218300549

[37] R. Yan, G. Khalsa, S. Vishwanath, Y. Han, J. Wright, S. Rouvimov, D. S. Katzer, N. Nepal, B. P. Downey, D. A. Muller, H. G. Xing, D. J. Meyer, and D. Jena, "GaN/NbN epitaxial semiconductor/superconductor

heterostructures," *Nature*, vol. 555, no. 7695, pp. 183–189, 2018. [Online]. Available: https://doi.org/10.1038/nature25768

[38] T.-N. Ye, S.-W. Park, Y. Lu, J. Li, M. Sasase, M. Kitano, and H. Hosono, "Contribution of Nitrogen Vacancies to Ammonia Synthesis over Metal Nitride Catalysts," *Journal of the American Chemical Society*, vol. 142, no. 33, pp. 14 374–14 383, aug 2020. [Online]. Available: https://doi.org/10.1021/jacs.0c06624

[39] T.-N. Ye, S.-W. Park, Y. Lu, J. Li, M. Sasase, M. Kitano, T. Tada, and H. Hosono, "Vacancy-enabled N2 activation for ammonia synthesis on an Ni-loaded catalyst," *Nature*, vol. 583, no. 7816, pp. 391–395, 2020. [Online]. Available: https://doi.org/10.1038/s41586-020-2464-9

[40] A. Hasegawa, "Electronic structure of La monopnictides," *Journal of Physics C: Solid State Physics*, vol. 13, no. 33, pp. 6147–6156, 1980. [Online]. Available: http://dx.doi.org/10.1088/0022-3719/13/33/012

[41] M. R. Norman, H. J. F. Jansen, D. D. Koelling, and A. J. Freeman, "Electronic structure of LaN: Prediction of a small band overlap semi-metal," *Solid State Communications*, vol. 52, no. 8, pp. 739–741, 1984. [Online]. Available: http://www.sciencedirect.com/science/article/pii/0038109884904010

[42] G. Vaitheeswaran, V. Kanchana, and M. Rajagopalan, "Structural phase stability and superconductivity of LaN," *Solid State Communications*, vol. 124, no. 3, pp. 97–102, 2002. [Online]. Available: http://www.sciencedirect.com/science/article/pii/S0038109802004817

[43] Y. O. Ciftci, K. Çolakoglu, E. Deligoz, and H. Ozisik, "The first-principles study on the LaN," *Materials Chemistry and Physics*, vol. 108, no. 1, pp. 120–123, 2008. [Online]. Available: http://www.sciencedirect.com/science/article/pii/S0254058407005664

[44] E. Zhao and Z. Wu, "Electronic and mechanical properties of 5d transition metal mononitrides via first principles," *Journal of Solid State Chemistry*, vol. 181, no. 10, pp. 2814–2827, 2008. [Online]. Available: http://www.sciencedirect.com/science/article/pii/S0022459608003964

[45] C. Stampfl, W. Mannstadt, R. Asahi, and A. J. Freeman, "Electronic structure and physical properties of early transition metal mononitrides: Density-functional theory LDA, GGA, and screened-exchange LDA FLAPW calculations," *Physical Review B*, vol. 63, no. 15, p. 155106, mar 2001. [Online]. Available: https://link.aps.org/doi/10.1103/PhysRevB.63.155106

[46] S. D. Gupta, S. K. Gupta, and P. K. Jha, "First-principles lattice dynamical study of lanthanum nitride under pseudopotential approximation," *Computational Materials Science*, vol. 49, no. 4, pp. 910–915, 2010. [Online]. Available: https://www.sciencedirect.com/science/article/pii/S0927025610003939

[47] A. T. A. Meenaatci, R. Rajeswarapalanichamy, and K. Iyakutti, “Investigation of structural stability and electronic properties of group III nitrides: a first principles study,” *Phase Transitions*, vol. 86, no. 6, pp. 570–584, jun 2013. [Online]. Available: https://doi.org/10.1080/01411594.2012.713486

[48] P. Larson, W. R. L. Lambrecht, A. Chantis, and M. van Schilfgaarde, “Electronic structure of rare-earth nitrides using the LSDA+U approach: Importance of allowing 4f orbitals to break the cubic crystal symmetry,” *Physical Review B*, vol. 75, no. 4, p. 45114, jan 2007. [Online]. Available: https://link.aps.org/doi/10.1103/PhysRevB.75.045114

[49] M. J. Winiarski and D. Kowalska, “Electronic structure of REN (RE = Sc, Y, La, and Lu) semiconductors by MBJLDA calculations,” *Materials Research Express*, vol. 6, no. 9, p. 95910, 2019. [Online]. Available: http://dx.doi.org/10.1088/2053-1591/ab31c2

[50] M. J. Winiarski and D. A. Kowalska, “Band gap bowings of ternary REN (RE = Sc, Y, La, and Lu) alloys,” *Journal of Alloys and Compounds*, vol. 824, p. 153961, 2020. [Online]. Available: https://www.sciencedirect.com/science/article/pii/S0925838820303248

[51] P. C. Sreeparvathy, V. K. Gudelli, V. Kanchana, G. Vaitheeswaran, A. Svane, and N. E. Christensen, “Thermoelectric properties of binary LnN (Ln=La and Lu): First principles study,” *AIP Conference Proceedings*, vol. 1665, no. 1, p. 110008, jun 2015. [Online]. Available: https://aip.scitation.org/doi/abs/10.1063/1.4918064

[52] F. Hulliger, “Chapter 33 Rare earth pnictides,” in *Handbook on the Physics and Chemistry of Rare Earths*. Elsevier, 1979, vol. 4, pp. 153–236. [Online]. Available: https://www.sciencedirect.com/science/article/pii/S016812737904006X

[53] W. Setyawan and S. Curtarolo, “High-throughput electronic band structure calculations: Challenges and tools,” *Computational Materials Science*, vol. 49, no. 2, pp. 299–312, 2010. [Online]. Available: http://www.sciencedirect.com/science/article/pii/S0927025610002697

[54] R. Resta, “Theory of the electric polarization in crystals,” *Ferroelectrics*, vol. 136, no. 1, pp. 51–55, nov 1992. [Online]. Available: https://doi.org/10.1080/00150199208016065

[55] R. D. King-Smith and D. Vanderbilt, “Theory of polarization of crystalline solids,” *Physical Review B*, vol. 47, no. 3, pp. 1651–1654, jan 1993. [Online]. Available: https://link.aps.org/doi/10.1103/PhysRevB.47.1651

[56] R. W. Nunes and X. Gonze, “Berry-phase treatment of the homogeneous electric field perturbation in insulators,” *Physical Review B*, vol. 63, no. 15,

p. 155107, mar 2001. [Online]. Available: https://link.aps.org/doi/10.1103/PhysRevB.63.155107

[57] I. Souza, J. Íñiguez, and D. Vanderbilt, "First-Principles Approach to Insulators in Finite Electric Fields," *Physical Review Letters*, vol. 89, no. 11, p. 117602, aug 2002. [Online]. Available: https://link.aps.org/doi/10.1103/PhysRevLett.89.117602

[58] R. A. Young and W. T. Ziegler, "Crystal Structure of Lanthanum Nitride," *Journal of the American Chemical Society*, vol. 74, no. 21, pp. 5251–5253, nov 1952. [Online]. Available: https://doi.org/10.1021/ja01141a004

[59] M. Suzuki, T. Uenoyama, and A. Yanase, "First-principles calculations of effective-mass parameters of AlN and GaN," *Physical Review B*, vol. 52, no. 11, pp. 8132–8139, sep 1995. [Online]. Available: https://link.aps.org/doi/10.1103/PhysRevB.52.8132

[60] K. Bushick, S. Chae, Z. Deng, J. T. Heron, and E. Kioupakis, "Boron arsenide heterostructures: lattice-matched heterointerfaces and strain effects on band alignments and mobility," *npj Computational Materials*, vol. 6, no. 1, p. 3, dec 2020. [Online]. Available: http://www.nature.com/articles/s41524-019-0270-4

[61] S. F. Palguev, R. P. Lesunova, and L. S. Karenina, "Ionic conductivity of nitrides," *Solid State Ionics*, vol. 20, no. 4, pp. 255–258, 1986. [Online]. Available: http://www.sciencedirect.com/science/article/pii/0167273886900433

[62] W.-B. Zhang, X.-J. Ma, A. Loh, X. Li, F. C. Walsh, and L.-B. Kong, "High Volumetric Energy Density Capacitors Based on New Electrode Material Lanthanum Nitride," *ACS Energy Letters*, vol. 2, no. 2, pp. 336–341, feb 2017. [Online]. Available: https://doi.org/10.1021/acsenergylett.6b00636

[63] J. Casamento, H. G. Xing, and D. Jena, "Oxygen Incorporation in the Molecular Beam Epitaxy Growth of ScxGa1xN and ScxAl1xN," *physica status solidi (b)*, vol. 257, no. 4, p. 1900612, apr 2020. [Online]. Available: https://doi.org/10.1002/pssb.201900612

[64] P. Wang, B. Wang, D. A. Laleyan, A. Pandey, Y. Wu, Y. Sun, X. Liu, Z. Deng, E. Kioupakis, and Z. Mi, "Oxygen defect dominated photoluminescence emission of ScxAl1xN grown by molecular beam epitaxy," *Applied Physics Letters*, vol. 118, no. 3, p. 32102, jan 2021. [Online]. Available: https://doi.org/10.1063/5.0035026

[65] J. S. Cetnar, A. N. Reed, S. C. Badescu, S. Vangala, H. A. Smith, and D. C. Look, "Electronic transport in degenerate (100) scandium nitride thin films on magnesium oxide substrates," *Applied Physics Letters*, vol. 113, no. 19, p. 192104, nov 2018. [Online]. Available: https://doi.org/10.1063/1.5050200

[66] B. K. Meyer, A. Polity, D. Reppin, M. Becker, P. Hering, P. J. Klar, T. Sander, C. Reindl, J. Benz, M. Eickhoff, C. Heiliger, M. Heinemann, J. Bläsing, A. Krost, S. Shokovets, C. Müller, and C. Ronning, "Binary copper oxide semiconductors: From materials towards devices," *physica status solidi (b)*, vol. 249, no. 8, pp. 1487–1509, aug 2012. [Online]. Available: https://doi.org/10.1002/pssb.201248128

[67] M. Hara, T. Kondo, M. Komoda, S. Ikeda, J. N. Kondo, K. Domen, M. Hara, K. Shinohara, and A. Tanaka, "Cu_2O as a photocatalyst for overall water splitting under visible light irradiation," *Chemical Communications*, no. 3, pp. 357–358, 1998. [Online]. Available: http://dx.doi.org/10.1039/A707440I

[68] K. Tu, Q. Wang, A. Lu, and L. Zhang, "Portable Visible-Light Photocatalysts Constructed from Cu_2O Nanoparticles and Graphene Oxide in Cellulose Matrix," *The Journal of Physical Chemistry C*, vol. 118, no. 13, pp. 7202–7210, apr 2014. [Online]. Available: https://doi.org/10.1021/jp412802h

[69] X. Wan, J. Wang, L. Zhu, and J. Tang, "Gas sensing properties of Cu_2O and its particle size and morphology-dependent gas-detection sensitivity," *Journal of Materials Chemistry A*, vol. 2, no. 33, pp. 13 641–13 647, 2014. [Online]. Available: http://dx.doi.org/10.1039/C4TA02659D

[70] J. Hu, C. Zou, Y. Su, M. Li, Y. Han, E. S.-W. Kong, Z. Yang, and Y. Zhang, "An ultrasensitive NO_2 gas sensor based on a hierarchical Cu_2O/CuO mesocrystal nanoflower," *Journal of Materials Chemistry A*, vol. 6, no. 35, pp. 17 120–17 131, 2018. [Online]. Available: http://dx.doi.org/10.1039/C8TA04404J

[71] K. Matsuzaki, K. Nomura, H. Yanagi, T. Kamiya, M. Hirano, and H. Hosono, "Epitaxial growth of high mobility Cu_2O thin films and application to p-channel thin film transistor," *Applied Physics Letters*, vol. 93, no. 20, p. 202107, nov 2008. [Online]. Available: https://doi.org/10.1063/1.3026539

[72] H. A. Al-Jawhari, "A review of recent advances in transparent p-type Cu_2O-based thin film transistors," *Materials Science in Semiconductor Processing*, vol. 40, pp. 241–252, 2015. [Online]. Available: http://www.sciencedirect.com/science/article/pii/S1369800115300184

[73] M. Singh, D. Jampaiah, A. E. Kandjani, Y. M. Sabri, E. Della Gaspera, P. Reineck, M. Judd, J. Langley, N. Cox, J. van Embden, E. L. H. Mayes, B. C. Gibson, S. K. Bhargava, R. Ramanathan, and V. Bansal, "Oxygen-deficient photostable Cu_2O for enhanced visible light photocatalytic activity," *Nanoscale*, vol. 10, no. 13, pp. 6039–6050, 2018. [Online]. Available: http://dx.doi.org/10.1039/C7NR08388B

[74] F.-Y. Ran, H. Hiramatsu, H. Hosono, T. Kamiya, and M. Taniguti, "Detection of dead layers and defects in polycrystalline Cu_2O thin-film transistors by x-ray reflectivity and photoresponse spectroscopy analyses," *Journal of Vacuum*

Science Technology B, vol. 33, no. 5, p. 51211, aug 2015. [Online]. Available: https://doi.org/10.1116/1.4929445

[75] L. Papadimitriou, C. A. Dimitriadis, and L. Dozsa, "Trap centers in cuprous oxide," *Solid-State Electronics*, vol. 31, no. 10, pp. 1477–1482, 1988. [Online]. Available: http://www.sciencedirect.com/science/article/pii/0038110188900184

[76] G. K. Paul, Y. Nawa, H. Sato, T. Sakurai, and K. Akimoto, "Defects in Cu_2O studied by deep level transient spectroscopy," *Applied Physics Letters*, vol. 88, no. 14, p. 141901, apr 2006. [Online]. Available: https://doi.org/10.1063/1.2175492

[77] N. L. Peterson and C. L. Wiley, "Diffusion and point defects in Cu_2O," *Journal of Physics and Chemistry of Solids*, vol. 45, no. 3, pp. 281–294, 1984. [Online]. Available: http://www.sciencedirect.com/science/article/pii/0022369784900337

[78] J. H. Park and K. Natesan, "Oxidation of copper and electronic transport in copper oxides," *Oxidation of Metals*, vol. 39, pp. 411–435, 1993.

[79] O. Porat and I. Riess, "Defect chemistry of $Cu_{2-y}O$ at elevated temperatures. Part II: Electrical conductivity, thermoelectric power and charged point defects," *Solid State Ionics*, vol. 81, no. 1, pp. 29–41, 1995. [Online]. Available: http://www.sciencedirect.com/science/article/pii/0167273895001697

[80] J. P. Perdew and A. Zunger, "Self-interaction correction to density-functional approximations for many-electron systems," *Physical Review B*, vol. 23, no. 10, pp. 5048–5079, may 1981. [Online]. Available: https://link.aps.org/doi/10.1103/PhysRevB.23.5048

[81] A. F. Wright and J. S. Nelson, "Theory of the copper vacancy in cuprous oxide," *Journal of Applied Physics*, vol. 92, no. 10, pp. 5849–5851, oct 2002. [Online]. Available: https://doi.org/10.1063/1.1516620

[82] M. Nolan and S. D. Elliott, "The p-type conduction mechanism in Cu_2O: a first principles study," *Physical Chemistry Chemical Physics*, vol. 8, no. 45, pp. 5350–5358, 2006. [Online]. Available: http://dx.doi.org/10.1039/B611969G

[83] D. O. Scanlon, B. J. Morgan, and G. W. Watson, "Modeling the polaronic nature of p-type defects in Cu_2O: The failure of GGA and GGA+U," *The Journal of Chemical Physics*, vol. 131, no. 12, p. 124703, sep 2009. [Online]. Available: https://doi.org/10.1063/1.3231869

[84] D. O. Scanlon, B. J. Morgan, G. W. Watson, and A. Walsh, "Acceptor Levels in p-Type Cu_2O: Rationalizing Theory and Experiment," *Physical Review Letters*, vol. 103, no. 9, p. 96405, aug 2009. [Online]. Available: https://link.aps.org/doi/10.1103/PhysRevLett.103.096405

[85] D. O. Scanlon and G. W. Watson, “Uncovering the Complex Behavior of Hydrogen in Cu_2O,” *Physical Review Letters*, vol. 106, no. 18, p. 186403, may 2011. [Online]. Available: https://link.aps.org/doi/10.1103/PhysRevLett.106.186403

[86] L. Y. Isseroff and E. A. Carter, “Electronic Structure of Pure and Doped Cuprous Oxide with Copper Vacancies: Suppression of Trap States,” *Chemistry of Materials*, vol. 25, no. 3, pp. 253–265, feb 2013. [Online]. Available: https://doi.org/10.1021/cm3040278

[87] M. Chase, “NIST-JANAF Thermochemical Tables, 4th Edition,” p. 1023, 1998.

[88] M. O’Keeffe, “Infrared Optical Properties of Cuprous Oxide,” *The Journal of Chemical Physics*, vol. 39, no. 7, pp. 1789–1793, oct 1963. [Online]. Available: https://doi.org/10.1063/1.1734530

[89] J. Jo, J. D. Lenef, K. Mashooq, O. Trejo, N. P. Dasgupta, and R. L. Peterson, “Causes of the Difference Between Hall Mobility and Field-Effect Mobility for p-Type RF Sputtered Cu_2O Thin-Film Transistors,” *IEEE Transactions on Electron Devices*, vol. 67, no. 12, pp. 5557–5563, 2020.

[90] J. D. Lenef, J. Jo, O. Trejo, D. J. Mandia, R. L. Peterson, and N. P. Dasgupta, “Plasma-Enhanced Atomic Layer Deposition of p-Type Copper Oxide Semiconductors with Tunable Phase, Oxidation State, and Morphology,” *Journal of Physical Chemistry C*, vol. 125, no. 17, pp. 9383–9390, 2021.

[91] J. P. Dahl and A. C. Switendick, “Energy bands in cuprous oxide,” *Journal of Physics and Chemistry of Solids*, vol. 27, no. 6, pp. 931–942, 1966. [Online]. Available: http://www.sciencedirect.com/science/article/pii/0022369766900643

[92] P. Marksteiner, P. Blaha, and K. Schwarz, “Electronic structure and binding mechanism of Cu_2O,” *Zeitschrift für Physik B Condensed Matter*, vol. 64, no. 2, pp. 119–127, 1986. [Online]. Available: https://doi.org/10.1007/BF01303692

[93] E. Ruiz, S. Alvarez, P. Alemany, and R. A. Evarestov, “Electronic structure and properties of Cu_2O,” *Physical Review B*, vol. 56, no. 12, pp. 7189–7196, sep 1997. [Online]. Available: https://link.aps.org/doi/10.1103/PhysRevB.56.7189

[94] F. Bruneval, N. Vast, L. Reining, M. Izquierdo, F. Sirotti, and N. Barrett, “Exchange and Correlation Effects in Electronic Excitations of Cu_2O,” *Physical Review Letters*, vol. 97, no. 26, p. 267601, dec 2006. [Online]. Available: https://link.aps.org/doi/10.1103/PhysRevLett.97.267601

[95] T. Kotani, M. van Schilfgaarde, and S. V. Faleev, “Quasiparticle self-consistent GW method: A basis for the independent-particle approximation,” *Physical Review B*, vol. 76, no. 16, p. 165106, oct 2007. [Online]. Available: https://link.aps.org/doi/10.1103/PhysRevB.76.165106

[96] M. Heinemann, B. Eifert, and C. Heiliger, “Band structure and phase stability of the copper oxides Cu_2O, CuO, and Cu_4O_3,” *Physical Review B*, vol. 87, no. 11, p. 115111, mar 2013. [Online]. Available: https://link.aps.org/doi/10.1103/PhysRevB.87.115111

[97] F. Tran and P. Blaha, “Implementation of screened hybrid functionals based on the Yukawa potential within the LAPW basis set,” *Physical Review B*, vol. 83, no. 23, p. 235118, jun 2011. [Online]. Available: https://link.aps.org/doi/10.1103/PhysRevB.83.235118

[98] T. Ito, T. Kawashima, H. Yamaguchi, T. Masumi, and S. Adachi, “Optical Properties of Cu_2O Studied by Spectroscopic Ellipsometry,” *Journal of the Physical Society of Japan*, vol. 67, no. 6, pp. 2125–2131, jun 1998. [Online]. Available: https://doi.org/10.1143/JPSJ.67.2125

[99] F. Haidu, M. Fronk, O. D. Gordan, C. Scarlat, G. Salvan, and D. R. T. Zahn, “Dielectric function and magneto-optical Voigt constant of Cu_2O: A combined spectroscopic ellipsometry and polar magneto-optical Kerr spectroscopy study,” *Physical Review B*, vol. 84, no. 19, p. 195203, nov 2011. [Online]. Available: https://link.aps.org/doi/10.1103/PhysRevB.84.195203

[100] C. Malerba, F. Biccari, C. Leonor Azanza Ricardo, M. D’Incau, P. Scardi, and A. Mittiga, “Absorption coefficient of bulk and thin film Cu_2O,” *Solar Energy Materials and Solar Cells*, vol. 95, no. 10, pp. 2848–2854, 2011. [Online]. Available: http://www.sciencedirect.com/science/article/pii/S0927024811003229

[101] J.-W. Park, H. Jang, S. Kim, S.-H. Choi, H. Lee, J. Kang, and S.-H. Wei, “Microstructure, optical property, and electronic band structure of cuprous oxide thin films,” *Journal of Applied Physics*, vol. 110, no. 10, p. 103503, nov 2011. [Online]. Available: https://doi.org/10.1063/1.3660782

[102] L. Zhang, L. McMillon, and J. McNatt, “Gas-dependent bandgap and electrical conductivity of Cu_2O thin films,” *Solar Energy Materials and Solar Cells*, vol. 108, pp. 230–234, 2013. [Online]. Available: http://www.sciencedirect.com/science/article/pii/S0927024812002358

[103] R. D. Schmidt-Whitley, M. Martinez-Clemente, and A. Revcolevschi, “Growth and microstructural control of single crystal cuprous oxide Cu_2O,” *Journal of Crystal Growth*, vol. 23, no. 2, pp. 113–120, 1974. [Online]. Available: http://www.sciencedirect.com/science/article/pii/0022024874901109

[104] J. P. Allen, D. O. Scanlon, L. F. J. Piper, and G. W. Watson, “Understanding the defect chemistry of tin monoxide,” *Journal of Materials Chemistry C*, vol. 1, no. 48, pp. 8194–8208, 2013. [Online]. Available: http://dx.doi.org/10.1039/C3TC31863J

[105] J. Buckeridge, "Equilibrium point defect and charge carrier concentrations in a material determined through calculation of the self-consistent Fermi energy," *Computer Physics Communications*, vol. 244, pp. 329–342, 2019. [Online]. Available: http://www.sciencedirect.com/science/article/pii/S0010465519302048

[106] N. Tabuchi and H. Matsumura, "Control of Carrier Concentration in Thin Cuprous Oxide Cu_2O Films by Atomic Hydrogen," *Japanese Journal of Applied Physics*, vol. 41, no. Part 1, No. 8, pp. 5060–5063, 2002. [Online]. Available: http://dx.doi.org/10.1143/JJAP.41.5060

[107] D. S. Murali, S. Kumar, R. J. Choudhary, A. D. Wadikar, M. K. Jain, and A. Subrahmanyam, "Synthesis of Cu_2O from CuO thin films: Optical and electrical properties," *AIP Advances*, vol. 5, no. 4, p. 47143, apr 2015. [Online]. Available: https://doi.org/10.1063/1.4919323

[108] C. G. Van de Walle, "Hydrogen as a Cause of Doping in Zinc Oxide," *Physical Review Letters*, vol. 85, no. 5, pp. 1012–1015, jul 2000. [Online]. Available: https://link.aps.org/doi/10.1103/PhysRevLett.85.1012

[109] S. F. J. Cox, E. A. Davis, S. P. Cottrell, P. J. C. King, J. S. Lord, J. M. Gil, H. V. Alberto, R. C. Vilão, J. Piroto Duarte, N. Ayres de Campos, A. Weidinger, R. L. Lichti, and S. J. C. Irvine, "Experimental Confirmation of the Predicted Shallow Donor Hydrogen State in Zinc Oxide," *Physical Review Letters*, vol. 86, no. 12, pp. 2601–2604, mar 2001. [Online]. Available: https://link.aps.org/doi/10.1103/PhysRevLett.86.2601

[110] K. P. Hering, C. Kandzia, J. Benz, B. G. Kramm, M. Eickhoff, and P. J. Klar, "Hydrogen induced mobility enhancement in RF sputtered Cu_2O thin films," *Journal of Applied Physics*, vol. 120, no. 18, p. 185705, nov 2016. [Online]. Available: https://doi.org/10.1063/1.4966605

[111] J. T-Thienprasert and S. Limpijumnong, "Identification of nitrogen acceptor in Cu_2O: First-principles study," *Applied Physics Letters*, vol. 107, no. 22, p. 221905, nov 2015. [Online]. Available: https://doi.org/10.1063/1.4936760

[112] S. Ishizuka, S. Kato, T. Maruyama, and K. Akimoto, "Nitrogen Doping into Cu_2O Thin Films Deposited by Reactive Radio-Frequency Magnetron Sputtering," *Japanese Journal of Applied Physics*, vol. 40, no. Part 1, No. 4B, pp. 2765–2768, 2001. [Online]. Available: http://dx.doi.org/10.1143/JJAP.40.2765

[113] Y. S. Lee, J. Heo, M. T. Winkler, S. C. Siah, S. B. Kim, R. G. Gordon, and T. Buonassisi, "Nitrogen-doped cuprous oxide as a p-type hole-transporting layer in thin-film solar cells," *Journal of Materials Chemistry A*, vol. 1, no. 48, pp. 15 416–15 422, 2013. [Online]. Available: http://dx.doi.org/10.1039/C3TA13208K

[114] J. Benz, K. P. Hering, B. Kramm, A. Polity, P. J. Klar, S. C. Siah, and T. Buonassisi, "The influence of nitrogen doping on the electrical and vibrational properties of Cu_2O," *physica status solidi (b)*, vol. 254, no. 4, p. 1600421, apr 2017. [Online]. Available: https://doi.org/10.1002/pssb.201600421

[115] G. B. Abdullaev, Z. A. Aliyarova, E. H. Zamanova, and G. A. Asadov, "Investigation of the electric properties of Cu_2S single crystals," *physica status solidi (b)*, vol. 26, no. 1, pp. 65–68, jan 1968. [Online]. Available: https://doi.org/10.1002/pssb.19680260103

[116] R. Wagner and H.-D. Wiemhöfer, "Hall effect and conductivity in thin films of low temperature chalcocite Cu_2S at 20°C as a function of stoichiometry," *Journal of Physics and Chemistry of Solids*, vol. 44, no. 8, pp. 801–805, 1983. [Online]. Available: https://www.sciencedirect.com/science/article/pii/0022369783900136

[117] M. Nolan and S. D. Elliott, "Tuning the Transparency of Cu_2O with Substitutional Cation Doping," *Chemistry of Materials*, vol. 20, no. 17, pp. 5522–5531, sep 2008. [Online]. Available: https://doi.org/10.1021/cm703395k

[118] J. Resende, C. Jiménez, N. D. Nguyen, and J.-L. Deschanvres, "Magnesium-doped cuprous oxide ($Mg:Cu_2O$) thin films as a transparent p-type semiconductor," *physica status solidi (a)*, vol. 213, no. 9, pp. 2296–2302, sep 2016. [Online]. Available: https://doi.org/10.1002/pssa.201532870

[119] S. Nakamura and M. R. Krames, "History of gallium–nitride-based light-emitting diodes for illumination," *Proceedings of the IEEE*, vol. 101, no. 10, pp. 2211–2220, 2013.

[120] M. Parker, "A gallium nitride HEMT that enhances," *Nature Electronics*, vol. 4, no. 12, p. 858, 2021. [Online]. Available: https://doi.org/10.1038/s41928-021-00698-3

[121] N. Feldberg, J. D. Aldous, W. M. Linhart, L. J. Phillips, K. Durose, P. A. Stampe, R. J. Kennedy, D. O. Scanlon, G. Vardar, R. L. Field, T. Y. Jen, R. S. Goldman, T. D. Veal, and S. M. Durbin, "Growth, disorder, and physical properties of $ZnSnN_2$," *Applied Physics Letters*, vol. 103, no. 4, p. 42109, jul 2013. [Online]. Available: https://doi.org/10.1063/1.4816438

[122] P. C. Quayle, E. W. Blanton, A. Punya, G. T. Junno, K. He, L. Han, H. Zhao, J. Shan, W. R. L. Lambrecht, and K. Kash, "Charge-neutral disorder and polytypes in heterovalent wurtzite-based ternary semiconductors: The importance of the octet rule," *Phys. Rev. B*, vol. 91, p. 205207, May 2015. [Online]. Available: https://link.aps.org/doi/10.1103/PhysRevB.91.205207

[123] S. Lany, A. N. Fioretti, P. P. Zawadzki, L. T. Schelhas, E. S. Toberer, A. Zakutayev, and A. C. Tamboli, "Monte carlo simulations of disorder in $znsnn_2$ and the effects on the electronic structure,"

Phys. Rev. Materials, vol. 1, p. 035401, Aug 2017. [Online]. Available: https://link.aps.org/doi/10.1103/PhysRevMaterials.1.035401

[124] S. Chen, P. Narang, H. A. Atwater, and L. W. Wang, "Phase stability and defect physics of a ternary $ZnSnN_2$ semiconductor: First principles insights," *Advanced Materials*, vol. 26, no. 2, pp. 311–315, 2014.

[125] R. A. Makin, K. York, S. M. Durbin, N. Senabulya, J. Mathis, R. Clarke, N. Feldberg, P. Miska, C. M. Jones, Z. Deng, L. Williams, E. Kioupakis, and R. J. Reeves, "Alloy-Free Band Gap Tuning across the Visible Spectrum," *Physical Review Letters*, vol. 122, no. 25, p. 256403, 2019. [Online]. Available: https://link.aps.org/doi/10.1103/PhysRevLett.122.256403

[126] R. D. Shannon, "Revised effective ionic radii and systematic studies of interatomic distances in halides and chalcogenides," *Acta Crystallographica Section A*, vol. 32, no. 5, pp. 751–767, sep 1976. [Online]. Available: https://doi.org/10.1107/S0567739476001551

[127] E. P. George, D. Raabe, and R. O. Ritchie, "High-entropy alloys," *Nature Reviews Materials*, vol. 4, no. 8, pp. 515–534, 2019. [Online]. Available: https://doi.org/10.1038/s41578-019-0121-4

[128] J.-W. Yeh, S.-K. Chen, S.-J. Lin, J.-Y. Gan, T.-S. Chin, T.-T. Shun, C.-H. Tsau, and S.-Y. Chang, "Nanostructured high-entropy alloys with multiple principal elements: Novel alloy design concepts and outcomes," *Advanced Engineering Materials*, vol. 6, no. 5, pp. 299–303, 2004. [Online]. Available: http://www.aem-journal.de

[129] B. Cantor, I. T. Chang, P. Knight, and A. J. Vincent, "Microstructural development in equiatomic multicomponent alloys," *Materials Science and Engineering A*, vol. 375-377, no. 1-2 SPEC. ISS., pp. 213–218, 2004.

[130] B. Gludovatz, A. Hohenwarter, D. Catoor, E. H. Chang, E. P. George, and R. O. Ritchie, "A fracture-resistant high-entropy alloy for cryogenic applications." *Science*, vol. 345, no. 6201, pp. 1153–1158, 2014.

[131] Y. Lu, Y. Dong, S. Guo, L. Jiang, H. Kang, T. Wang, B. Wen, Z. Wang, J. Jie, Z. Cao, H. Ruan, and T. Li, "A promising new class of high-temperature alloys: eutectic high-entropy alloys," *Scientific Reports*, vol. 4, no. 1, p. 6200, 2014. [Online]. Available: https://doi.org/10.1038/srep06200

[132] C. P. Lee, Y. Y. Chen, C. Y. Hsu, J. W. Yeh, and H. C. Shih, "The effect of boron on the corrosion resistance of the high entropy alloys Al0.5CoCrCuFeNiBx," *Journal of The Electrochemical Society*, vol. 154, no. 8, pp. C424–C430, 2007.

[133] C. M. Rost, E. Sachet, T. Borman, A. Moballegh, E. C. Dickey, D. Hou, J. L. Jones, S. Curtarolo, and J. P. Maria, "Entropy-stabilized

oxides," *Nature Communications*, vol. 6, p. 8485, 2015. [Online]. Available: http://dx.doi.org/10.1038/ncomms9485

[134] J. Zhou, J. Zhang, F. Zhang, B. Niu, L. Lei, and W. Wang, "High-entropy carbide: A novel class of multicomponent ceramics," *Ceramics International*, vol. 44, no. 17, pp. 22 014–22 018, 2018.

[135] Y. Qin, J. X. Liu, F. Li, X. Wei, H. Wu, and G. J. Zhang, "A high entropy silicide by reactive spark plasma sintering," *Journal of Advanced Ceramics*, vol. 8, no. 1, pp. 148–152, 2019. [Online]. Available: www.springer.com/journal/40145

[136] J. Gild, Y. Zhang, T. Harrington, S. Jiang, T. Hu, M. C. Quinn, W. M. Mellor, N. Zhou, K. Vecchio, and J. Luo, "High-entropy metal diborides: A new class of high-entropy materials and a new type of ultrahigh temperature ceramics," *Scientific Reports*, vol. 6, p. 37946, 2016. [Online]. Available: www.nature.com/scientificreports/

[137] T. Jin, X. Sang, R. R. Unocic, R. T. Kinch, X. Liu, J. Hu, H. Liu, and S. Dai, "Mechanochemical-assisted synthesis of high-entropy metal nitride via a soft urea strategy," *Advanced Materials*, vol. 30, no. 23, p. 1707512, 2018.

[138] P. Koželj, S. Vrtnik, A. Jelen, S. Jazbec, Z. Jagličić, S. Maiti, M. Feuerbacher, W. Steurer, and J. Dolinšek, "Discovery of a superconducting high-entropy alloy," *Physical Review Letters*, vol. 113, no. 10, p. 107001, 2014.

[139] D. Bérardan, S. Franger, D. Dragoe, A. K. Meena, and N. Dragoe, "Colossal dielectric constant in high entropy oxides," *physica status solidi (RRL) – Rapid Research Letters*, vol. 10, no. 4, pp. 328–333, apr 2016. [Online]. Available: https://doi.org/10.1002/pssr.201600043

[140] A. Sarkar, L. Velasco, D. Wang, Q. Wang, G. Talasila, L. de Biasi, C. Kübel, T. Brezesinski, S. S. Bhattacharya, H. Hahn, and B. Breitung, "High entropy oxides for reversible energy storage," *Nature Communications*, vol. 9, no. 1, p. 3400, 2018. [Online]. Available: https://doi.org/10.1038/s41467-018-05774-5

[141] S. B. Desai, S. R. Madhvapathy, A. B. Sachid, J. P. Llinas, Q. Wang, H. Ahn, G. Pitner, M. J. Kim, J. Bokor, C. Hu, H.-S. P. Wong, and A. Javey, "MoS¡sub¿2¡/sub¿ transistors with 1-nanometer gate lengths," *Science*, vol. 354, no. 6308, pp. 99–102, 2016.

[142] W. Wang, M. T. Winkler, O. Gunawan, T. Gokmen, T. K. Todorov, Y. Zhu, and D. B. Mitzi, "Device characteristics of CZTSSe thin-film solar cells with 12.6efficiency," *Advanced Energy Materials*, vol. 4, no. 7, p. 1301465, 2014.

[143] A. I. Hochbaum and P. Yang, "Semiconductor nanowires for energy conversion," *Chemical Reviews*, vol. 110, no. 1, pp. 527–546, jan 2010. [Online]. Available: https://doi.org/10.1021/cr900075v

[144] L. Williams and E. Kioupakis, "BInGaN alloys nearly lattice-matched to GaN for high-power high-efficiency visible LEDs," *Applied Physics Letters*, vol. 111, no. 21, p. 211107, nov 2017. [Online]. Available: https://doi.org/10.1063/1.4997601

[145] C.-Z. Ning, L. Dou, and P. Yang, "Bandgap engineering in semiconductor alloy nanomaterials with widely tunable compositions," *Nature Reviews Materials*, vol. 2, no. 12, p. 17070, 2017. [Online]. Available: https://doi.org/10.1038/natrevmats.2017.70

[146] J. D. Sau and M. L. Cohen, "Possibility of increased mobility in Ge-Sn alloy system," *Physical Review B*, vol. 75, no. 4, p. 045208, jan 2007. [Online]. Available: https://link.aps.org/doi/10.1103/PhysRevB.75.045208

[147] B. Qin, X. Hu, Y. Zhang, H. Wu, S. J. Pennycook, and L.-D. Zhao, "Comprehensive investigation on the thermoelectric properties of p-type PbTe-PbSe-PbS alloys," *Advanced Electronic Materials*, vol. 5, no. 12, p. 1900609, dec 2019. [Online]. Available: https://doi.org/10.1002/aelm.201900609

[148] X. Yan, B. Poudel, Y. Ma, W. S. Liu, G. Joshi, H. Wang, Y. Lan, D. Wang, G. Chen, and Z. F. Ren, "Experimental studies on anisotropic thermoelectric properties and structures of n-type Bi2Te2.7Se0.3," *Nano Letters*, vol. 10, no. 9, pp. 3373–3378, sep 2010. [Online]. Available: https://doi.org/10.1021/nl101156v

[149] M. Hong, T. C. Chasapis, Z.-G. Chen, L. Yang, M. G. Kanatzidis, G. J. Snyder, and J. Zou, "n-type Bi2Te3–xSex nanoplates with enhanced thermoelectric efficiency driven by wide-frequency phonon scatterings and synergistic carrier scatterings," *ACS Nano*, vol. 10, no. 4, pp. 4719–4727, apr 2016. [Online]. Available: https://doi.org/10.1021/acsnano.6b01156

[150] W. He, D. Wang, H. Wu, Y. Xiao, Y. Zhang, D. He, Y. Feng, Y.-J. Hao, J.-F. Dong, R. Chetty, L. Hao, D. Chen, J. Qin, Q. Yang, X. Li, J.-M. Song, Y. Zhu, W. Xu, C. Niu, X. Li, G. Wang, C. Liu, M. Ohta, S. J. Pennycook, J. He, J.-F. Li, and L.-D. Zhao, "High thermoelectric performance in low-cost SnS0.91Se0.09 crystals," *Science*, vol. 365, no. 6460, pp. 1418 LP – 1424, sep 2019. [Online]. Available: http://science.sciencemag.org/content/365/6460/1418.abstract

[151] M. Samanta and K. Biswas, "Low thermal conductivity and high thermoelectric performance in (GeTe)1–2x(GeSe)x(GeS)x: Competition between solid solution and phase separation," *Journal of the American Chemical Society*, vol. 139, no. 27, pp. 9382–9391, jul 2017. [Online]. Available: https://doi.org/10.1021/jacs.7b05143

[152] J. Dong, F.-H. Sun, H. Tang, J. Pei, H.-L. Zhuang, H.-H. Hu, B.-P. Zhang, Y. Pan, and J.-F. Li, "Medium-temperature thermoelectric GeTe: vacancy

suppression and band structure engineering leading to high performance," *Energy Environmental Science*, vol. 12, no. 4, pp. 1396–1403, 2019. [Online]. Available: http://dx.doi.org/10.1039/C9EE00317G

[153] R. Liu, H. Chen, K. Zhao, Y. Qin, B. Jiang, T. Zhang, G. Sha, X. Shi, C. Uher, W. Zhang, and L. Chen, "Entropy as a gene-like performance indicator promoting thermoelectric materials," *Advanced Materials*, vol. 29, no. 38, p. 1702712, 2017.

[154] Y. Qiu, Y. Jin, D. Wang, M. Guan, W. He, S. Peng, R. Liu, X. Gao, and L.-D. Zhao, "Realizing high thermoelectric performance in GeTe through decreasing the phase transition temperature via entropy engineering," *Journal of Materials Chemistry A*, vol. 7, no. 46, pp. 26 393–26 401, 2019. [Online]. Available: http://dx.doi.org/10.1039/C9TA10963C

[155] Z. Fan, H. Wang, Y. Wu, X. Liu, and Z. Lu, "Thermoelectric performance of PbSnTeSe high-entropy alloys," *Materials Research Letters*, vol. 5, no. 3, pp. 187–194, may 2017. [Online]. Available: https://doi.org/10.1080/21663831.2016.1244116

[156] L. Hu, Y. Zhang, H. Wu, J. Li, Y. Li, M. Mckenna, J. He, F. Liu, S. J. Pennycook, and X. Zeng, "Entropy engineering of SnTe: Multi-principal-element alloying leading to ultralow lattice thermal conductivity and state-of-the-art thermoelectric performance," *Advanced Energy Materials*, vol. 8, no. 29, p. 1802116, oct 2018. [Online]. Available: https://doi.org/10.1002/aenm.201802116

[157] D. B. Miracle and O. N. Senkov, "A critical review of high entropy alloys and related concepts," *Acta Materialia*, vol. 122, pp. 448–511, 2017. [Online]. Available: http://www.sciencedirect.com/science/article/pii/S1359645416306759

[158] R.-Z. Zhang, F. Gucci, H. Zhu, K. Chen, and M. J. Reece, "Data-driven design of ecofriendly thermoelectric high-entropy sulfides," *Inorganic Chemistry*, vol. 57, no. 20, pp. 13 027–13 033, 2018. [Online]. Available: https://pubs.acs.org/sharingguidelines

[159] N. Dragoe and D. Bérardan, "Order emerging from disorder," *Science*, vol. 366, no. 6465, pp. 573 LP – 574, nov 2019. [Online]. Available: http://science.sciencemag.org/content/366/6465/573.abstract

[160] Q. Wang, A. Sarkar, D. Wang, L. Velasco, R. Azmi, S. S. Bhattacharya, T. Bergfeldt, A. Düvel, P. Heitjans, T. Brezesinski, H. Hahn, and B. Breitung, "Multi-anionic and -cationic compounds: new high entropy materials for advanced Li-ion batteries," *Energy Environmental Science*, vol. 12, no. 8, pp. 2433–2442, 2019. [Online]. Available: http://dx.doi.org/10.1039/C9EE00368A

[161] L. D. Zhao, S. H. Lo, Y. Zhang, H. Sun, G. Tan, C. Uher, C. Wolverton, V. P. Dravid, and M. G. Kanatzidis, "Ultralow thermal conductivity and high thermoelectric figure of merit in SnSe crystals," *Nature*, vol. 508, no. 7496, pp. 373–377, 2014.

[162] C. M. Rost, Z. Rak, D. W. Brenner, and J.-P. Maria, "Local structure of the MgxNixCoxCuxZnxO(x=0.2) entropy-stabilized oxide: An EXAFS study," *Journal of the American Ceramic Society*, vol. 100, no. 6, pp. 2732–2738, jun 2017. [Online]. Available: https://doi.org/10.1111/jace.14756

[163] J. Vidal, S. Lany, M. D'Avezac, A. Zunger, A. Zakutayev, J. Francis, and J. Tate, "Band-structure, optical properties, and defect physics of the photovoltaic semiconductor SnS," *Applied Physics Letters*, vol. 100, no. 3, p. 032104, 2012.

[164] W.-H. Xie, B.-G. Liu, and D. G. Pettifor, "Half-metallic ferromagnetism in transition metal pnictides and chalcogenides with wurtzite structure," *Physical Review B*, vol. 68, no. 13, p. 134407, oct 2003. [Online]. Available: https://link.aps.org/doi/10.1103/PhysRevB.68.134407

[165] Y. Sun, Z. Zhong, T. Shirakawa, C. Franchini, D. Li, Y. Li, S. Yunoki, and X.-Q. Chen, "Rocksalt SnS and SnSe: Native topological crystalline insulators," *Phys. Rev. B*, vol. 88, no. 23, p. 235122, dec 2013. [Online]. Available: https://link.aps.org/doi/10.1103/PhysRevB.88.235122

[166] F.-C. Hsu, J.-Y. Luo, K.-W. Yeh, T.-K. Chen, T.-W. Huang, P. M. Wu, Y.-C. Lee, Y.-L. Huang, Y.-Y. Chu, D.-C. Yan, and M.-K. Wu, "Superconductivity in the PbO-type structure α-FeSe," *Proceedings of the National Academy of Sciences*, vol. 105, no. 38, pp. 14 262–14 264, 2008. [Online]. Available: https://www.pnas.org/content/105/38/14262